



THE UNIVERSITY *of* EDINBURGH  
School of Physics  
and Astronomy

GROUP PROJECT

# How Can We Detect Gravitational Waves and What Can They Teach Us About the Universe?

*Nye Baker*  
*Magnus Haughey*  
*Chloe McGeorge*  
*Jonas Paulavičius*  
*Jason Pericleous*  
*Francesco Sarandrea*

supervised by  
Dr. Ross GALLOWAY

February 16, 2017

## **Abstract**

The aim of this review is to introduce the reader to gravitational waves, justify their existence and explain how we can use them to see, or rather hear, more of the Universe. The review will start with a brief introduction into the 4 types of gravitational wave (continuous, inspiral, burst and stochastic). Then, by examining Einstein's field equations, a mathematical justification of the existence of gravitational waves will be presented from the viewpoint of general relativity. The review will progress to examine the astrophysical sources of gravitational waves with a detailed study of binary systems (neutron star and black hole) as they are the most prolific sources. Supernovae and the stochastic background are also examined as sources. The detector technology used to detect gravitational waves will be covered from the first ideas to Weber bars to interferometric detectors to space based gravitational waves detection and beyond with a focus on sources of noise and how to combat them. Then the methodology of matched filtering will be explained in detail as a method of data analysis that can be applied to all gravitational wave detectors. Other data analysis techniques will be outlined and the report will conclude with a study of the GW150914 data signal observed at the LIGO detector in September 2015. With the content covered in this report, it is easy to justify the research and funding invested into gravitational waves thus far and perceive why research will continue well into the future.

# 1 Introduction

On September 14, 2015 at 5:51 a.m. Eastern European Time, the twin Laser Interferometer Gravitational Wave Observatory (LIGO) located in Livingston, Louisiana, and Hanford, Washington, in the US, recorded the first detection of gravitational waves (GW)<sup>7</sup>. The discovery represented a major breakthrough in many fields of Physics, from observational astronomy to general relativity. Later on in the same year, on December 26, a second GW signal was detected by LIGO<sup>10</sup>. In Figure 1 we see the plot of the first of the detected signal.

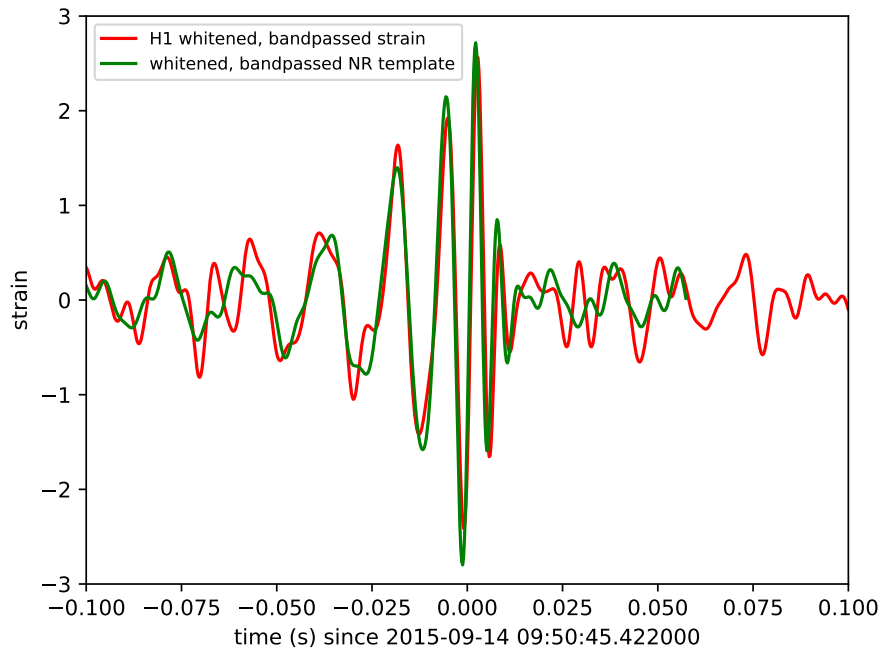


Figure 1: Shown in this plot is the whitened and bandpassed signal from the H1 detector around 2015-09-14 09:50:45 UTC, the signal is better known as GW150914<sup>7</sup>. It is overlaid by the best-fit numerical relativity waveform template corresponding to two black holes of around 30 solar masses each merging (see §6.5 for more detail).

The signal was produced during the final stages of the life of a black hole binary system. The binary system consists of two black holes orbiting each other, losing energy via the emission of GW in Space. In these systems, as energy is lost, the orbits of the two bodies start collapsing and the objects begin to approach each other at an increasing rate until they finally merge into one more massive black hole. The GW emitted during the final orbits and the merging phase were the ones detected by LIGO.

The two first detections (GW150914 followed by GW151226) represent the end result of more than fifty years of research which pushed the boundaries of modern physics both on theoretical ground (as more and more progress was made in the understanding of the consequences of General Relativity) and in the formulation of Cosmological models, experimental techniques and data analysis which made possible to construct detectors whose complexity and sensitivity was unconceivable only a decade ago.

## 1.1 Historical Background

The very first introduction of the idea of GW was made by Henri Poincaré in 1905<sup>81</sup> where he theorised them as the carriers of the gravitational interaction. When Albert Einstein published his General Theory of Relativity ten years later, in 1915, he found out that the equations describing the deformation of space-time admitted wave-like solutions, so the existence of GW was possible. In the years following GW were at the centre of a heated debate, with Einstein himself changing his mind various times on the possibility of their existence<sup>36</sup>. In 1957 Richard Feynman showed that it was theoretically possible for GW to do work against frictional forces<sup>36</sup>, making the prospect of their detection more plausible than it had been before.

The first indirect detection of GW came only in 1975 when researchers Hulse and Taylor demonstrated how the loss of energy of the rotating pulsar PSR1913 + 16 was consistent with the predicted amount of energy emitted by the object via GW<sup>59</sup>. After this experimental result, interest on the possibility of a direct detection has increased, leading to the development of highly sensitive detectors which made the 2015 LIGO discovery possible.

## 1.2 Main Aims of the Report and Motivation

This paper has the main aim of addressing two fundamental questions regarding gravitational waves: how can such signals be detected and what new information about the Universe can be extracted from them? The first question explores the development of the detecting technology, discussing the physical principles exploited by apparatuses such as LIGO and the technical ingenuity that makes the construction of these detectors possible. This is not limited to the physical construction of the detectors, but also includes an exploration of the data analysis techniques used to study the detected signal. The second question shifts the focus from the *detection* of GWs to their possible *employment* as a tool to probe the Universe and gather information about astrophysical events which would otherwise be inaccessible, such as supernovae explosions or black holes merging. In order to answer the questions, this report presents a summary of the state of the art of GW research and its future perspectives both in a theoretical and an experimental context.

There are many reasons that motivate the interest towards both the questions presented above. Firstly, GWs represent a new physical phenomena which has never been observed before, so studying them is intrinsically interesting and will allow us to expand our knowledge of the Universe in which we live. From the theoretical perspective, if the existence of GW is another confirmation of the correctness of general relativity, it offers the chance to test the theory in new ways by opening a window for highly relativistic phenomena which have never been observed before. If the physics of these events turned out to be different from Einstein's predictions we would discover a flaw in general relativity for the first time since its formulation, more than a hundred years ago. From a more practical point of view, it was already anticipated that being able to detect GW allows us to broaden the frequency spectrum that we can study: we can now “hear” sounds we were deaf to before. Metaphorically speaking, we just gained a “sixth sense” to explore the Universe and we now have a chance to find answers to some of the most interesting questions in astrophysics and cosmology, possibly gaining more detailed information about the Big Bang. Finally, the search for GW motivates the development of new technologies which will have countless applications in many areas of physics and industry.

### 1.3 Report Structure

The structure of the report is outlined below, with a very brief descriptions of the content covered in each section.

- Section 2 presents the main results of General Relativity which will be needed by the reader throughout the report, setting up the mathematical formalism of the paper.
- Section 3 mainly aims to answer the second part of the report's question, explaining the importance of GWs in astrophysics and cosmology and their possible uses.
- Section 4 together with Section 5 focuses on the first part of the report's question, reviews past and present detector technology, from the first resonant mass detectors to LIGO.
- Section 5 describes the future of GW detection by presenting planned future detectors such as LISA as well as improvements to the already existing ones.
- Section 6 goes through the data analysis performed at LIGO on the two detected signals, explaining the important technique of matched filtering as well as other possible methods such as the excess power technique and the use of clustering algorithms.
- Section 7 presents a discussion of the results of the report and a final conclusion.

### 1.4 Primary Sources of GW

The four primary types of GW signals are *continuous*, *inspiral*, *burst* and *stochastic* gravitational waves, all having in common that they are produced by extremely massive, dense astrophysical bodies.

Continuous GW signals are emitted either by stable, orbiting systems of massive bodies or by fast-spinning bodies with irregularities in their structure. For the former case, systems produced are primarily black hole-black hole orbitals, black hole-neutron star orbitals or neutron star-neutron star orbitals. Systems containing bodies of similar masses tend to have long lived orbital states. As the bodies orbit each other, energy is slowly emitted in the form of gravitational waves, leading to a progressive shortening of the orbital radius and to an eventual merging/collision of the two bodies. For the latter case, neutron stars with an irregularity on their surface (such as a mountain) are responsible for GW emission. Neutron stars tend to spin about a central axis extremely fast. Due to the asymmetry in their shape, rotation energy is lost in the form of GW, until an equilibrium state is achieved. Both of these types of systems radiate energy slowly, and as such the GW signals emitted by them are rather weak, in comparison to the other sources of GW.

Inspiral GW are emitted in the final stages of continuous emission systems, and the binary systems become known as 'merger' systems. In these final stages, when the astrophysical bodies have approached each other enough, the orbital radius decreases at an increasing rate as the gravitational force acting on each body grows. The greater the difference in mass of the bodies in the binary systems, the faster the radiation of energy, and the more prominent the GW signal. As the orbital radius decreases at an increasing rate, so too does the frequency of the orbit increase, and correspondingly the frequency and amplitude of the GW that are emitted. Such orbital frequency increase leads to the

characteristic ‘chirp’ of merger systems. A more detailed discussion of this process is carried on in §3.3.2.

Burst gravitational waves are emitted by violent, highly energetic astrophysical phenomena, such as supernovae or gamma ray bursts. Burst emission also includes events or systems acting as sources, which have yet to be theorized and remain unknown. The signal is a powerful peak, normally stronger than from the aforementioned sources, and short in duration due to the nature of such events.

The final source of gravitational waves is the stochastic signal, which is analogous to the cosmic microwave background in observational cosmology. GW from random sources throughout the universe are expected to combine and create a very weak ‘background’ signal known as the stochastic signal (stochastic referring to the random nature such waves). The stochastic signal is theorized to link to the Big Bang - it being composed in part of the remnants of GW emitted during this time.

## 2 Mathematical Theory

General relativity has been described as one of the most beautiful theories in physics. The combination of philosophy and physics leading to complex and surprising results is a testament to this beauty. To proceed, it is necessary to develop some mathematical concepts in order to make it possible to understand the results derived from such reasoning.

In this section we consider why the Newtonian theory of gravity is incomplete and how it needs to be edited to be agree with special relativity. Moving into the realm of general relativity we derive the Einstein field equations and from them (taking appropriate limits) derive the existence of GW. A brief discussion of the production of GW from strong sources, such as black holes, will follow. The theory of strong GW production, however, will not be discussed as it is beyond the level of this review.

### 2.1 From Newtonian Gravity to General relativity

Special relativity dictates that distances in space time are only relative or are dependent on the frame of reference considered. Thus when we examine the Newtonian regime for gravity we find that there are contradictions. The central equation in Newtonian mechanics is

$$F_{12} = \frac{Gm_1m_2}{|\vec{r}_1(t) - \vec{r}_2(t)|^2}. \quad (1)$$

It describes how the force on two particles is inversely proportional to the square of the distance separating them. The force calculated by an observer is then dependent on the measured distance between particles. So observers in different reference frames would measure different forces. The postulates of special relativity, however, assert that the laws of physics are the same in all reference frames. Thus a different approach to gravity must be adopted so as to keep consistency with special relativity. This is the theory of general relativity.

The theory of general relativity is based on a concept known as the *Equivalence Principle*. This states that there is no local experiment which can distinguish between a reference frame in a gravitational field and a reference frame accelerating in the absence of a gravitational field. This is best illustrated by considering a person in an lift. There

is no experiment that can discriminate between a lift which is standing still on earth (i.e. in a gravitational field) or if it is accelerating at a constant rate in free space. The equivalence principle relies on one fundamental assumption: that the gravitational mass ( $m_g$ ) in the equation  $F = \frac{Gm_g M}{r^2}$  is the same as the inertial mass ( $m_i$ ) in Newton's second law  $F = m_i a$ . There is no physical reason why this identification should be the case, however this was the assumption made by Newton and Einstein alike. Many physicists have come up with experiments to test this hypothesis. Examples can be found in experiments such as the Eötvös experiment where the difference between the two quantities was found to differ by at most 1 part in 100 million.

Since this principle must apply to all laws of physics we must now deduce that a gravitational field will also have an effect on light. This can be demonstrated thus: if a light beam enters an elevator when it is accelerating in free space it will hit a point on the other side of the elevator which is below the position it entered at. If this system is now transferred into a uniform gravitational field (i.e. placed on earth) then using the equivalence principle the light must be bent in this gravitational field otherwise it would be possible to deduce that the system was in a gravitational field rather than accelerating in free space.

This principle can now be used to deduce that clocks are affected by their positions in gravitational fields (for further reading see Hartle's *Gravity: An Introduction to Einstein's General Relativity*<sup>58</sup>). Using this result we can conclude that gravity affects the rate at which clocks run and all clocks are affected in exactly the same way i.e. clocks further away from the source of a gravitational field will be affected more than those nearer to the source. This is the principle on which GPS (see §6.4 of Hartle's *Gravity*<sup>58</sup>) works. This type of explanation leads to the conclusion that space time is flat and that the intervals measured by clocks only appear to be changed when in different positions in the gravitational field. However, it is much simpler to conclude that the intervals measured are the same, all distances remain the same and it is the underlying geometry of space which is changing i.e. space-time is curved by gravity. This results leads us to the theory of general relativity (for a more in-depth introduction see Leonard Susskind's GR course lectures 1-3).

## 2.2 Principle of General Covariance

The principle of general covariance follows from the Equivalence principle. It states that physical equations will hold in a general gravitational field if they obey the following conditions:

- Equations hold in the absence of a gravitational field and they obey the laws of special relativity when the geometry of space time is flat and there is no curvature in space-time.
- The equation is generally covariant; it remains in the same form under a general coordinate transformation  $x \rightarrow x'$ .

This follows from the equivalence principle<sup>99</sup>. It is central to the formalism of general relativity. If it holds throughout general relativity it implies that if equations are true in one reference or coordinate frame then they will be true in all reference or coordinate frames. This principle then allows one to choose which ever coordinate frame is most useful (which can make the equations simpler) and the results from any calculations done in that frame will be true in all frames.

### 2.2.1 Newtonian Gravity: a geometric approach

Having established that space-time is curved, the Newtonian theory of gravity can be recast in a geometrical way. We define the line element in Newtonian Space to be

$$ds^2 = -\left(1 + \frac{2\phi(x^i)}{c^2}\right)(cdt)^2 + \left(1 - \frac{2\phi(x^i)}{c^2}\right)(dx^2 + dy^2 + dz^2) \quad (2)$$

where  $\phi(x^i)$  is the gravitational potential as a function of position. We can now use this line element to find the proper time between two points in Newtonian space-time. Then, treating the proper time as an action (for an explanation of action principle see Appendix A) it is possible to derive the classic Newtonian force law  $F = ma$ , i.e. to first order

$$\tau_{AB} \approx \int_A^B dt \left( \frac{1}{2} \vec{V}^2 - \phi \right). \quad (3)$$

Treating the integrand as a Lagrangian and applying the Euler-Lagrange equations the Newtonian force law is reproduced in the form  $\frac{d^2 \vec{x}}{dt^2} = -\nabla \phi$ .

### 2.2.2 Geometry of Special Relativity

The geometry of special relativity is, like in Newtonian gravity, a flat space-time but with the Minkowski metric applied to it. To describe space-time as being flat means that there exists one set of coordinates in which the metric of that space is constant. For further reading see<sup>43</sup>. To change from the flat space time of special relativity to the curved space-time of general relativity the metric must be free to vary across space-time.

## 2.3 Mathematical Interlude: Curved Geometries and Curvature

### 2.3.1 Covariant and Contravariant Coordinates

In order to use the principle of general covariance outlined in §2.2 we must understand how quantities transform. It is simplest to define the transformations for scalar quantities as they do not change when transformed from one coordinate system to another. As an example, the universal gravitational constant,  $G = 6.67 \times 10^{-11} m^3 kg^{-1} s^{-2}$  is the same regardless of what coordinate system is in use. However there are two ways in which vectors can transform. Here we have defined vectors as entities with one index which usually are represented by a  $n \times 1$  matrix.

$$A = \begin{pmatrix} x_0 \\ x_1 \\ x_2 \\ x_3 \\ \cdot \\ \cdot \\ x_n \end{pmatrix} \quad (4)$$

The first is the transformation of the contravariant vector where <sup>1</sup>

$$V'^{\mu} = V^{\nu} \frac{\partial x'^{\mu}}{\partial x^{\nu}}. \quad (5)$$

The second is the transformation of a covariant vector

$$V'_{\mu} = V_{\nu} \frac{\partial x^{\nu}}{\partial x'^{\mu}}. \quad (6)$$

---

<sup>1</sup>It should be noted that Einstein Summation convention is used through out this section



Where  $x'$  is the new coordinate system and  $x$  is the coordinate in the original system. The definitions above define covariant and contravariant vectors as entities with one index which transform as described. They also form the basis of how general tensors transform. A tensor with upper indices  $\mu, \nu, \dots$  and lower indices  $\alpha, \beta, \dots$  will transform like the product of covariant and contravariant  $U^\mu W^\nu \dots V_\alpha Y_\beta \dots$  hence

$$T'^{\mu\lambda} = \frac{\partial x'^\mu}{\partial x^\alpha} \frac{\partial x'^\lambda}{\partial x^\beta} \frac{\partial x^\gamma}{\partial x'^\nu} T_\gamma^{\alpha\beta}. \quad (7)$$

It is now possible to define a way in which an equation can be invariant in general relativity: if the equation is a tensor equation with the same upper and lower indices on either side then that equation will be invariant.

### 2.3.2 Metrics

The metric tensor is defined by <sup>2</sup>

$$g_{ab} = e_a \cdot e_b \quad (8)$$

with its inverse being

$$g^{ab} = e^a \cdot e^b. \quad (9)$$

Where  $e_a$  and  $e_b$  are the basis vectors in any coordinate system. The metric tensor defines the intrinsic geometry or curvature of the space on which it is defined. It can be used to define a general line element (a generalisation of pythagoras' theorem in any coordinate system). The line element  $ds^2$  is now defined by

$$ds^2 = g_{ab} dx^a dx^b. \quad (10)$$

Where  $dx^a$  or  $dx^b$  are infinitesimal intervals.

As the metric determines the intrinsic geometry of the space, it can be used to determine whether or not the space is curved. The metric itself however will not determine if the space is curved since its form is determined by the coordinates used to calculate it. Later in this section it will be shown that there is a tensor (called the *Riemann tensor*) which can encapsulate this.

### 2.3.3 Christoffel Symbols

*Christoffel Symbols* are entities which tell us how much the coordinate system changes as we move around it. Coordinate systems can cause vectors which are the same in one coordinate system (frame) to look different in another frame (note that here differentiation is viewed as the difference between two vectors which are very close together). Thus when we differentiate these vectors in the first system we find that the derivative is zero since there is no change. However when differentiating in the second frame where the vectors have changed it is found that the value of the differential is non zero thus the vectors are different in this coordinate system.

---

<sup>2</sup>Note that an alternate definition of the metric tensor is  $g_{\mu\nu} = \frac{\partial \xi^\alpha}{\partial x^\mu} \frac{\partial \xi^\beta}{\partial x^\nu} \eta_{\alpha\beta}$  Where  $\eta^\alpha$  are the coordinates in the old coordinate system and  $x^\mu$  are coordinates in the old system

To rectify this situation it is necessary to realise that the basis vectors are no longer constant. In normal n-dimensional Euclidean space the basis vectors  $e_i$  are the same at all points. However in a different coordinate system the basis vectors could change due to their position in the space. For example the radial basis vector  $e_r$  in a spherical coordinate system changes as a vector moves around the origin since it always must point away from the origin.

With this new information it is possible to define the differential of a vector as

$$\frac{\partial \vec{V}}{\partial x^\beta} = \frac{\partial V^\alpha}{\partial x^\beta} \vec{e}_\alpha + V^\alpha \frac{\partial \vec{e}_\alpha}{\partial x^\beta}. \quad (11)$$

The final term in the above equation is the term which is of interest here. It represents how much the coordinates change as we move through the system. Now we introduce the Christoffel Symbol to denote the coefficients in this expression.

$$\frac{\partial \vec{e}_\alpha}{\partial x^\beta} = \Gamma_{\alpha\beta}^\mu \vec{e}_\mu. \quad (12)$$

This is possible since the partial derivative in the second term is a vector so one must be able to express this as a linear combination of some basis vectors (for further reading on Christoffel symbols see Schutz<sup>87</sup>, §5.3. Alternative names in literature for Christoffel symbols are *affine connections* or *connection forms*).

### 2.3.4 Covariant Derivative

Using the definition of the Christoffel symbol from above it is now possible to define covariant differentiation, or differentiation in curved coordinates. Combining equations 11 and 12 gives

$$\frac{\partial \vec{V}}{\partial x^\beta} = \left( \frac{\partial V^\alpha}{\partial x^\beta} + V^\mu \Gamma_{\mu\beta}^\alpha \right) \vec{e}_\alpha \quad (13)$$

which we define as the covariant derivative, denoted by  $D_\beta$ . This new type of derivative deals with a changing coordinate system.

### 2.3.5 Tensors in GR

In relativity tensors are of special importance, since if equations involving tensors apply in one frame then they are true in all frames (as mentioned in §2.2). It is therefore useful to create quantities in tensor form.

**Stress Energy Tensor** The stress energy tensor (denoted  $T^{ij}$ ) is defined as the flux of  $x^\alpha$  momentum across a surface of constant  $x^\beta$ . Here  $\alpha$  and  $\beta$  run across 0,1,2 and 3 since we are dealing with 4 dimensional space time. Since the 0<sup>th</sup> component of 4-momentum is energy and the 0<sup>th</sup> component of a 4-vector is time then the  $T^{00}$  component corresponds to the flow of energy across constant time i.e. the energy density.<sup>(87 section 4.5)</sup>

**Riemann Tensor/Curvature Tensor** To explain what the Riemann tensor does it is necessary to examine the effect of taking a vector round a closed loop on a curved surface whilst keeping it parallel to itself. When the vectors returns to its original position one finds that the vector is no longer pointing in the same direction. This is a consequence of the curvature of the space in which the vector is moving. This mechanism is called *parallel transport*, and is illustrated in Figure 2:

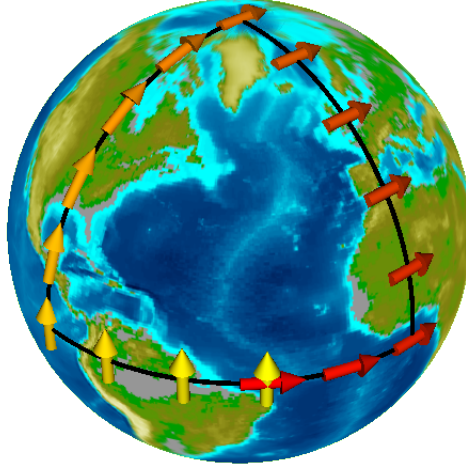


Figure 2: Parallel transport

If differentials are treated as if they were small displacements then two second-order differentials can be compared when the derivatives are taken in different orders. If the difference of these is non zero then it can be concluded that the space which the vector occupies is curved. This operation reduces to the equation

$$R_{srn}^t = \partial_r \Gamma_{sn}^t - \partial_s \Gamma_{rn}^t + \Gamma_{sn}^p \Gamma_{pr}^t - \Gamma_{rn}^p \Gamma_{ps}^t \quad (14)$$

This defines the *Riemann tensor*,  $R_{srn}^t$ , which quantifies the extent to which space is curved at particular points in that space. Two other entities can be made from this tensor the Ricci Tensor and the Ricci Scalar. The Ricci Tensor is a contraction of the Riemann tensor over 2 of its indices such that  $R_{\mu n}^\mu = R_{sn}$ . This tensor can be contracted even further with the metric tensor to define what is known as the Ricci scalar  $R = g^{ab} R_{ab}$ .

**Einstein Tensor** The two quantities above are very important in general relativity as they appear in Einstein's Field equations in the form of the Einstein tensor

$$G^{\alpha\beta} \equiv R^{\alpha\beta} - \frac{1}{2} g^{\alpha\beta} R. \quad (15)$$

Further explanation of this tensor will be given in the next section.

## 2.4 Einstein's Field Equations

As mentioned previously general relativity should reduce to Newtonian theory of gravity in the appropriate limit. It is instructive then to start by examining what the theory should look like in this approximation. Newtonian theory states that the source of gravitational fields is mass densities. It further states that the gravitational potential is determined by the equation

$$\nabla^2 \phi(r) = 4\pi G \rho(r). \quad (16)$$

This has the solution

$$\phi(r) = \frac{-GM}{r} \quad (17)$$

when the mass density is spherically symmetric - a solution which is only valid outside the mass distribution. When this equation and solution are considered from a relativistic point of view, however, they are evidently not relativistically invariant. An observer in a different reference frame would measure a different mass distribution and hence a different mass density. This would result in a different calculated value of  $\phi(r)$  to that derived by an observer in the lab frame. This equation is only true in one frame so is not relativistically invariant.

To make the equations relativistically invariant under any coordinate transformation (including Lorentz transformations) the stress energy tensor discussed earlier is used. It can be noted that the Newtonian theory only uses the  $T^{00}$  component of this tensor and so by using the whole tensor it is ensured that all coordinate frames are treated equally.

In searching for an equation which is similar to the Newtonian view of gravity, the form of the field equations for general relativity should be some tensor equation  $G^{\mu\nu} = kT^{\mu\nu}$ . This makes it true in all reference frames. It should be noted that the aim is to construct a tensor, or tensors, the elements of which consist of second derivatives of the metric. This is due to the Newtonian limit featuring a second derivative on the LHS of the equation (16).

Recalling the definition of the Riemann tensor and noting that the Christoffel symbols consist of derivatives of the metric (namely that  $\Gamma_{\beta\mu}^{\gamma} = \frac{1}{2}g^{\alpha\gamma}(\partial_{\mu}g_{\alpha\beta} + \partial_{\beta}g_{\alpha\mu} - \partial_{\alpha}g_{\beta\mu})$ , for derivation see<sup>87</sup>). Using this definition and noting that equation (14) involves derivatives of the Christoffel symbols it is seen that the Riemann tensor could be a candidate for this tensor  $G^{\mu\nu}$ . The Riemann tensor, however, has four indices and the tensor we seek only has two. We then contract the Riemann tensor over two of its indices. As we have seen, this process produces the Ricci tensor. The Ricci tensor contains less information than the Riemann tensor, but does describe the curvature of space and is made up of second derivatives of the metric. This process of contraction can be performed again to produce the Ricci scalar, denoted by  $R$ . This can also be made to have two indices by multiplication with the metric to produce  $g_{\mu\nu}R$ , which is called the *curvature scalar*.

The challenge that follows is that of determining the correct form of the field equations. To find this, the continuity equations for the stress energy tensor are invoked where  $D_{\mu}$  is the covariant derivative. This equation is simply an expression of the conservation of energy

$$D_{\mu}T^{\mu\nu} = 0. \quad (18)$$

Now since  $G^{\mu\nu} = kT^{\mu\nu}$  it follows that

$$D_{\mu}G^{\mu\nu} = 0. \quad (19)$$

As we have two candidates for this tensor we apply this equation to both of them to obtain the results

$$\begin{aligned} D_{\mu}(g^{\mu\nu}R) &= g^{\mu\nu}(\partial_{\mu}R) \\ D_{\mu}(R^{\mu\nu}) &= \frac{1}{2}g^{\mu\nu}(\partial_{\mu}R). \end{aligned} \quad (20)$$

It is now possible to combine these two equations in a linear combination such that their sum is zero. This then creates the Einstein tensor which was defined above. The resulting

field equations are then<sup>3</sup>

$$G^{\mu\nu} = R^{\mu\nu} - \frac{1}{2}g^{\mu\nu}R = 8\pi T^{\mu\nu}. \quad (21)$$

#### 2.4.1 Trace Reversed Field Equations

An equivalent, and sometimes more useful, formulation of the field equations is found by taking the trace of equation (21) and manipulating it so that it is possible to eliminate the factor of  $-\frac{1}{2}g^{\mu\nu}R$ . This results in the equation

$$R_{\mu\nu} = T_{\mu\nu} - \frac{1}{2}g_{\mu\nu}T. \quad (22)$$

Where  $T$  is the trace of the stress energy tensor.

### 2.5 Derivation of Gravitational Waves from Weak Sources

In general, solving Einstein's field equations is very difficult since there are no general solutions to these equations. This is because it is a system of ten coupled non linear differential equations (not sixteen as we would expect for a tensor with two indices because the metric tensor is symmetric under exchange of its indices). It is however possible to simplify matters considerably by imposing conditions on the system. One of these simplification is to consider what is called *linearised gravity*. This involves solving the equations in a system which only differs from flat space-time by a small perturbation  $|h_{\alpha\beta}| \ll 1$ . We can also impose other constraints on the system such as dealing with the far field approximation where we set  $T_{\alpha\beta} = 0$  (i.e. off-diagonal components) and only deal with the small perturbations  $h_{\alpha\beta}$ . This is equivalent to a system where there are no complicated interactions occurring which would produce strong GW (see §3 for a discussion of this).

In the far field approximation Einstein's (Trace Reversed) field equations reduce to the form

$$R_{\mu\nu} = 0. \quad (23)$$

Now, expressing the metric as flat space time with small perturbations

$$g_{\mu\nu}(x) = \eta_{mn} + h_{\mu\nu}(x) \quad (24)$$

and using the definition of the Ricci tensor and the fact that the Christoffel symbols consist of the metric and its derivatives, this expression for  $g_{\mu\nu}$  can be substituted into the far field approximation to obtain the equation<sup>4</sup>

$$\frac{1}{2}(-\square h_{\alpha\beta} + \partial_\alpha V_\beta + \partial_\beta V_\alpha) = 0. \quad (25)$$

Where

$$V_\alpha \equiv \partial_\gamma h_\alpha^\gamma - \frac{1}{2}\partial_\alpha h_\gamma^\gamma \quad (26)$$

and

$$h_\alpha^\gamma = \eta^{\gamma\delta} h_{\delta\alpha}. \quad (27)$$

---

<sup>3</sup>Notice the omission of the cosmological constant which would also be a solution and so the field equations would have to form  $G^{\mu\nu} + \Lambda g^{\mu\nu} = 8\pi T^{\mu\nu}$ .

<sup>4</sup>Here  $\square$  is the d'Alembertian operator. That is to say  $\square = -\frac{\partial^2}{\partial t^2} + \vec{\nabla}^2$ .

Now since the coordinates have been chosen arbitrarily we are free to choose any coordinate we want so that equation (25) can be simplified. This is called “choosing a gauge” and has much in common with choosing a gauge in electromagnetism. The appropriate gauge here is to choose

$$\partial_\gamma h_\alpha^\gamma - \frac{1}{2} \partial_\alpha h_\gamma^\gamma = 0 \quad (28)$$

i.e. choosing  $V_\alpha = 0$ . This is called the Lorentz gauge. Using this condition the linearised field equations now become

$$\square h_{\alpha\beta}(x, t) = 0. \quad (29)$$

This is a wave equation which is solved by perturbations which are plane waves of the form

$$h_{\alpha\beta}(x) = a_{\alpha\beta} e^{i\vec{k} \cdot \vec{x}} \quad (30)$$

where  $a_{\alpha\beta}$  is a  $4 \times 4$  symmetric matrix which gives the amplitude of the wave in various coordinate directions. From the field equations of general relativity more conditions are placed on this condition which require that the  $a_{\alpha\beta}$  components must satisfy what are known as the transverse traceless conditions. This means that the GW oscillate perpendicular to their direction of travel, in the same way as electromagnetic waves. So, only the components of  $a_{\alpha\beta}$  which are perpendicular to the direction of travel will be non zero whilst the traceless condition says that the trace of  $a_{\alpha\beta} = 0$ . These conditions leave this matrix with the following form

$$a_{\alpha\beta} = \begin{bmatrix} 0 & 0 & 0 & 0 \\ 0 & a & b & 0 \\ 0 & b & -a & 0 \\ 0 & 0 & 0 & 0 \end{bmatrix}. \quad (31)$$

This matrix describes the propagation of a GW traveling along the z-axis which has the form

$$h_{\alpha\beta}(z, t) = a_{\alpha\beta} e^{i\omega(z-t)}. \quad (32)$$

From this expression it can be seen how different polarisations of GW arise. Since the matrix can be split up into two parts (one proportional to  $a$  and one proportional to  $b$ ) there are two different polarisations possible. The part proportional to  $a$  is known as the plus-polarisation whilst the part proportional to  $b$  is known as the cross-polarisation.

## 2.6 Solving 4d Wave Equation with Source

It was shown above that for linearised gravity (approximations to first order) the perturbations in space time which were produced by far off sources obeyed the wave equation  $\square h_{\alpha\beta} = 0$ . This is, however, not a source equation. The complete equation with the stress energy tensor as a source is<sup>5</sup>

$$\square h^{\alpha\beta} = -16T^{\alpha\beta}. \quad (33)$$

This wave equation can be solved in the simple case when the source  $j(x)$  is a 4-dimensional delta function. The delta function source is spherically symmetric which implies that the solution will only depend on the distance from the source,  $r = |\vec{x}|$ , and time,  $t$ . So this solution must satisfy the spherical wave equation in polar coordinates, namely

$$-\frac{\partial^2 g}{\partial t^2} + \frac{1}{r^2} \frac{\partial}{\partial r} \left( r^2 \frac{\partial g}{\partial r} \right) = 0. \quad (34)$$

---

<sup>5</sup>These equations are not tensor equations so they will only hold in a Cartesian coordinate system.

Where  $g = g(t, r)$  is the solution to the wave equation. This equation could have two possible solutions: one propagating inwards and one outwards. We will only consider the solution which propagates outwards called the causal solution which will have the form

$$g(t, r) = \frac{1}{r} [O(t - r)]. \quad (35)$$

Where  $O(t - r)$  represents a wave traveling away from the source at the speed of light. To find this solution to the wave equation we integrate the 4-dimensional wave equation with a delta function source over a small volume

$$\int_{\epsilon} d^3x \left[ -\frac{\partial^2 g(x)}{\partial t^2} + \vec{\nabla}^2 g(x) \right] = \int_{\epsilon} d^3x \delta(t) \delta^{(3)}(\vec{x}) = \delta(t). \quad (36)$$

Now, we note that the first term on the left hand side varies negligibly time so as  $\epsilon \rightarrow 0$  that term will vanish, leaving a volume integral over a small sphere. This can be turned into a surface integral using the divergence theorem making the integration and limits easier to evaluate. The results of this calculation are

$$g(t, r) = -\frac{\delta(t - r)}{4\pi r}. \quad (37)$$

If the source is not just a delta function but is distributed over many points in space time then the solution can be found by integrating over the whole source with each point weighted by  $j(t', \vec{x}')$ . So, the solution will be

$$f(t, \vec{x}) = -\frac{1}{4\pi} \int d^3x' \frac{[j(t', \vec{x}')] }{|\vec{x} - \vec{x}'|}. \quad (38)$$

If the source of the wave equation is taken to be an oscillating source  $j(t, \vec{x}) = j_{\omega}(\vec{x}) \cos(\omega t)$  and we examine the case where  $\lambda \gg R_{\text{source}}$  it can be shown (Hartle<sup>58</sup> page 495) that

$$f(t, \vec{x}) \rightarrow -\frac{1}{4\pi r} \int d^3x' j(t - r, \vec{x}'). \quad (39)$$

### 2.6.1 Solution in Linearised Gravity

Using equation (38) we can immediately generalise the results of the previous section to the case of linearised gravity since it is a set of ten flat-space wave equations, each with their own source. This leads to

$$h^{\alpha\beta}(t, \vec{x}) = 4 \int d^3x' \frac{[T^{\alpha\beta} t', \vec{x}']}{|\vec{x} - \vec{x}'|}. \quad (40)$$

This result only holds for the metric perturbations in Cartesian coordinates and so it is not a fully general equation.

## 2.7 Production of weak gravitational waves

The general solution for linearised gravity above (40) can be used to examine what type of characteristics the source of these weak gravitational waves will have. In this derivation it is assumed that  $r \gg R_{\text{source}}$  and  $\lambda \gg R_{\text{source}}$ . Using (39) with the source as the stress energy tensor, and the flat space conservation law  $D_{\mu} T^{\mu\nu} = 0$  to first order, it is possible to derive characteristics of the source. This derivation leads to the conclusion



that the perturbations in space time due to the source are approximately proportional to the second derivative of the second mass moment <sup>6 78</sup>

$$h^{ij}(t, \vec{x}) \rightarrow_{r \rightarrow \infty} \frac{2}{r} \ddot{I}^{ij}(t - r). \quad (41)$$

This equation is often known as the quadrupole formula in general relativity as it relates the rate at which GW are produced to the change of the quadrupole moment of the system,  $\ddot{I}^{ij}$ . Another quantity can be derived from this second mass moment which is known as the reduced quadrupole moment tensor  $\bar{I} := I_{jk} - \frac{1}{3}\delta_{jk}I_l^l$ . This quantity can be used to express the luminosity of a GW or the energy carried away from a source by GW. The result is found by calculating the flux of a GW through a generalised detector and then integrating over a sphere which indicates the luminosity of the wave. The formula holds for weak gravitational fields and slow velocities and for highly relativistic sources of gravitational waves

$$L = \frac{1}{5} \langle \ddot{\bar{I}}_{ij} \ddot{\bar{I}}^{ij} \rangle. \quad (42)$$

Where the angle brackets denote the time average over one period of oscillation (see §9.4 of Schutz<sup>87</sup>).

## 3 Single and Binary sources of Gravitational Waves

### 3.1 Gravitational Wave Astronomy

Now that the mathematical formalism and the main aspects of the theory have been presented, it is possible to see how these can be put into practice, allowing for both the analysis of data detected in new observations and the development of models for physical events which are still not fully understood. One of the research areas in which the study and understanding of GW is of fundamental importance is astrophysics. This is the case since all the main sources of GW are astrophysical bodies such as black holes or neutron stars. The very first indirect experimental evidence of the existence of the waves came from the observation of energy loss of pulsar PSR1913+16 by Hulse and Taylor in 1975<sup>59</sup>; today, after the direct detection observed by LIGO in 2015, the era of GW astronomy has officially begun.

Since GW interact extremely weakly with cosmic dust or stellar envelopes, they can travel past such astrophysical barriers and reach us even when most of the electromagnetic radiation is blocked and undetectable. This opens up a whole new perspective on the universe by massively broadening the spectrum of signals that can be studied and analysed. GW can be used to probe highly relativistic phenomena which have eluded scientists until now due to the lack of direct experimental data. In this section we outline some of the most important of these phenomena and astrophysical events, such as the merging of black holes and the explosion mechanism of the supernova. We begin by discussing GW emitted by binary systems, not only because waves emitted from this kind of source are those that were detected at LIGO, but also because they are expected to be among the most prolific sources in the Universe.

---

<sup>6</sup>This quantity here is defined as  $I^{ij} \equiv \int d^3x \mu(t, \vec{x}) x^i x^j$ . It is not the inertia tensor however it is related to it.

<sup>7</sup>It should be noted here that this derivation does not take into account first order non-linearities, however the result still holds in general for a more complete derivation see<sup>75</sup>

<sup>8</sup>There are different conventions for the definition of the quadrupole moment which vary from text to text here we are using the conventions from Hartle<sup>58</sup> which in turn follows from<sup>75</sup>



## 3.2 Binary System Gravitational Wave Emission

Binary astrophysical systems which emit GW fall into three major categories of combinations of neutron stars and black holes. As mentioned in §1.4, the three distinct binaries are neutron star - neutron star (BNS), neutron star - black hole (BHNS) and black hole - black hole (BBH). The mechanism of GW emission is very similar over all three. All consist of two supermassive bodies orbiting around a common center of mass. In contrast to the Newtonian prediction, the orbital radius of the binaries decreases with time, due to radiation of energy in the form of GW in accordance with general relativity. Eventually the two astrophysical bodies coalesce to form either a more massive neutron star, or more commonly a more massive black hole.

The binary coalescence process is divided into three phases: inspiral, merger and ring-down. The inspiral phase labels the period of time when the astrophysical bodies orbit one another, until they coalesce. At the early stages of their orbital journey when their orbital radius is relatively large (or in the case that the bodies have similar masses and hence a more stable orbit) the system emits continuous GW. If the masses are non-similar or the orbit is eccentric, continuous GW signals are not detected. As the orbital radius decreases, more energetic, inspiral GW are produced due to the increased rate of energy loss in the binary system. As the bodies approach coalescing distance, the GW energy and frequency peaks<sup>7</sup>. From the moment the coalescence begins until it ends is known as the merger phase. Following the merger phase, the two bodies become a single, deformed, unstable body, which continues to radiate weaker GW until the deformation has been eliminated and a stable state achieved. This final phase is known as the ringdown phase.

## 3.3 A Closer look at Neutron Star Binary - Wave Production Mechanism and Predicted Waveforms

### 3.3.1 What are Neutron Stars?

Neutron stars are massive compact astronomical objects which represent one of the possible end states of the life of a massive star. Massive stars have mass greater than 6–8 times that of our Sun. Neutron stars are formed from the collapse of the core of such a dying star, after its outer layers are expelled via a supernova explosion. As mass is added to the core by shell Si-burning, the core becomes unstable and undergoes a gravitational collapse. The gravitational pull in the core is so strong that it induces net electron capture on nuclei and free protons, hence decreasing the total lepton number<sup>33</sup>. The collapse of the core comes to rest when its internal pressure (enhanced by the increasing density) balances the gravitational force. Today, several accurate mass determinations for neutron stars are available, and they all lie in the narrow range of 1.25–1.44 solar masses<sup>33</sup>.

The study of the structure of neutron stars is of great importance - for determining both the properties of nuclear matter at high densities and the behavior of the nuclear symmetry energy near the nuclear saturation density<sup>69</sup>.

As previously mentioned, neutron stars are often found in binary systems, which consists of two rotating about a common centre of mass and the system undergoes a loss of energy due to the emission of GW, which causes the orbits to decay and leads to the coalescence of the two bodies. According to the theoretical predictions and simulations, the final burst of gravitational radiation emitted in this process carries direct information about the neutron star fluid, and, in particular, about the equation of state of nuclear matter at extreme densities<sup>46</sup>.

For this reason the detection of GW emitted by coalescing binary neutron stars would present an opportunity to probe the internal structure of these astronomical bodies and acquire information which is of crucial importance both in astrophysics and nuclear physics. In the rest of this sub-section we illustrate the theoretical models which allow this analysis to be performed.

### 3.3.2 Point-Mass Approximation

In this sub-sub-section, calculations for the inspiral phase dynamics are examined. For simplicity, the BNS system is considered. During the inspiral stage, the neutron stars are far away from each other and relativistic effects are relatively weak, therefore an analytic perturbative approach can be used to describe their dynamics<sup>85</sup>. Throughout the calculations, the neutron stars are taken as point-particles. This approximation is reasonable when the objects are far away from each other, but it fails to describe the merger and ringdown stages, during which relativistic interactions are much stronger and the effects of the finite mass of the neutron stars become important. For this reason, by comparing the point-mass results to the real detected signal and studying how the latter is distorted away from the former, we can gather information about the tidal forces inside the neutron stars, which directly depend on their equation of state. For a more complete discussion of the system considered, see<sup>85</sup>.

We consider two neutron stars of equal masses orbiting with an instantaneous radius  $R(t)$  and instantaneous frequency  $\omega(t)$ . For simplicity, we take the x-y plane to be the plane of the orbit and the centre of the orbit to be the origin of the frame of reference. In this model the position of one body is denoted  $x_1 = R$  at  $t = 0$ . The positions of both neutron stars is then

$$x_1(t) = -x_2(t) = R \cos(\omega t); \quad (43)$$

$$y_1 = -y_2 = R \sin(\omega t) \quad (44)$$

$$z_1 = z_2 = 0. \quad (45)$$

We use Kepler's Third Law to find the relation between  $\omega$  and  $R$ ,

$$\omega^2 = \frac{GM}{4R^3}. \quad (46)$$

Also note that the total energy  $E$  of the system (kinetic + gravitational potential),

$$E = -\frac{GM^2}{4R}. \quad (47)$$

Knowing the coordinates of the body allows one to compute the second mass moment  $I^{ij} = \int d^3x \mu(t, \vec{x}) x^i x^j$  where  $\mu(t, \vec{x})$  is the rest-mass density of the bodies. The third time-derivative of the reduced quadrupole moment tensor can then be evaluated as

$$\ddot{\ddot{I}} = \begin{pmatrix} \sin(2\omega t) & -\cos(2\omega t) & 0 \\ -\cos(2\omega t) & -\sin(2\omega t) & 0 \\ 0 & 0 & 0 \end{pmatrix}. \quad (48)$$

We find the luminosity

$$L = \frac{128}{5} \frac{GM^2}{c^5} R^4 \omega^6. \quad (49)$$

We can then equate the rate of energy loss  $\frac{dE}{dt}$  to the negative of the luminosity and set up a differential equation for the separation  $R(t)$

$$\frac{dE}{dt} = \frac{dE}{dR} \frac{dR}{dt} = -L \Rightarrow R^3 \frac{dR}{dt} = -\frac{8}{5} \frac{G^3 M^3}{c^5}. \quad (50)$$

Integrating from the present time  $t$  to a future time  $t_{coal}$  when  $R = 0$  yields

$$R(t) = \left[ \frac{32}{5} \frac{G^3 M^3}{c^5} (t_{coal} - t) \right]^{\frac{1}{4}}. \quad (51)$$

From this expression we can find the gravitational wave frequency  $f = \frac{2\omega}{2\pi}$

$$f_{GW} = \frac{1}{4\pi} [2 \times 5^3]^{\frac{1}{8}} \left[ \frac{c^3}{GM} \right]^{\frac{5}{8}} \frac{1}{\tau^{\frac{5}{8}}}. \quad (52)$$

Where  $\tau$  is defined as the time remaining before coalescence. We observe the  $\tau^{-\frac{3}{8}}$  dependence of the frequency, which gives rise to the characteristic “chirp” in the detected waveform. This simple treatment drastically simplifies the structure of rotating objects, therefore it can be used as an extreme simplification of the coalescence of a BBH or a BHNS system, with some slight modifications and consideration of applicability. In the case of the BNS system, the spin of both the system components is negligible. When black holes replace one or both neutron stars, the spin no longer maintains a negligible contribution to the GW emission, and leads to significant distortions in the predicted waveform<sup>85</sup>. A precession of the orbital plane is caused by the black hole spin, thus altering the orientation of the waveform with respect to an observer, creating a modulation of the observed waveform. The spin also contributes to the orbital decay period and therefore also to the phase of the waveform and its amplitude, due to spin-orbit and spin-spin interactions. The point mass approximation thus stands as a sufficient model for a static black hole system however due to the aforementioned reasons this simple model breaks down when considering non-static (spinning) black hole merger systems.

### 3.3.3 Equation of State of a Neutron Star

After looking at the predicted gravitational signal emitted by point-like objects, we can now examine the expected waveform for two neutron stars with finite masses in the range of 1.25 - 1.44 solar masses.

The cores of neutron stars can be described as polytropic fluids<sup>46</sup>. These are fluids which obey to a polytropic equation of state (EOS)

$$P = k\rho_*^n. \quad (53)$$

Where  $P$  indicates the internal pressure,  $k$  is a constant of proportionality,  $p_*$  is the rest density of the fluid and  $n$  is called polytropic index.

The polytropic index has been shown to be equivalent to the pressure derivative of the bulk modulus<sup>100</sup>, meaning that a high polytropic index implies that even a small variation in pressure can lead to a large variation in the fluid’s compressibility. For this reason the polytropic index is said to give the “stiffness” of an equation of state (EOS). A stiff EOS is capable of maintaining long-lived deformed states in self-gravitating fluids such as neutron matter<sup>46</sup>. Several simulations of coalescing binary neutron stars have been carried out, in order to study the hydrodynamical properties of the final merger<sup>26</sup>.

Most of the simulations are performed using *Post Newtonian* (PN) algorithms, which give approximate solutions to Einstein’s field equations by making an expansion in small

parameters which represent deviations from Newton’s law of gravitation<sup>26</sup>. PN effects, combined with finite-sized fluid effects noticeably increase the critical binary separation at which instability sets in, thus decreasing the frequency of the signal. *Smoothed Particle Hydrodynamics* (SPH) simulations were performed, taking as initial conditions irrotational nuclei with shapes of tidally stretched ellipsoids. The nuclei are irrotational because the timescale of viscous tidal forces is expected to be much longer than the inspiral timescale, therefore in a frame co-rotating with the binary any rotation of the ellipsoids around any of their axes can be ignored, as well as spurious oscillations around their equilibrium positions<sup>46</sup>. Simulations show that after the merger a central remnant core is formed, surrounded by a tenuous halo. The final result is a *differentially rotating object* (DRO) that is stabilized against the gravitational collapse by rotation and thermal pressure contributions.

As has been shown in previous sections, GW are formed by quadrupole oscillations and so a spherically symmetric object cannot emit gravitational radiation, because of the lack of a monopole term in the expansion of the waveform. As a consequence, the intensity of the GW at late times after the merger depends on how long the ellipsoidal deformation will persist, which is determined by the stiffness of the EOS. For a soft EOS, the remnant will rapidly collapse to a spherical shape, while for a stiff EOS the deformation will be much greater and last for longer times<sup>46</sup>. From this discussion we can therefore conclude that specific characteristics of GW spectrum can allow us to narrow the constraints on the EOS of neutron stars.

## 3.4 Single and Binary Black Hole Systems

### 3.4.1 What are Black Holes?

Black holes are solutions to Einstein’s field equations, and are regions in space-time from which not even electromagnetic radiation may escape, due to the incredible magnitude of the gravity in those regions. Black holes are described by properties allowed by the *no-hair* theorem which states that any black hole is completely characterised by only three externally observed parameters; mass, angular momentum and electric charge. Nothing, aside from these three properties, can be understood about the matter which falls in a black hole from an outside observer. So far, from solutions to Einstein’s field equations and relating principles, four different ‘categories’ of black holes have emerged, known as *metrics*. The four metrics found to date are the non-rotating and non-charged; charged and non-rotating; non-charged and rotating, and the charged and rotating black holes. Each of these are labelled as Schwarzschild, Reissner–Nordström, Kerr and Kerr–Newman metrics, respectively. To current understanding, all metrics when found in binary systems should produce GW. Furthermore, black holes are also separated into different types according to their mass and origin of creation. Discussed below is the main type of paramount interest.

Certain black holes represent a possible final state in the lifetime of a supermassive star. As explained previously: during the final stages of the life of a supermassive star, mass in the outer layers of the star is expelled via supernovae. Due to the instability of the core, gravitational collapse follows. If the mass of the remaining core surpasses the *Tolman–Oppenheimer–Volkoff* limit, then neutron degeneracy is overpowered by the gravitational force, meaning a neutron star is not a stable state and the implosion continues indefinitely. Hence, a black hole is formed. Black holes of this type are known as *stellar black holes*, and typically are of several solar masses, ranging up to roughly eighty solar masses.<sup>27</sup>

### 3.4.2 What knowledge can be extracted from gravitational wave signals?

The GW signals detected from binary systems offer a lot of information about the system, ranging from its evolution in time to its underlying physical properties. One of the most fundamental pieces of information which the GW signal contains are the masses of the two bodies. The masses are determined from the “chirp” signal, as theory predicts particular masses to emit specific chirps.<sup>11</sup> These masses can then in turn broaden the understanding of stellar black holes. In addition, the measured GW luminosity of the system, which is determined from the chirp mass (the mass ejected from the system in the form of gravitational wave energy) leads to one of the most reliable methods of calculating the distance to the system itself. The reliability of this method stems from the fact that GW interact very weakly with the intermediary matter, between the source and the observer. As such knowing (and confirming) the red-shift from electromagnetic sources, in combination with the GW signal, will allow for the most dependable mapping method of these binary systems.<sup>49</sup>

GW signals allow for the understanding of the creation mechanisms for BBH systems. BBH systems are created mainly by two different processes. The first relates to the fact that massive stars are most often found in binary systems. As such, when they reach the final stages of their lifetimes, both can become black holes (or neutron stars) leading to the creation of BBH/BHNS systems. The second mechanism involves dense star clusters. Supermassive stars which become black holes/neutron stars in these clusters move to regions of higher density within the cluster by dynamical friction.<sup>9</sup> Eventually, these black holes/neutron stars meet similarly formed and moved partner black holes and form BBH/BHNS systems. By measuring the precession and spin-alignment of BBH systems, one can determine which of the two mechanisms lead to the creation of BBH systems, as large precession and non-spin-alignment imply the dynamical forming of two black holes meeting at the centers of dense stellar clusters.<sup>9</sup> Furthermore, parameter estimation analysis of the gravitational waveform from BBH systems constrains the spin magnitude value for single black holes. Therefore, with appropriate analysis GW signals provide information concerning BBH system creation and yield limits for black hole spin magnitude values.

BBH and BHNS systems experience a phenomenon known as a ‘kick’ when the two bodies merge. The kick is a recoil effect due to the emission of GW. As the bodies orbit anisotropically, there is a net emission of angular momentum and by conservation of momentum, a recoil effect is felt by the post-merger remnant. In certain models was predicted to be a barrier for the existence of BBH merger systems. With the detection of GW of GW150914 by LIGO, it was shown that kicks are not always strong enough to prohibit the creation of BHNS or BBH systems, in either dynamic or isolated binary system creation. Moreover, by the detection of the GW150914 BBH merger, theories of the cosmos including the idea that kicks should be large enough to prohibit the creation of BBH/BHNS systems, or those which exclude BBH/BHNS, are falsified to an extent. Black hole kicks, depending on the ‘direction’ in which they expel the final product of the binary system, cause the last part of the gravitational waveform to be blueshifted or redshifted accordingly.<sup>51</sup> Thus, black hole kicks offer an entirely new GW observable. Using numerical relativity to compare the measured values, this type of observable will offer a method with which to test whether linear momentum is carried by GW, as predicted by general relativity. General relativity has undergone stringent tests in weak gravity regimes, yet GW offer the first possibility of testing the theory in the most extreme

scenarios of strong gravity. Thereby, with further detection and progressive development, the theory of general relativity will be improved and, if necessary, refined to include observational results.

GW signals provide the opportunity to probe the internal structure of a black hole for the first time since their discovery. The inspiraling bodies lead to a deformation on one another due to tidal interactions, in a similar way to that of the moon causing tides on Earth. This deformation can be easily imagined as a slight ‘bump’ on the event horizon of a black hole.

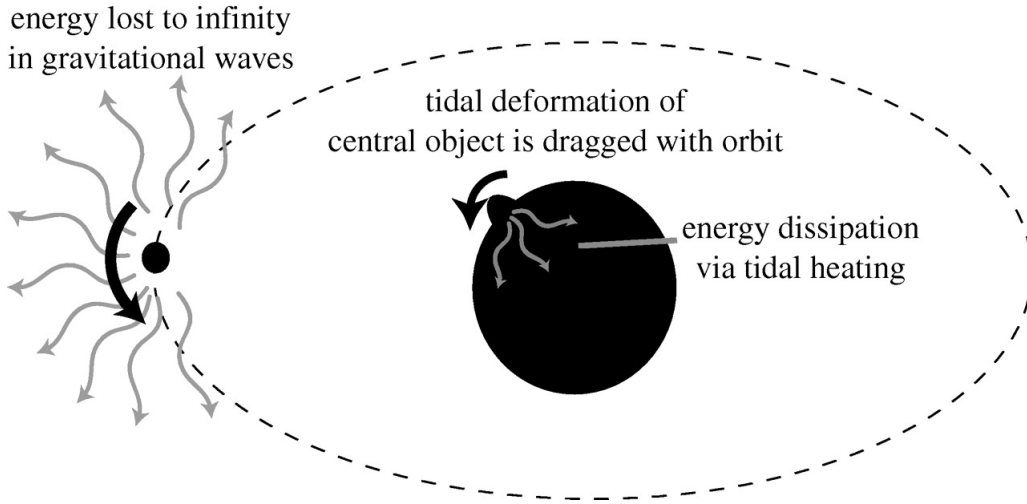


Figure 3: Tidal deformation due to the gravitational effect of one body on the other, depicting how internal structure may be probed via energy difference calculations<sup>49</sup>

Such tidal interactions are, in essence, energy being taken from the orbit and absorbed by the bodies, in order to produce the deformation. The energy of the GW emitted by the binary systems depends on the external space-time structure rather than their internal structure<sup>49</sup>. The precession rates of these systems indicates their external structure, and as such the energy of the GW signal may be calculated. From the decay of the inspiralling object, the energy lost in the orbit may be determined by an observer. Calculating the difference between the energy lost in the decay and that of the predicted GW emission will yield the energy maintained in the system from tidal interactions, and in this way the GW signal serves as a probe for the internal structure of black holes.<sup>49</sup> Such calculations and understanding of black hole space-times allows for a clearer picture of the merger phase and how the topological nature of the black hole systems evolves when approaching coalescence. According to simulations<sup>38</sup>, the merger phase begins by both black holes morphing into a ‘duckbill’ shape.



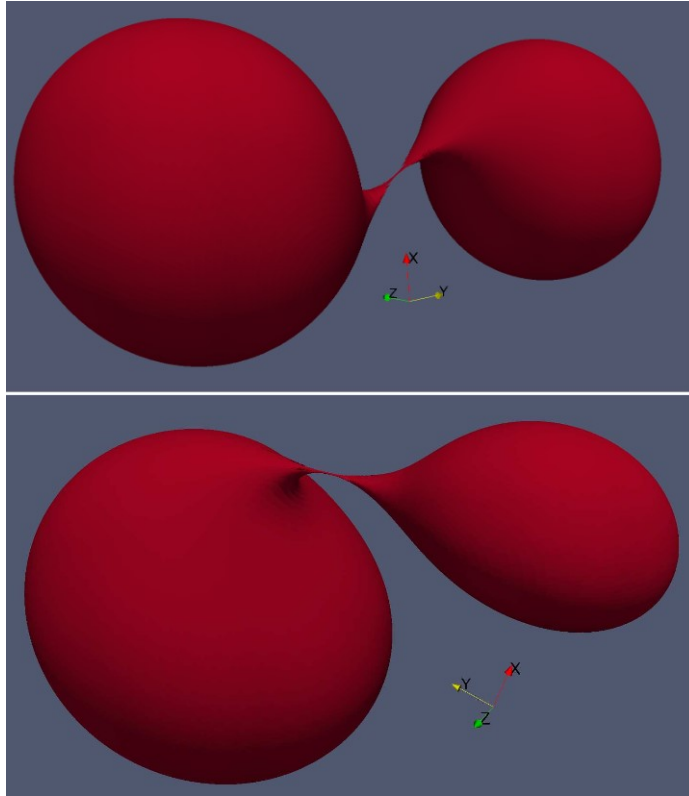


Figure 4: Upper panel depicts non-spinning equal mass black hole duckbill shapes, lower panel depicts generic BBH merger duckbill shapes. Both as slices at the exact time of merger phase initiation<sup>38</sup>

This phase persists until the two event horizons cross over and eventually the black holes coalesce and enter the ringdown stage. With simulations complimenting the tidal interaction theories, more may yet be understood about the time evolution of the space-time structure of the new black hole in its ringdown phase.

### 3.5 A Closer look at Supernovae - Gravitational Wave Bursts

Among the different expected GW production mechanisms, the class called “bursts” refers to transient states of poorly known or unknown phase evolutions. The main example of such bursts are supernovae explosions<sup>85</sup> which will be discussed in this sub-section.

#### 3.5.1 The Supernova Mechanism

As explained in §3.3.1, supernova explosions occur at the end of the life of a massive star, when the outer layers are expelled and its core collapses into a neutron star or a black hole. When the catastrophic gravitational collapse sets in, the inner core is compressed to incredibly high nuclear densities ( $\sim 2.6 \times 10^{14} \frac{g}{cm^3}$ ) causing its EOS to stiffen suddenly. As a consequence, the inner core rebounds into the still collapsing outer core, creating a so-called “core bounce”. This process gives rise to a hydrodynamical shock wave that propagates radially outwards causing the ejection of the outer layers of the star in the supernova explosion<sup>78</sup>.

While it was originally believed that a prompt hydrodynamic explosion would follow the shock creation, more recent studies show that this cannot be the case, since photodissociation of infalling heavy nuclei into nucleons in the core and the ejection of neutrinos from the post-shock region would drive energy away from the shockwave and prevent

the explosion. Therefore there must exist a mechanism which transfers the gravitational energy of the core back to the outer layers of the star, providing the necessary kinetic energy<sup>78</sup>.

The exact nature of the core-collapse supernova mechanism is a fundamental unsolved problem in astrophysics. Traditional observational methods have so far failed in investigating what happens inside collapsing cores because most of the electromagnetic radiation is shielded inside them. On the other hand, the gravitational radiation which is produced during the process will travel from the inside of the core to an observer without interactions with intervening matter, therefore the study of the GW spectrum can provide information about the process leading to supernova explosions<sup>79</sup>.

In the following sub-sub-sections the main hypothesis on the nature of the core-collapse mechanism will be outlined, together with the expected GW signature from each.

### 3.5.2 Neutrino Mechanism

The fundamental idea of the neutrino mechanism is that the central core shock is revived by neutrinos and antineutrinos which are emitted from the core. Neutrinos of all flavours would transport the gravitational energy released in the collapse to the outer stellar mantle, igniting the explosion<sup>78</sup>. The motion of the neutrino is modelled as a convective process: initially neutrinos are in the *proto-neutron star* (PNS) core, but then leak out towards its surface until they reach the boundary of the *gain region* which is defined as the region beyond which neutrino heating processes dominate over neutrino cooling processes. The net neutrino heating is stronger in the inner boundary than on the outer boundary, forming a negative entropy gradient which causes neutrinos to move back towards the central region of the PNS. Thus convection is established<sup>78</sup>.

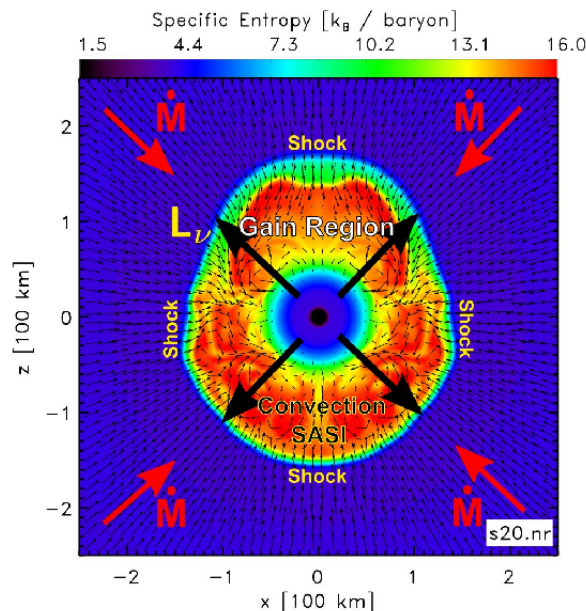


Figure 5: The core of a non-rotating SN where the neutrino mechanism is taking place. In the picture, the entropy distribution is shown using different colours. We see that outside the >Gain Region entropy drops, this induces neutrinos to overturn and perform convective motion. Velocity vectors are superimposed and allow to visualize the flow patterns. We also notice the core deformation due to the early phase of SASI<sup>78</sup>.

According to the model, the neutrino convection is combined with a *standing accretion shock instability* (SASI). SASI is a hydrodynamical instability of the spherical shock wave



in the PNS accretion flow. This instability causes turbulence which enhances the energy transfer towards the mantle of the star<sup>61</sup>. Because of the turbulent and non deterministic dynamics inside a supernova, the GW emitted by neutrino convection and SASI processes will be stochastic in nature i.e. of random and uncorrelated polarisations. Furthermore, the GW production by these mechanisms is much greater in slowly rotating or non-rotating stars.

### 3.5.3 Magnetorotational Mechanism

It is believed that a small fraction of supernova progenitors is made up by stars with rapidly rotating iron cores (periods of the order of seconds)<sup>78</sup>. Under gravitational collapse, the drastic decrease in radius would lead to an increase in rotational speed, due to conservation of angular momentum, creating a spinning PNS with period in the order of milliseconds and a differentially rotating postshock outer region. A supernova explosion could then be ignited by converting the huge rotational energy of the system into kinetic energy of its outer layers. In the magnetorotational mechanism the rotational energy is stored into a strong magnetic field generated by the rotating core<sup>78</sup>. Numerous simulations<sup>74</sup> have shown that exponentially growing *magnetorotational instability* (MRI) leads to jet-driven bipolar explosions along the core's rotation axis. These explosions would transfer the energy to the outer layers of the star, causing the supernova explosion.

The differentially rotating, rapidly spinning core in this kind of star is expected to produce strong GW emissions because of the centrifugal distortions it is subjected to. The GW spectrum is predicted to have a distinctive small peak right before the bounce and a large negative peak when the bounce occurs. Due to the first phase of the collapse being axisymmetric, the first emitted waves will be linearly polarised<sup>78</sup>.

### 3.5.4 Acoustic Mechanism

The model of the acoustic mechanism hypothesises that the energy is transferred from the supernova core to the outer mantle by strong acoustic waves. The origin of the sound propagation would be the oscillations of the pulsation modes of PNS inner core<sup>32</sup>. Simulations have shown that the anisotropic accretion process and turbulence can excite strong pulsations (pulsations are described by Legendre Polynomials with  $l = 1, 2$ )<sup>32</sup>. These pulsations can then decay by emitting sound waves, which are excellent carriers of energy and momentum. As previously stated, in the case of rapidly rotating stars the SASI is inhibited, therefore the acoustic mechanism would be mostly suppressed. Furthermore, in presence of strong rotations the magnetorotational mechanism would ignite the explosion much faster than the acoustic one (the acoustic timescale is around 550ms)<sup>78</sup>.

The early GW emitted by a supernova exploding via the acoustic mechanism are similar to the ones emitted by the neutrino-SASI mechanism. The most distinctive feature of their spectrum can be observed at later times, when the wave emission is mostly driven by the PNS core pulsation (rather than the accretions process) and they have the frequencies of the quadrupole components of the oscillations<sup>78</sup>. Since the quadrupole components depend on the PNS structure, the waves carry direct information about the inner core of supernova.

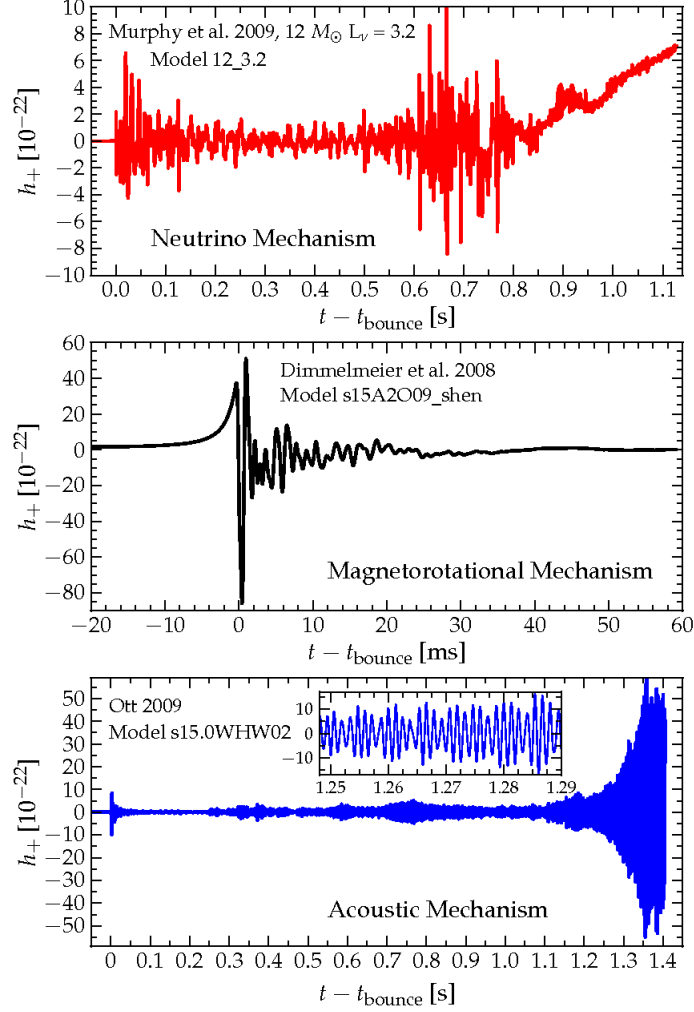


Figure 6: Here we see the plots of the simulated GW emission spectra from supernova with core-collapse happening via the three different mechanisms: neutrino + SASI (top), magnetorotational (middle) and acoustic (bottom). GW spectra in the neutrino mechanism is of stochastic nature, with random polarisations. Only the  $h_+$  (equatorial) polarization is represented. In the magnetorotational mechanism, GW are linearly polarised because of axial symmetry, with a strong negative peak at the core bounce. The first part of the acoustic mechanism emission is similar to the neutrino one, since SASI processes dominate. About 0.3s after the bounce the PNS pulsations become dominant leading to a narrow-band signal at the quadrupole pulsations' frequencies. The different scales on the axis show the different timescales of the processes: the magnetorotational mechanism appears faster than the other two<sup>72</sup>.

### 3.6 Stochastic GW Signal

Stochastic gravitational waves, much like the cosmic microwave background (CMB) radiation originate from the early Universe. There could be, however, many sources of these primordial GW. These possible sources all superimpose onto one another to create a background radiation of GW which would be incident from all around. This source of GW would be highly red-shifted due to the expansion of the Universe, however there still would be information contained within the waves since they do not couple weakly to matter, meaning little information is dissipated due to interference. Some examples of the many mechanisms are discussed below.

### 3.6.1 Inflation

During inflation the Universe expanded rapidly over a very short time period. This caused some of the vacuum/quantum fluctuations in the early Universe to be amplified. This however would not create GW in the usual way through tensor perturbations in the metric. The fluctuations created by pure randomness propagate as GW after inflation has occurred and thus contribute to the background GW.

### 3.6.2 Preheating

After inflation, an excess of energy was present in the Universe from the scalar field which was driving inflation. This energy evolved towards thermal equilibrium, however the process itself would be very turbulent and non-linear which lead to stresses in space-time. The production of these types of GW would only occur if inflation took place at sufficiently low energies.

### 3.6.3 Cosmic Strings

Cosmic Strings are remnants of phase transitions at the end of inflation. When any of these strings cross each other, or themselves, they create smaller cosmic loops which oscillate relativistically. These loops lose energy and decay through the emission of GW. Due to the range in size of these strings and loops the background signal resulting from these interactions would have a large frequency range. Another mechanism by which the strings may lose energy is so called ‘cusps’ or ‘kinks’. These occurrences would produce bursts of GW.

### 3.6.4 First Order Phase Transitions

During the cooling down period of the Universe, several phase transitions occurred which were driven by the cooling process. These transitions created what is known as *phase bubbles*. They are areas of the Universe which exist in a different phase from one another. The collision of these bubbles would have created stresses, leading to the generation of GW. In the current formulation of the standard model the Electro-Weak Phase Transition (EWPT) is not expected to produce any measurable cosmological signals however other theories could predict first order EWPT which produce GW along with other phenomenon, such as baryogenesis and candidates for dark matter.

## 4 Detector technology

Despite the vast amount of theoretical work over the past several decades relating to GW physics, the science had been unconfirmed by experiment until 2015. The famous coincidence signal produced by the LIGO detectors (see Figure 1 at the top of this review) embodies the monumental achievement by experimentalists, engineers and theorists alike, and has been the culmination of decades of work in the field of GW detection. The detection itself will be discussed in further detail in section 4.4.

The act of detecting the waves is a key aspect of GW physics. It serves as another test of Einstein’s theory of general relativity, as well as a means of corroborating and confirming the claims of those who have been developing theories over the past 50 years relating to GW, cosmology and astrophysics. This section will address GW detection beginning with its reasonably humble conception, up to the advanced experiments of the future.

## 4.1 The Beginnings of Gravitational Wave Detection

The prediction of GW in Einstein’s theory of general relativity has brought about a further challenge to science teams across the globe: that of building the highly sophisticated machines, and detectors of unprecedented sensitivity, that can detect them. The earliest advancements in this field have widely been attributed to Joseph Weber who, whilst working at the University of Maryland, built two detectors comprised of aluminium alloy cylinders and separated them by around 2 km, claiming that they would resonate in coincidence as a GW passed through the Earth. The working principle behind Weber’s detector was based on the theorised interaction<sup>95</sup> of a GW with a ring of test particles, shown in Figure 7. Weber showed that a GW would distort and do work on a ring of test particles, and he described this as the GW driving an engine<sup>98</sup> the effect of which could be measured.

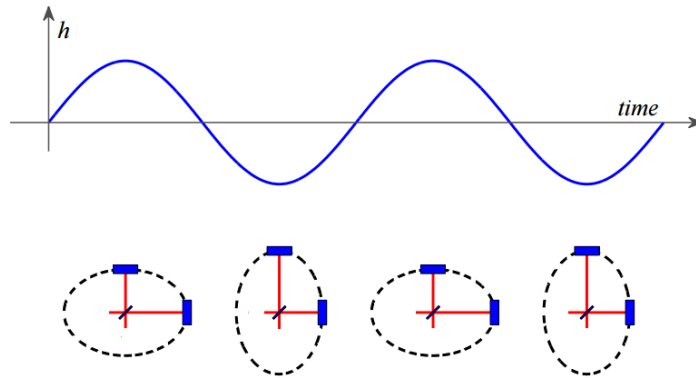


Figure 7: Distortion of a ring of test particles for two full cycles of a wave, showing the ring being distorted into an ellipse with its major axis in orthogonal directions for every half-wavelength<sup>8</sup>. Amplitude of the wave is characterised by the strain,  $h$ , defined by (54).

In practice, Weber’s detectors would have to be sensitive to changes in the length of the aluminium cylinders of the order of  $10^{-15}\text{m}$ , corresponding to a nuclear radius. The metal bars, however exhibit vibrations of this order of magnitude in the absence of a GW, as will be discussed in subsequent sections on noise sources. In an attempt to outrule coincident vibrations of the two cylinders that were not caused by GW, Weber employed the method of the *delay histogram*. This approach involved comparing the outputted events as a function of time for both of the detectors, and “shifting” the distribution for just one of them (one can imagine superimposing two graphs of events versus time with the axes aligned, then shifting one graph along the time axis and comparing the two distributions). With the two distributions out of alignment the number of coincident events can be counted, and the process repeated with different time shifts. With repeated applications one can build up a statistical picture of the background and can therefore make an estimation of the likelihood that a excess of coincidences is just a background fluctuation. This method of background estimation is still relevant to GW detection today<sup>22</sup>.

Weber’s detector, which was known as a *resonant mass detector*, and others which follow the same working principle are, in theory, sensitive to burst, continuous and stochastic signals. Resonant bar detectors are best suited to detecting the burst signals due to their relatively large amplitude, and since they will create short coincident vibrations of the bars. A GW detection is characterised by an excess of these coincident pulses above the background estimation, provided by the method of the delay histogram. Joseph Weber

published several papers throughout his career in which he claimed to have obtained evidence for the existence of GW<sup>96,97</sup>, however these claims were mostly disregarded by the GW community since they could not be reproduced successfully. Weber had, however, devised a method of GW detection that would continue to be employed beyond his lifetime.

## 4.2 Modern Resonant Mass Detectors

Whilst the claims of Joseph Weber have mainly been debunked, some groups continued to use resonant bars to detect GW into the 21<sup>st</sup> century. One such group is the Ricerca Onde Gravitazionali (ROG) Collaboration, who operate the EXPLORER detector at CERN and the NAUTILUS detector at the Frascati INFN Laboratories, Rome. We discuss modern resonant mass detectors, giving particular consideration to the NAUTILUS detector.

### 4.2.1 The NAUTILUS Detector

Both the EXPLORER and NAUTILUS detectors are *cryogenic* resonant bar detectors, meaning that they operate at ultra-low temperatures of around 100mK (see §4.2.2). The NAUTILUS detector<sup>21</sup>, shown in Figure 8, comprises most generally of an aluminium bar (2350kg) connected to a *resonant capacitive transducer* which is followed by an *ultra-low-noise amplifier* known as a SQUID (superconducting quantum-interface device). The vibrations in the bar (caused by a GW or otherwise) are converted into electrical signals by the capacitive transducer which are fed into the input of the SQUID amplifier. The amplified signals from the SQUID are then processed.

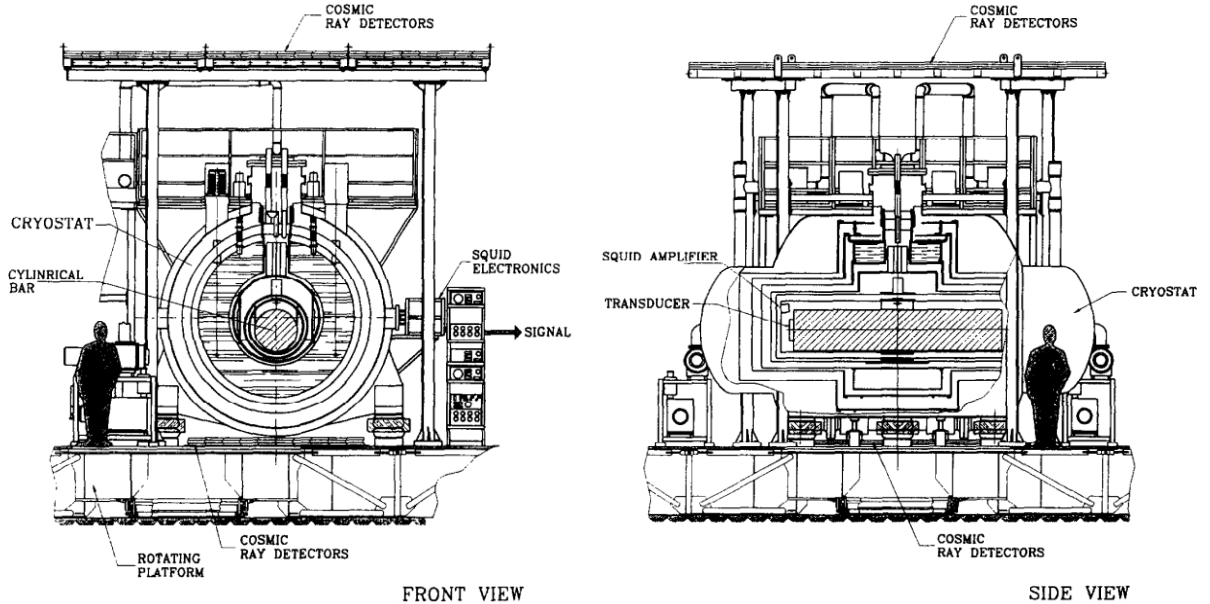


Figure 8: Layout of the NAUTILUS detector<sup>21</sup>.

In principle a bar detector has a single resonant frequency; the value of which can be positioned to be similar to the predicted frequency of incident GW bursts to achieve resonance when a wave passes through the detector. The NAUTILUS detector has two, however, at 908Hz and 924Hz, arising from the properties of the bar itself and its coupling to the resonant transducer.

A major challenge faced when designing the NAUTILUS detector, as is still the case in modern GW detection, was obtaining a clear and comprehensive signal. According to D. G. Blair<sup>29</sup>, who was involved in the development of the NIOBE resonant bar detector<sup>71</sup>, “...only a very small fraction of the signal energy is coupled into a detector”. This is due to what is commonly referred to as the *impedance-matching problem*, arising from the profound difference in the impedance of the resonant bar and that of the medium through which the GW propagates<sup>9</sup>. In more practical terms: if the strain amplitude,  $h$ , is defined as

$$h = \frac{\delta L}{L} \quad (54)$$

where  $L$  is the length of the bar, then a resonant bar of a few meters in length would need to be sensitive to a strain amplitude<sup>29</sup> of  $h \sim 10^{-18}$  to  $10^{-20}$ . A crucial element to obtaining a strong signal is to identify and minimise the main noise contributions to the system. These noise sources include thermal noise, mechanical vibrational noise from the detector’s surroundings, and electrical noise from the components of the detector.

#### 4.2.2 Thermal Noise and Q-Factor

Thermal noise arises from the thermal kinetic energy of the atoms in a resonant bar and may seem like, due to the constant presence of thermal fluctuations, an unavoidable complication. Furthermore one might expect  $k_B T$  to be a limiting point at which vibrations in the bar due to a GW are distinguishable from thermal vibrations (atoms vibrate with this energy in equilibrium at temperature  $T$ ).

To address the issue of thermal noise, materials with large  $Q$ -factors, have been used to minimise energy loss within the bar ( $Q$ -factor is defined as the reciprocal of the energy loss as a fraction of total energy, i.e. the extent to which the oscillator is underdamped). The NAUTILUS detector comprised of the aluminium alloy 5056, which has a  $Q$ -factor of order  $\sim 10^3$  greater than that of the pure aluminium bar used in previous experiments. A high  $Q$  material will have a particularly high *ring down* time,  $\tau$ , associated with the bar’s fundamental mode, which is the time taken for the vibrational amplitude to drop to a factor of  $e^{-1}$  of its original value. A high  $Q$  material, with a large  $\tau$  value, will develop thermal fluctuations of order  $k_B T$  on this time scale. A GW burst will occur on a relatively short time scale compared to  $\tau$  over which time the fluctuations in the energy due to thermal vibrations will be small. Therefore, if one makes a measurement over a short enough time scale,  $\tau_m$ , then the presence of a GW can be observed above the thermal noise, and at energy values below  $k_B T$ . The “effective” thermal noise energy is then of the order of

$$k_B T \frac{\tau_m}{\tau}. \quad (55)$$

The thermal noise is reduced by surrounding the NAUTILUS detector with highly sophisticated cryogenic apparatus. The setup consists of two aluminium shields which are cooled using helium gas, followed a liquid helium reservoir and a series of copper shields, which provide further successive cooling such that the bar itself is at a temperature of

---

<sup>9</sup>By drawing analogies with Einstein’s field equations,  $\mathbf{T} = (\frac{c^4}{8\pi G})\mathbf{G}$ , and the physics of acoustic waves one can identify an impedance, of the order  $10^{35} \text{ kg s}^{-1}$ , which characterises the medium in which GW propagate. On the other hand, the impedance of a typical resonant bar detector is equal the density of the material multiplied by the speed of sound, which is of the order  $10^8 \text{ kg s}^{-1}$ . When a wave passes through the resonant bar the impedance it ‘feels’ will only change by approximately  $x \rightarrow (1 + 1 \times 10^{-27})x$ . This fact means that a GW exchanges an incredibly small amount of energy with the detector, and modern experiments involve designing detectors with a high characteristic impedance to maximise energy transfer, making the wave easier to detect.



100 mK (see Figure 9). The bar is suspended on copper cables which provide a thermal path between the bar and the thermal contacts. The complete system of refrigerators and shields has also been designed to minimise the transmission of vibrations to the bar from the outside. The liquid helium is maintained in a superfluid regime, which eradicates any additional noise that would arise from boiling liquid helium. The result of the intensive cooling of the bar is a reduction of the thermal noise corresponding to  $\delta L \approx 10^{-16}$  m at room temperature to  $\delta L \approx 10^{-18}$  m at 100 mK, thus making it significantly easier to distinguish signals due to GW.

#### 4.2.3 Electronic Noise

Another source of noise which limits the sensitivity of resonant bar detectors is electronic noise. This is an intrinsic property of the electrical components used within the detector, such as the signal amplifier. The read-out system in the NAUTILUS detector (the transducer, amplifier and subsequent electronics) is designed to minimise electrical noise and maximise energy transfer from the bar to the read-out apparatus. The bar itself is coupled to the capacitive transducer, which form a system of two coupled oscillators<sup>84</sup>. The transducer in the NAUTILUS detector res-

onates at the same frequency as the bar, which provides good energy transfer between the bar and the readout electronics. The detector utilises a SQUID amplifier, which was chosen due to the extremely low, and unparalleled, intrinsic noise levels<sup>77</sup>.

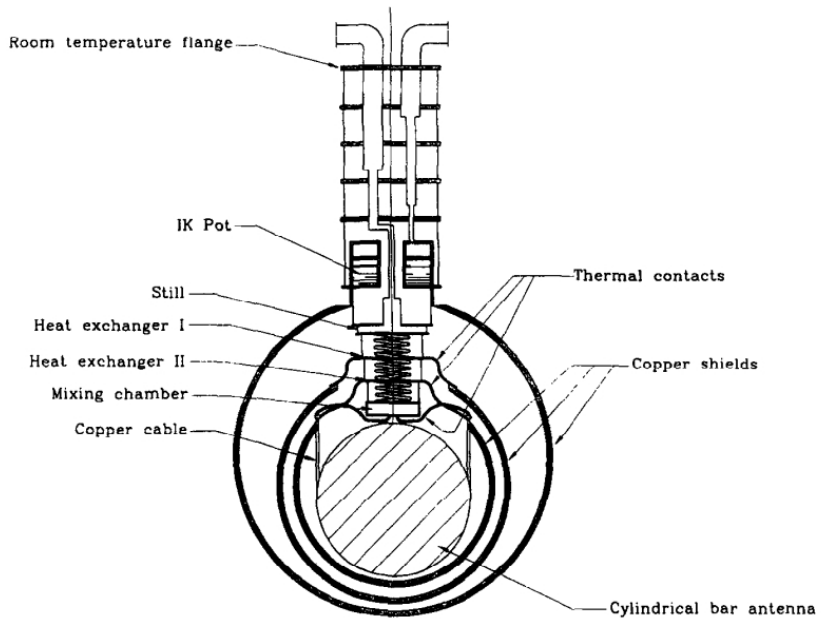


Figure 9: Schematic of the NAUTILUS cryogenic apparatus<sup>21</sup>.

#### 4.2.4 The Future of Resonant Mass Detectors

The current capabilities of resonant bar detectors do not quite match the those of the large-scale GW *interferometers* (see §4.3). The strain sensitivity of resonant bar detectors has peaked at a value of approximately  $h \sim 10^{-19}$  which is still around three orders of magnitude below the estimated sensitivity that is required for detecting GW. There are however some important factors to consider concerning the past performance, and future prospects, of resonant mass detectors. Over the past two decades there have been several resonant mass detectors in operation; the data from which have been pooled and compared. While there has not been the suggestion of the presence of GW to a high enough significance, upper limits have been established on the rate of GW bursts<sup>19</sup>. Other intriguing results have been obtained with data from the NAUTILUS and EXPLORER detectors such as a small excess of coincidences corresponding to when they were pointing in the direction of the rotational centre of the Milky Way<sup>20</sup>.

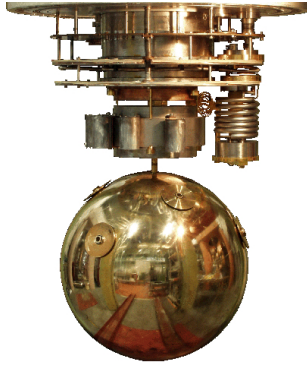


Figure 10: The MiniGRAIL sprical detector, which is aimed to operate at  $\sim 20$  mK and reach strain sensitivities of  $\sim 4 \times 10^{-21}$ <sup>55</sup>. Image source: *www.minigrail.nl*, retrieved 2016.

Developments have also been made in the past decade concerning spherical resonant mass detectors as an avenue for improving the sensitivity of resonant mass detectors. One such project is the MiniGRAIL resonant sphere, the first of its kind, shown in Figure 10. There are a number of stark improvements which spherical detectors offer. For the same resonance frequency, a spherical detector has a larger mass than a bar detector which means a GW will do more work on the detector, and the detector will have a larger cross-section for absorbing GW and a higher sensitivity. Additionally a spherical detector can detect GW from all directions and, as

G. Frossati writes<sup>48</sup>, they possess “...five degenerate quadrupole modes of vibration...” whereas “cylindrical Weber-bar detectors have only one useful quadrupole mode”, which means that spherical detectors allow one to deduce both the direction of arrival and the polarisation of GW. This is a property which is not shared by bar detectors or solitary interferometers (data from multiple ( $n > 3$ ) interferometers can be combined to deduce information about the direction of travel of the wave), and will likely be crucial for similar projects receiving funding in the future.

An extension to the spherical detector design is the hollow sphere detector<sup>37</sup>. Whilst sharing with the solid sphere design the benefits of detecting waves from all directions, the hollow sphere has a much smaller mass, meaning its resonant frequencies are nearer to  $\sim 200$ Hz. A hollow sphere detector of this design would then perhaps be able to compete with the large-scale laser interferometer designs since these two designs have overlapping frequency over which they are sensitive to GW. This is another promising avenue for improving the state of resonant mass detection and since detectors of this kind are generally far cheaper than their interferometer counterparts, it is likely that a perceivable increase in the number of resonant mass experiments will be seen in the next couple of decades, as their sensitivities continue to be improved.

### 4.3 Interferometry

Another method of GW detection, which has encompassed decades of collaboration and many millions of dollars of funding, is that of laser interferometry. This method dates back to the 1960s, and has been a competitor in ways (such as funding) to the resonant mass method. The basic principle of laser interferometry has its roots in the Michelson-type interferometer which was used in the famous Michelson-Morley experiment<sup>73</sup> (Figure 11). A laser source emits light with a spatial component described by

$$E_0 e^{-i\omega t + i\mathbf{k} \cdot \mathbf{r}}. \quad (56)$$

Where  $\mathbf{k}$  and  $\omega$  denote the wave-vector and angular frequency of the laser respectively and  $\mathbf{r}$  is the position vector of a photon in the laser beam. If the  $x$ -axis is defined as parallel to the horizontal arm in Figure 11 and the  $y$ -axis parallel to the vertical arm in Figure 11 then the light will travel a distance of  $L_x$  and  $L_y$  (i.e. the length of each arm) before arriving back at the beam-splitter. If the beam arrived at the beam-splitter initially at a time  $t_0$  then the time co-ordinates for the second arrival at the beam-splitter are



$$t = t_0^{(x)} + \frac{2L_x}{c} \quad \text{and} \quad t = t_0^{(y)} + \frac{2L_y}{c} \quad (57)$$

so that

$$t_0^{(x)} = t - \frac{2L_x}{c} \quad \text{and} \quad t_0^{(y)} = t - \frac{2L_y}{c}. \quad (58)$$

Setting the beam-splitter position to  $\mathbf{r} = \mathbf{0}$ , then the initial phases of the beams are

$$e^{-i\omega t + 2ikL_x} \quad \text{and} \quad e^{-i\omega t + 2ikL_y}. \quad (59)$$

Where the relation  $k = \frac{\omega}{c}$  has been used. The two light beams acquire a phase-factor of  $\pm \frac{1}{2}$  due to transmission and reflection at the beam-splitter and mirrors, such that when the two beams recombine they are described by

$$E_x = -\frac{1}{2}E_0 e^{-i\omega t + 2ikL_x} \quad \text{and} \quad E_y = +\frac{1}{2}E_0 e^{-i\omega t + 2ikL_y}. \quad (60)$$

Then, re-writing  $2L_x = (L_x + L_y) + (L_x - L_y)$  and  $2L_y = (L_x + L_y) - (L_x - L_y)$ , the resulting light beam is

$$E_{\text{out}} = E_x + E_y = -\frac{1}{2}E_0 \left\{ e^{-i\omega t + 2ikL_x} - e^{-i\omega t + 2ikL_y} \right\} \quad (61)$$

$$E_{\text{out}} = -\frac{1}{2}E_0 e^{-i\omega t + ik(L_x + L_y)} \left\{ e^{ik(L_x - L_y)} - e^{-ik(L_x - L_y)} \right\} \quad (62)$$

$$E_{\text{out}} = -iE_0 e^{-i\omega t + ik(L_x + L_y)} \sin(k[L_x - L_y]). \quad (63)$$

The photodetector is sensitive to the *intensity* of the light beam, i.e.

$$|E_{\text{out}}|^2 = E_0^2 \sin^2(k[L_x - L_y]). \quad (64)$$

Therefore we see that a non-uniform change in the length of the two arms will result in a change in the intensity measured by the photodetector. Since GW are theorised to have such an effect (see Figure 7) this forms the basis for GW interferometry. There are currently three major GW experiments which utilise laser interferometers: GEO 600<sup>103</sup>, located in Germany; Virgo<sup>13</sup>, located in Italy and LIGO<sup>25</sup>, comprising of the largest laser interferometers which are located in Louisiana and Washington State, USA. These machines have come to represent a monumental technological achievement, with cutting edge components which are continuously monitored and whose performance is constantly being improved. A description of a LIGO interferometer is given below.

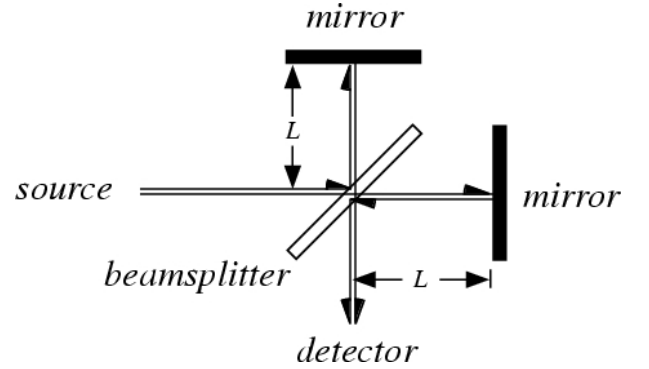


Figure 11: Michelson-Morely interferometer. Image source: [www.scienceworld.wolfram.com](http://www.scienceworld.wolfram.com), retrieved 2017.

### 4.3.1 LIGO Detectors

The LIGO experiment includes three laser interferometers: a single 4 km long interferometer located in Livingston, Louisiana, (L1) and two interferometers of 4 km and 2 km in length located in Hanford, Washington State (H1 and H2 respectively). The layout of a LIGO interferometer, as depicted in Figure 12, consists of a laser source which sends monochromatic light along an initial path to a beam-splitter, at which point the light is split into two orthogonal paths. The light travels along these orthogonal *storage arms* before being reflected highly reflective mirrors, referred to as the *test masses*. The light rays then recombine and the resulting light wave intensity is measured by a photodetector. In the absence of a GW the light will travel equal distances in the two arms of the detector. The influence of a GW however is to lengthen one arm and shorten the second, orthogonal, arm (see Figure 7) which will produce a path difference between the two orthogonal paths. This will change the form of the light when the two beams recombine, which can then be measured.

As with resonant mass detectors, every possible aspect of a laser interferometer must be optimised to reduce noise and create a measurable signal. The LIGO detectors house highly stable laser sources, sophisticated vacuum systems, complex suspension systems for the test masses (mirrors) and layers of vibrational isolation to suppress noise sources and create a strong signal in the presence of a GW. Some of these systems will be discussed in the following sections. Additionally, the *delay lines* have been used in previous

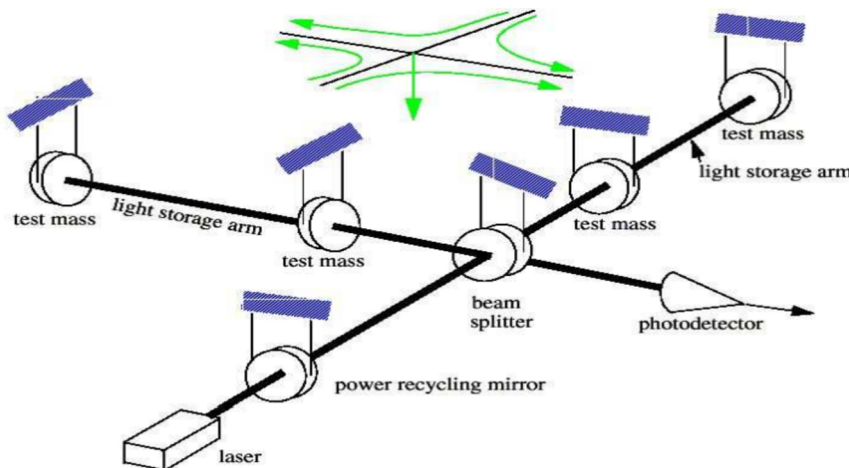


Figure 12: Layout of a LIGO detector showing main components, showing an incoming GW from above<sup>6</sup>.

designs to increase the measurable path difference  $\delta L$  which scales with the detector's arm length. The optimal arm length corresponds to the laser beams spending a time inside the detector arms which is equal to half the period of the GW. Delay lines utilise mirrors to bounce the light beams back and forth along trajectories which are not quite overlapping. This increases the distance travelled, and time spent in the storage arms, by the light beams essentially producing the effects of an  $\mathcal{O}(100\text{km})$  detector with one of only a few kilometers in length. To address the same issue, the LIGO detectors use *Fabry-Perot cavities*<sup>44</sup>, optical cavities made up of mirrors between which the light reflects many times. One of the mirrors partially transmits the light beam, and each of the transmitted beams are then focused with a lens. This significantly increases the sensitivity of the detector, whilst overcoming problems of large mirrors and noise associated with the use of delay lines. These will not be discussed in any further detail.

### 4.3.2 Suspension System and Seismic Noise

A significant source of noise in the detector is that of mechanical vibrations, and seismic noise which can be caused by things such as ocean waves, rivers and vehicle traffic from the surrounding area. To combat these, the LIGO detectors utilise complex methods of suspension to stabilise the mirrors, as well as a seismic isolation system comprising of multiple *passive* and *active* layers. The suspension system, the final stage of which is shown in Figure 13, works to minimise vibrations from the surrounding environment from transferring to the mirror. Platforms from which the mirrors are suspended serve this function as well as a series of counter weights. One of these counter weights is shown in the figure, with another three contained in preceding stages. These counter weights, along with the motion of the mirror, provide horizontal vibration isolation. Another measure taken to eliminate unwanted vibrations in the mirror is the use of magnets, attached to the mirror itself, which use “alternating polarities to reduce coupling to environmental magnetic fields”<sup>6</sup>.

The aforementioned methods constitute the *passive* seismic isolation measures, which are crucial in the discrimination between external vibrations and the strain in space introduced by a GW. Passive techniques are mechanical by nature and act to absorb vibrations which occur in the external world. A second type, *active* isolation techniques, involves using sensors and electronics to cancel out vibrations. Examples of these in the LIGO detectors are the use of actuators (device used to move a mechanical system) which are in line with the arm and can translate the mirror suspension and seismic isolation systems in response to earth tides. Embedded in the housing for the mirrors are auxilliary seismometers which again work to sense and respond to the surrounding seismic activity. Additionally, a system for reducing disturbances at the microseismic ( $\sim 0.16\text{Hz}$ ) frequency is employed<sup>52</sup>.

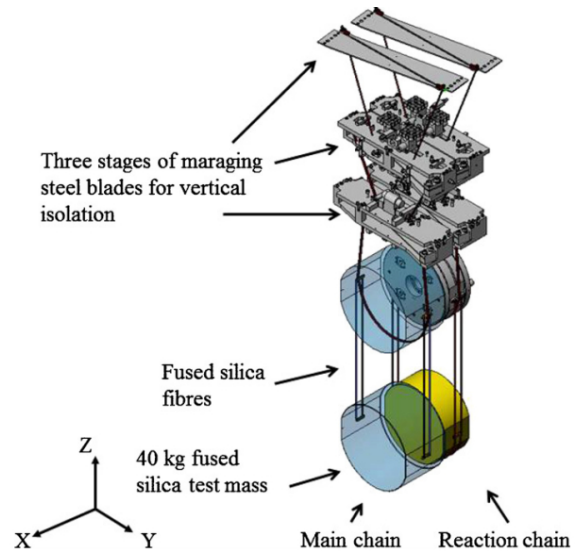


Figure 13: Section of the LIGO mirror suspension system<sup>18</sup>

### 4.3.3 Thermal Noise

Another challenge in GW interferometry is the reduction of thermal noise. Whilst resonant mass detectors are cryogenically cooled to reduce the influence of thermal vibrations, a different approach is taken with interferometers since cooling the apparatus has a lesser effect on the thermal noise. According to D. G. Blair, “a more elegant approach is to shift all [thermal] resonance frequencies out of the frequency window of observation”<sup>29</sup>. As with resonant mass detectors, the mirrors in the LIGO detectors are made from a material with a high  $Q$ -factor which concentrates the thermal motions into a small frequency range around the thermal resonances. In essence, the thermal vibrations peak at a frequency dissimilar to the predicted frequency of the GW, and in this way the two sources of vibration can be differentiated. As a result of these measures, in the first scientific run S1 (run in which data was taken for LIGO), a “...negligible level of off-resonance thermal noise...”<sup>6</sup> was reported.

#### 4.3.4 Shot Noise and Radiation Pressure

A noise source which interferometers do not share with resonant mass detectors is *shot noise*. This arises from the quantum nature of light, and the fact that the measurements made by the photodetector are so sensitive that they can be reduced to a photon-counting problem (since it measures minute changes in the intensity of the laser light). Fluctuations about the mean power of the laser source leads to an error  $\Delta N$  in the number of photons which reach the photodetector. This phenomenon is one of several which constitute the *standard quantum limit*, which represents the point at which noise is limited by quantum effects. This limit can be surpassed by the use of injecting *squeezed states* of light into the interferometer (see §5.1.1). Without using squeezed states, however, shot noise can in theory be reduced since the signal produced by a GW is proportional to the power of the laser, whilst the Poisson error governing the counting of the photons goes as the square-root of the power. Therefore by increasing the power of the laser one can reduce the shot noise.

By increasing the laser power to reduce the shot noise however the effect of another phenomenon, that of *radiation pressure*, becomes more prominent. This is also related to the fluctuations in the average laser power and arises from the fact that the change in momenta of the photons at the mirror will produce a force on the mirror. Fluctuating numbers of photons in each arm will lead to an uncertainty in the momenta of the two mirrors, which again incurs an error in the photodetector measurement. C. M. Caves<sup>34</sup> argues that this phenomenon is not caused by the fluctuating power of the laser source, since the effect of these fluctuations would be the same at both mirrors. Rather, it is an intrinsic property of a laser interferometer, and he identifies two sources for this: the first being the random nature of the beam splitter, and the second being vacuum fluctuations in the electro-magnetic field. This so called radiation pressure noise however does still scale with the power of the laser, and so there exists an upper limit on the laser power when both the shot noise and radiation pressure noise is considered<sup>2</sup>.

### 4.4 Detection of Gravitational Waves

In early 2016, a paper was published by the LIGO Scientific Collaboration and the VIRGO Collaboration which reported the first ever direct detection of gravitational waves. Two LIGO detectors, L1 in Livingston and H1 in Hanford, detected a coincident signal which “...matches the waveform predicted by general relativity for the inspiral and merger of a pair of black holes and the ringdown of the resulting single black hole”. The data corresponded to a significance greater than  $5.1\sigma$  and elucidated the “existence of binary stellar-mass black hole systems”. This discovery was a monumental breakthrough for all those working in the field of GW detection, and has eluded to the vast amount of information we can obtain in the future and the discoveries that are still to come. New projects such as a space-bound interferometer, LISA (see §5.2.1) are intended to push the boundaries of GW detection, and the expansion of the LIGO project to India with LIGO-India<sup>62</sup> will greatly improve the reconstruction capabilities of the current project and provide further information about GW sources.

A factor which has a large influence on future experiments, especially those requiring the design and construction of huge machines such as GW interferometers and particle colliders, is funding. After the Higgs boson was observed in 2012 one might have expected the acquisition of funding for CERN’s future developments to have become easier. This is not exactly the case however since, as was described by Dr. Ingrid-Maria Gregor of DESY, Hamburg, in 2016: there was the general sentiment of “what more do you want

now?” from the major funding donors. One would hope that this sentiment will not apply in the field of GW detection as it could be argued that there is stronger evidence for other sources of GW than there is for, say, additional Higgs bosons as in the supersymmetric standard model. With subsequent direct detections of GW<sup>1</sup> and development underway for projects such as LISA and MiniGRAIL, a vibrant future awaits for the field.

## 5 Detector Technology: The Next Generations

The first generation of GW detectors paved the way for future generations by proving their existence. However, once the first generation has reached its design sensitivity, without significant upgrades there is very little that can be done to improve the ability of these instruments to detect GW. Although only two positive detections of GW have occurred as of yet, the prospects of being able to use GW to see more of the universe are so bright that investing in improved detectors is essential. This section will outline the evolved ground based detectors that build on the detection from initial LIGO and look into space based detection which completely eliminates the effect of seismic noise, something that seriously limits detectors based on the ground.

### 5.1 The Future of Ground Based Detectors

Even though detectors based on the ground have significant limitations to their sensitivity caused by seismic vibrations, ground based detectors do have a future and are still being developed. The money saved by research facilities in not sending equipment into space can be used to develop technology to increase sensitivity and reduce noise. In fact, as will be outlined in this section, the most efficient method of GW detection will involve using ground based and spaced based detectors together. Hence, it is necessary to develop a second generation of ground based detectors that operate to a higher sensitivity.

#### 5.1.1 Advanced LIGO

The Advanced LIGO project improves on the sensitivity of initial LIGO by upgrading the existing equipment and making some additions. The sensitivity of each interferometer will be ten times higher than the interferometers in the initial LIGO project<sup>89</sup>. Much like the original LIGO project, Advanced LIGO will consist of three individual Michelson interferometers. The individual interferometers will consist of two perpendicular arms. For the Advanced LIGO project the arms will be 4km in length, a change from the initial LIGO project in which one of the detectors had only 2km arms. The strength of a GW signal grows with an increase in the arm length of the interferometers since the apparent change in arm length is larger if the arms are longer. Hence the increase in arm length at one of the interferometers will increase the strength of signals observed there<sup>101</sup>.

Most of the hardware used in the original LIGO project will be upgraded for Advanced LIGO with a focus on improving sensitivity and reducing noise. In this section we discuss in detail the hardware upgrades with a focus on those designed to reduce sources of noise.

**The Laser** The power of the laser used in the interferometers will be increased by a factor of 20 from 10W to almost 200W (<https://www.advancedligo.mit.edu/overview.html>). The upgraded laser that will be used for Advanced LIGO is to be provided by the GEO Collaboration, the same team that developed the laser for the GEO 600 and Virgo projects<sup>57</sup>. The upgraded laser aims to reduce the effect of shot noise. As mentioned in



Section 4, shot noise is a statistical source of noise arising from fluctuations in the amount of light hitting the detector so, increasing the power of the laser and hence the amount of light that enters the interferometer will reduce the its effect.

Advanced LIGO also has a finesse that is much improved from that of LIGO. Finesse is a quality of the arm cavities that gives a measure of the ability of the interferometer to resolve spectral features that are close together. The combination of the higher laser power and the improved finesse means that the arm cavities of Advanced LIGO will have a circulating power of 800kw a vast improvement on the 10kw power circulating in the arm cavity of the existing LIGO project<sup>89</sup>.

**Seismic Isolation** The seismic isolation system of Advanced LIGO completely replaces that of the initial LIGO setup. The motion of the ground due to seismic vibrations and other random disturbances is mostly noticed at frequencies lower than 10Hz. Therefore to detect low frequency GW signals, it is essential that seismic noise is reduced. Active inertial control is used to eliminate seismic noise at very low frequencies.

Outside of the vacuum chambers which contain the light cavities, hydraulic actuators exert a force on the tubes that hold the seismic isolation system. The force allows the motion of the hydraulic actuators to be transmitted into the vacuum chambers. Sensors and seismometers monitor the movement of the ground and relay the information back to the actuators so that they can adjust the movement of the vacuum chambers to eliminate the effect of ground movement.

Inside the vacuum, the seismic isolation system consists of two platforms suspended from each other by magnetic springs. Each platform will have six seismometers and six position sensors to measure the movement of the platforms in all six translational degrees of freedom. This information is fed back to a magnetic actuator which adjusts the movement of the platforms in order to cancel the movement caused by the seismic noise.

The combined seismic isolation will reduce seismic noise by a factor of 1000 in the 1-10Hz frequency range<sup>57</sup> and will help to eliminate the seismic noise at all observing frequencies.

**Signal Recycling** In addition to the upgraded hardware, Advanced LIGO will include a signal recycling cavity to work alongside the power recycling cavity of initial LIGO. The mirror will be added to the ‘dark’ output of the interferometer - the arm in which the reflected light is in anti-phase. The signal recycling cavities are designed to be stable in the Advanced LIGO setup. Having stable recycling cavities reduces the sensitivity of the cavity to optical distortions (<https://dcc.ligo.org/public/0002/T080208/001/T080208-00.pdf>). The addition of the signal recycling cavities allow the sidebands to be returned to the interferometer to be enhanced and correlated to extract more information<sup>17</sup>. The presence of the signal recycling cavities allow the quantum noise to be tuned and hence, as a result, some frequencies can be enhanced and others diminished.<sup>57</sup>

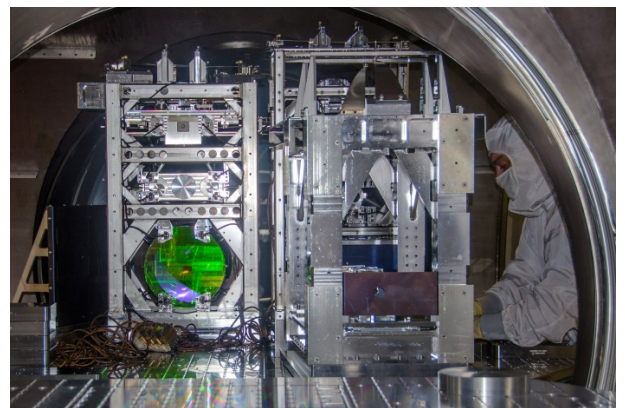


Figure 14: An image of the signal recycling mirror (bottom left) used in Advanced LIGO. Image:LIGO laboratory

**Sources of Noise and Squeezed States** The hardware improvements and additions made to the original LIGO setup result in the dominating source of noise over all frequencies being quantum noise. So the question arises: how can quantum noise be minimised?

In an experiment conducted in late 2011, squeezed states of light were injected into the LIGO interferometer located at Hanford. Light is formed by two electromagnetic field amplitude oscillations operating out of phase with each other by 90 degrees. These states can be labelled ‘in phase’ and ‘quadrature phase’<sup>10</sup> and the squeezed state corresponds to reducing the uncertainty of the quadrature phase relative to the coherent state in which both phases have equal uncertainty. The use of squeeze states in an interferometer reduces the shot noise below the quantum limit. The experiment conducted by introducing squeezed states of light into just one of the interferometers of initial LIGO reduced the shot noise by a 28%: a significant reduction. (<http://www.nature.com/nphoton/journal/v7/n8/pdf/nphoton.2013.177.pdf>).

The initial LIGO project used heterodyne detection which is not compatible with squeeze states. Heterodyne detection is the process of mixing a laser signal with one of a different frequency to produce a beat note that will be at the frequency difference. Advanced LIGO, however, uses homodyne detection, where the laser signal is mixed with one of the same frequency, and as a result will be compatible with the use of squeezed states in the future. Since shot noise is a statistical effect, it is often responsible for the sensitivity limit of a detector. The fact that Advanced LIGO can use squeezed states in the future and reduce the shot noise may further improve the capabilities of the detector once it has achieved its current sensitivity limit.

### 5.1.2 Other Ground Based Second Generation Detectors

Like LIGO, the Virgo and GEO600 projects have improved their sensitivity via second generation upgrades, namely Advanced Virgo and GEO-HF.

Advanced Virgo will have increased sensitivity by a factor of 10 from that of the initial Virgo project which will result the detection rate increasing by a factor of 1000<sup>12</sup>. Much like LIGO, the initial Virgo detector upgrades include increased laser power, the addition of a signal recycling cavity and new vibration isolation systems.

Although the initial GEO-600 project has a shorter cavity arm length than both the LIGO and Virgo projects, environmental limitations mean that the arm length of the GEO-600 detector could not be extended for the second generation GEO-HF project. The project will not come close to the sensitivity of the long arm Advanced LIGO and Advanced Virgo projects however the advantage of GEO-HF lies in the fact that it can run during the down-time of Advanced LIGO and Advanced Virgo<sup>102</sup>.

### 5.1.3 Third Generation Onwards

Generally, the second generation GW detectors improve the sensitivity of the initial detectors by a factor of 10. However, for precise astronomical study of the GW sources this is insufficient and the signal-to-noise ratio (defined in §6.2.1) needs to be much higher to detect such events. Hence a new generation of detectors is required. The Einstein Telescope will operate with a sensitivity 10 times greater than that of the advanced gen-

---

<sup>10</sup>By using the double angle formula  $\sin(A + B) = \sin A \cos B + \cos A \sin B$  and inserting it into the general equation of a wave,  $x(t) = A \sin \omega t + \phi$ , then any wave can be expressed as a sum of sines and cosines as follows:  $x(t) = A_1 \cos \omega t + A_2 \sin \omega t$ . The sine component is labelled ‘in-phase’ whilst the cosine part is the ‘quadrature phase’ component ([https://www.dsprelated.com/freebooks/mdft/In\\_Phase\\_Quadrature\\_Sinusoidal.html](https://www.dsprelated.com/freebooks/mdft/In_Phase_Quadrature_Sinusoidal.html)).

eration detectors mentioned previously making it ideal to study the gravitational wave signals emitted by bodies of smaller mass<sup>83</sup>.

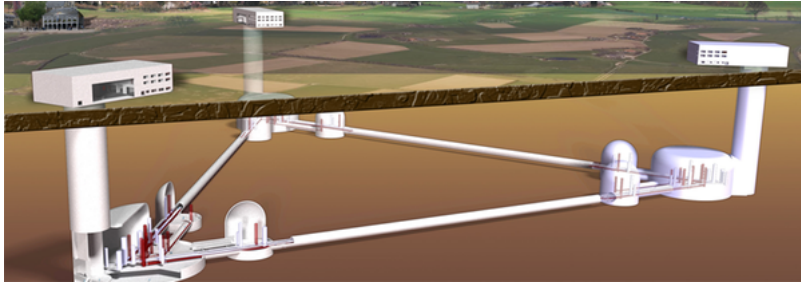


Figure 15: Computer model of the Einstein Telescope equipment (Image: Albert Einstein Institute Hannover).

The Einstein Telescope aims to increase the signal-to-noise ratio by operating underground with cryogenically cooled mirrors<sup>101</sup>. Figure 15 shows the logistics of the underground Einstein Telescope

#### 5.1.4 Conclusion

Advanced generation ground based GW detectors have a high enough sensitivity to continue to be used as high frequency detectors. Since some detectors are tailored to eliminating a particular source of noise (for example the Einstein Telescope focuses on eliminating thermal noise sources with cryogenically cooled mirrors), combining signals from detectors aimed at eliminating different sources of noise could perhaps mean that fewer signals have to be discredited due to noise. In conclusion ground based detectors will advance to give a comprehensive view of high frequency GW passing through Earth.

## 5.2 Space Based Detectors

Despite ground based detectors being effective in achieving the first positive GW detection, regardless of how sensitive they may become in the future a ground based detector will never be able to fully overcome the limits of seismic vibrations and mass movement. These effects limit the ground based detectors in such a way that GW that oscillate in the low frequency range of the spectrum cannot be detected from the ground. The low frequency range includes a diverse range of high mass sources, so being able to detect this range will allow for heavy objects such as black holes with masses up to  $10^8 M_{\odot}$  to be observed. To detect such GW one has to look to space.

### 5.2.1 LISA

The Laser Interferometer Space Antenna (LISA) will be the world's first space-based GW detector. Although the mission is now expected to be at a Technology Readiness Level of 6<sup>11</sup> by 2020 ([https://www.elisascience.org/files/publications/LISA\\_L3\\_20170120.pdf](https://www.elisascience.org/files/publications/LISA_L3_20170120.pdf)), the project development has not been without its adversities. The project was dropped completely in 2011 due to funding limitations. In 2013 the ESA called for GW project proposals and on 13<sup>th</sup> January 2017, the LISA project was proposed.

<sup>11</sup>Technology Readiness Level or TRL is a number from 1 to 9 assigned to a developing technology that assesses its maturity. A TRL 6 implies that the technology is at a stage in which there is a fully functioning prototype ([https://www.nasa.gov/directorates/heo/scan/engineering/technology/txt\\_accordion1.html](https://www.nasa.gov/directorates/heo/scan/engineering/technology/txt_accordion1.html)).



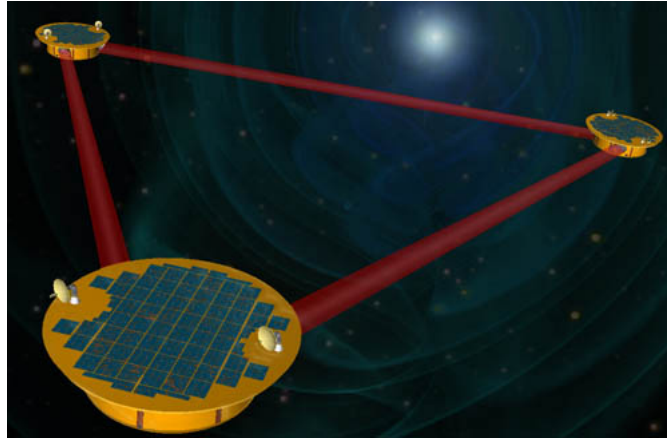


Figure 16: Computer simulated image of the Laser Interferometer Space Antenna (Image: Lisa Project Office at NASA).

Designed by the ESA and NASA, LISA will be formed of three spacecraft arranged in an equilateral triangle. The sides of the triangle form the arms with any two arms being used together as an interferometer. The interferometers will travel in an orbit, similar to that of the Earth, around the Sun. Each interferometer will have arm length of 5 million km - a length which is clearly unattainable on Earth<sup>88</sup>. Longer arms means the effect of low frequency GW is amplified, allowing LISA to detect the elusive but highly populated frequency range of GW below 1Hz<sup>88</sup>. This frequency range will allow it to detect BBH systems and objects falling into super massive black holes, with known binary systems being used for verification<sup>88</sup>. LISA will be used in conjunction with the second generation ground based detectors to provide a system of GW detectors that will capture a larger range of frequencies and hence a wider scope of sources than ever before.

**Methods** Each spacecraft will be centered on two free falling test masses, with each mass acting as an end mirror for one arm of the interferometer. The test masses used in LISA are known as ‘proof’ masses. They will be 4kg masses of gold-platinum alloy. Actuating thrusters located on the spacecraft will maintain the distance between the craft and the proof mass creating drag-free control<sup>60</sup>. Based on local interferometric readouts, the actuating thrusters force the spacecraft to move such that the distance between the masses and the spacecraft is constant. Since they are not in contact with the surface of the Earth, the free falling masses are no longer subject to seismic vibrations and so the interferometers can operate to a higher sensitivity.

There will be two active laser systems on each spacecraft. Three measurements will be required to accurately find the separation of the test masses and hence the change in the arm length due to the presence of gravitational waves. Two measurements will be of the test mass position within the spacecraft, on the optical bench<sup>12</sup>. One will measure the distance between the optical benches, along the arm length between spacecraft. The measurement of the distance between the spacecraft will be done using heterodyne interferometry<sup>88</sup>.

To verify unification of the lasers sent along the arms of the interferometer, one of the lasers sent from the main craft will be set as a master. When the master laser arrives at the neighbouring space crafts, the lasers to be emitted from them will be set to have the same phase as the master laser.

<sup>12</sup>An optical bench is a long rigid beam with a linear scale applied, optics will be held to the optical bench to form the desired formation of the image ([http://physics.kenyon.edu/EarlyApparatus/Optics/Optical\\_Bench/Optical\\_Bench.html](http://physics.kenyon.edu/EarlyApparatus/Optics/Optical_Bench/Optical_Bench.html)).

**Limitations** It is expected that for a well designed, properly functioning laser interferometer, the limiting source of noise will be from shot noise. To achieve this expected, inevitable limit to the sensitivity of a detector, all other sources of noise must be effectively eliminated.

The LISA equipment will be vulnerable to any gravitational fluctuations, including those not caused by GW. Fluctuations may cause the spacecraft to move relative to each other, obscuring the measurements.

The beat note is the characteristic signal of the GW and is produced by mixing the outgoing laser signal from the interferometer with a laser of a different fixed frequency. The measurement of the beat note is taken relative to an on-board clock on the spacecraft. Hence, any fluctuations of the clock will be indistinguishably mixed with the beat noise fluctuations carrying the information about the GW. The clock fluctuations can be eliminated in the data analysis stage.

Confusion noise is an effect of the high amount of GW signals present at frequencies below 0.1Hz<sup>64</sup>. A high amount of overlapping signals would lead to individual readouts becoming ‘confused’. The frequency range observable by LISA will mean that confusion noise becomes a relevant. However, it is claimed that the detections can be ‘untangled’ in the data analysis stages.

### 5.2.2 Other Space Based detectors

The Japanese based DECi-Hertz Interferometer Gravitational Wave Observatory (DECIGO) will be tailored to detecting GW in the 0.1-10Hz frequency range. The small frequency range is beneficial to designing a detector with a very high sensitivity since it is above the region in which confusion noise is relevant<sup>64</sup>. The frequency range of DECIGO lies between that of LISA and the ground based detectors. So, with all these detectors working together, an extremely large range of GW frequencies will be able to be observed.

DECIGO will consist of four clusters in heliocentric orbits consisting of three spacecraft carrying free falling mirrors arranged in triangular formations to form three Fabry-Perot Michelson interferometers. The arm length will be 1000km, since the Fabry-Perot design means the arm length can be shorter without concern about the divergence of the laser light. Fabry-Perot interferometers will also benefit by having reduced shot noise<sup>64</sup>.

The Big Bang Observer (BBO) will operate in the same frequency range as DECIGO. It will also be formed of a fleet of triangular laser interferometers which will have the same configuration as LIGO. Any one of the BBO detectors will be a hundred times smaller than LIGO and will have much improved sensitivity<sup>39</sup>. The extremely sensitive BBO is specially designed to observe the stochastic GW background and give insight into the state of the universe moments after the big bang.

The Advanced Laser Interferometer Antenna (ALIA) will be focused towards detecting intermediate mass black holes. It will have a similar construction to LISA but with smaller arm lengths and reduced noise<sup>41</sup>. ALIA will target the same frequency range as DECIGO and BBO and, like LISA, will be able to determine the position of sources of GW<sup>41</sup>.

### 5.2.3 Conclusion

The addition of space based detectors makes available a part of the GW spectrum never detectable before. The low frequency range allows scientists to ‘hear’ new parts of the universe and see closer to the Big Bang than was previously imaginable. In order to broaden our understanding of the Universe there is no doubt that space based GW detectors are crucial and it is likely that, with the funding available, low frequency GW will be observable by 2030.

## 6 Data analysis

In this section, the methodology of matched filtering to extract a useful signal in the presence of stationary, Gaussian noise will be described with application to GW detection with ground-based laser interferometers. The techniques described are very general and apply to space-based interferometers as well as other types of detectors described in §4. Several complex, multi-stage pipelines have been developed for the purpose of finding compact binary coalescence (CBC) events<sup>15,94</sup>, as well as burst events that may be a result of supernova explosions<sup>68</sup>, and they all rely on the technique of matched filtering to learn about the parameters of the source from which the GW was emitted.

### 6.1 Fourier methods

The data from an interferometer such as LIGO (L1, L2, H1) is a time series of strain data  $h(t)$  sampled at a rate of  $f_s = 16384$  Hz, where  $h(t) = \delta L(t)/L = (\delta L_x(t) - \delta L_y(t))/L$ , i.e. the fractional change in the length of the arms of the interferometer (see §4.3 for more detail). Including all sources of noise, the strain data can be written as  $s(t) = h(t) + n(t)$ , where  $h(t)$  is the GW signal and  $n(t)$  is the noise. As will be shown in §6.5, there are sources of noise that have well-known frequencies, for example the resonance frequency of the mirror pendulum and its harmonics, giving motivation for working with functions in the frequency domain. Moreover, the orbital energy, required in the derivation of a gravitational waveform, is expressed as a function of frequency  $F$ , and the Post-Newtonian (PN)<sup>30</sup> expression for  $F(t)$  is not a monotonic function, unlike that of the inverse,  $t(F)$ <sup>45</sup>. In the stationary phase approximation, templates (see §6.2.2) can be expressed directly as functions of frequency<sup>15</sup>.

Given a time series  $s(t)$  with  $N$  data points, its discrete Fourier transform (DFT) is defined as

$$\tilde{s}_n(f) = \sum_{k=0}^{N-1} s_n(t) e^{2\pi i k n / N}. \quad (65)$$

This is a list of  $N$  values separated in frequency by intervals of  $f_{fund} = 1/T$  where  $T$  is the length, in time, of the data block being analysed, and ranging from  $-f_c$  to  $f_c$ , where  $f_c = f_s/2$  is the Nyquist frequency. The data is conveniently sampled at frequencies that are a power of 2, and analysed in blocks of  $s(t)$  values that are a power of two. The Fast Fourier Transform (FFT) is employed, as it has a computational complexity of  $\mathcal{O}(N \log_2 N)$ , making the spectral analysis methods to be outlined feasible<sup>80</sup>.

The one-sided power spectral density (PSD)  $S_n(f)$  of a signal  $n(t)$ , also referred to as the power spectrum, is defined<sup>76</sup> as

$$\langle \tilde{n}(f) \tilde{n}^*(f') \rangle = \frac{1}{2} \delta(f - f') S_n(f). \quad (66)$$

With the discrete case being an average of the squared amplitudes of the Fourier coefficients of the function in frequency bins of a chosen size. For a real signal  $n(t)$ , this definition has the property  $S_n(-f) = S_n(f)$ . The amplitude spectral density (ASD) is then defined as the square root of the PSD and has units of strain/ $\sqrt{\text{Hz}}$ . This is a key quantity in describing detector sensitivity, and is used in whitening the noise.

The discrete sampling introduces the problem of aliasing<sup>82</sup>, where the power for any frequency component outside the range  $-f_c < 0 < f_c$  is transferred into the range, making only values up to  $f \simeq 0.7 f_{rmc}$  trustworthy.

This is not an issue, however, for a signal limited in bandwidth to less than the Nyquist frequency, as its information content is then fully specified by all frequencies in the

previously mentioned range. Such is the case for current ground-based detectors, which are sensitive to frequencies of the order 10 – 1000 Hz, with the chirp from GW150914<sup>7</sup> being band-pass filtered to the range of frequencies 35 Hz – 350 Hz and the peak frequency of the GW signal for this specific event being 250 Hz.

## 6.2 The matched filter

When the exact shape of the signal can be modelled as in the case of compact binary coalescences, and the statistical properties of the noise are known, it is possible to construct an optimal detection statistic, the *matched filter*<sup>40</sup>.

From here on, the noise will be assumed to be stationary and Gaussian. Stationary noise is defined by its statistical properties not changing in time. Gaussianity of the noise is a reasonable assumption for the majority of data collection time, however, other types of noise must be accounted for in the data analysis to reduce false trigger rates. The assumption of stationarity will hold if the data is analysed in small stretches since over a short time period the properties of the noise are expected to remain constant. The LIGO team, in the data analysis for BNS coalescence events during the first scientific run (S1)<sup>5</sup>, used a  $\chi^2$  discriminator<sup>14</sup> to reject non-Gaussian noise transients.

Defining a noise-weighted (see Appendix B) inner product  $(a, b)$  of time series  $a(t)$  and  $b(t)$  as

$$(a, b) = 4 \operatorname{Re} \int_0^\infty \frac{\tilde{a}(f)\tilde{b}^*(f)}{S_x(f)} df, \quad (67)$$

where the PSD  $S_x(f)$  is for a specific time series  $x(t)$ . The quantity  $(s, h)$  is then the matched filter up to a constant (see Appendix C for the derivation). The matched filter is a noise-weighted correlation of the expected signal with the data.

In general, the expected signal will depend on some vector of  $N$  parameters,  $\boldsymbol{\lambda}$ , so it is written as  $h(t; \boldsymbol{\lambda})$ . To find the optimal detection statistic, one must marginalise over the unknown parameters,

$$\Lambda(H_1|s) = \frac{\int p(s|H_{\boldsymbol{\lambda}})p(H_{\boldsymbol{\lambda}})d\boldsymbol{\lambda}}{p(s|H_0)} = \int \Lambda(H_{\boldsymbol{\lambda}}|s)p(H_{\boldsymbol{\lambda}})d\boldsymbol{\lambda}. \quad (68)$$

Where  $\Lambda(H_{\boldsymbol{\lambda}}|s) = p(s|H_{\boldsymbol{\lambda}})/p(s|H_0)$  is the likelihood ratio for a specific signal in the parameter space, and  $p(H_{\boldsymbol{\lambda}})$  is a prior PDF describing which parameters are more likely. A good approximation, given a strong GW signal present with parameters  $\boldsymbol{\lambda}_{\text{true}}$ , is to use the maximum of  $\Lambda(H_{\boldsymbol{\lambda}}|s)$  as the optimum detection statistic, also referred to as maximum likelihood statistic, with the parameter values  $\boldsymbol{\lambda}_{\text{max}}$ .

### 6.2.1 Extrinsic Parameters of the Search

Extrinsic parameters are those for which it is possible to algebraically maximise signal-to-noise ratio (defined below).

**Amplitude** For a signal with a known form and an unknown amplitude,  $h(t; A) = Ag(t)$ , where  $g(t)$  is the template, the maximum likelihood statistic is

$$\ln \Lambda(H_{\text{Amax}}|s) = \frac{(s, g)^2}{2(g, g)}. \quad (69)$$

The quantity  $x = (s, g)$  is also referred to as the matched filter and can be shown to have the following properties:

1) When no GW signal is present in the strain data,  $x$  is a Gaussian random variable with  $\mu = 0$  and  $\sigma^2 = (g, g)$ .

2) When a GW signal is present,  $x$  is a Gaussian random variable with  $\mu = A\sigma^2$  and  $\sigma^2 = (g, g)$ .

It is now possible to characterise the strength of the signal through the signal-to-noise ratio. The signal-to-noise ratio (SNR) is a normalised matched filter

$$\rho = \frac{x}{\sigma} = \frac{(s, g)}{(g, g)^{1/2}}. \quad (70)$$

It has unit variance and, when a signal is present, a mean of  $q = \langle \rho \rangle = A\sigma = (h, h)^{1/2}$ , with  $q$  referred to as the characteristic signal-to-noise ratio. In LIGO's 6th scientific run, the minimum required SNR for a candidate binary coalescence event was taken to be 5.5 in each of the two operational detectors<sup>3</sup>, while the GW150914 detection had a (re-weighted) SNR of  $\hat{\rho}_c = 23.6$ <sup>7</sup>. This is a quadrature sum for two detectors defined in eqn. 77.

**Arrival time** The SNR can be expressed in this case as a function of the unknown arrival time  $t$ :  $\rho(t) = x(t)/\sigma$  where

$$x(t) = 2 \int_{-\infty}^{\infty} \frac{\tilde{s}(f)\tilde{g}^*(f)}{S_n(|f|)} e^{2\pi i f t} df. \quad (71)$$

This is simply the inverse Fourier transform of the matched filter. The maximum likelihood detection statistic is then the greatest value of  $\rho$  in a time period of interest.

**Coalescence phase** This is defined to be the orbital phase at the termination of the waveform (for PN approximations this is when the orbital frequency becomes infinite). The optimal detection statistic to search over the phase can be formed from the sum in quadrature of the matched filters for two orthogonal terms of the form  $h(t) = p(t) \cos \theta + q(t) \sin \theta$ . This gives the complex matched filter

$$z(t) = x(t) + iy(t) = 4 \int_0^{\infty} \frac{\tilde{s}(f)\tilde{h}^*(f)}{S_n(f)} e^{2\pi i f t} df. \quad (72)$$

Where  $x(t), y(t)$  are the time-dependent matched filter outputs for the two orthogonal waveforms, and the stationary phase approximation allows one to write  $\tilde{p}(f) = -i\tilde{q}(f)$ <sup>5</sup>.

To first order in PN, for two non-spinning binaries, the only two parameters left to search over are the individual masses of the objects. These are called intrinsic parameters, and a template bank is necessary to search over them.

### 6.2.2 Template Banks

Parameters for which it is impossible to algebraically minimise the SNR are referred to as intrinsic parameters. BNS inspiral waveforms are only strongly determined by the orbital inclination of the binary and the masses, with the individual spins coming in at higher orders of PN, where the contributions from other variables can be shown to be negligible<sup>42</sup>.

When it is not possible to find a continuous likelihood function over the parameter space, a set of templates  $\{u(t; \boldsymbol{\lambda})\}$  must be constructed, with each template normalised such that  $(u(\boldsymbol{\lambda}), u(\boldsymbol{\lambda})) = 1$  and  $\rho = (s, u(\boldsymbol{\lambda}))$ . The maximum likelihood detection statistic in this case is  $\max_{\boldsymbol{\lambda}}[\rho(\boldsymbol{\lambda})]$ . The loss of information due to the discrete nature of the parameter



space is defined as such: one imagines the signal as having parameters  $\lambda$ ,  $h(t) = qu(t; \lambda)$ . The nearest template in the bank has parameters that differ by  $\Delta\lambda$ ,  $u(t; \lambda + \Delta\lambda)$ . The SNR expectation for this template will be  $q' = (h, u(\lambda + \Delta\lambda)) = q(u(\lambda), u(\lambda + \Delta\lambda))$ . The fractional loss in the expected SNR due to the gridding is  $(q - q')/q = 1 - (u(\lambda), u(\lambda + \Delta\lambda)) = 1 - A$ , where  $A$  is called the ambiguity function. For small  $\Delta\lambda$ , Taylor expanding the second term of the inner product gives

$$A = 1 + \frac{1}{2} \Delta\lambda_i \Delta\lambda_j \left( u(\lambda), \frac{\partial^2 u}{\partial \lambda_i \partial \lambda_j}(\lambda) \right) + O((\Delta\lambda)^3). \quad (73)$$

The linear term is 0 as the expansion is around the maximum of  $A$ . The maximum allowed fractional loss in the expected SNR therefore sets the maximum possible distances  $\{\Delta\lambda_i\}$  between the parameters in parameter space through  $A$ . This is implemented computationally by defining a metric over the parameter space<sup>23</sup>.

### 6.2.3 Stellar-mass CBC Waveform Templates

The previously mentioned post-Newtonian (PN) approximation has already been extended to at least to 4PN order<sup>47</sup>, the 4 denoting an expansion to the order  $(v/c)^8$ . Such waveforms can model to high accuracy the inspiral phase of a CBC where the combined mass of the system  $M \lesssim 12M_\odot$ <sup>63</sup>, and will only break down close to the last stable orbit (LSO). These systems tend to go through enough cycles at the frequency range of ground-based interferometers to make it feasible to search for them using PN templates only.

However, it is expected that detectable events of this type will be less than those resulting from an inspiral of a more massive black hole binary<sup>4</sup>, and they are less "loud". In the nearly symmetric case (where the masses of the stellar black hole binary are comparable), only the last  $\simeq 10$  orbits of such a system are expected to be the signal that falls into the range of detectability of a ground-based interferometer (GW150914 completed only 8 orbital cycles rising in frequency from 35Hz to 150Hz). Producing a waveform for this, as well as the merger and ringdown phases, requires solving equations of general relativity numerically. This has not been possible until very recently<sup>35</sup>, and it is still far from computationally feasible to produce them at numbers of the order of magnitude that is necessary for a detection (approximately 250000 combined for GW150914), especially for high spins and high mass ratios.

It was known for a while that the PN converges badly and a better approach would be needed to create reliable templates<sup>31,53</sup>. The effective one-body (EOB) approach recasts the equations of motion into those for a single body moving in a deformed space-time, which allows the high mass-ratio regime to be covered more accurately, whilst including high spin binaries. The key to generating enough templates to cover the full process of inspiral-merger-ringdown requires two steps. First, higher order (pseudo) PN terms are estimated by minimizing the discrepancy between the PN inspiral waveforms re-summed in EOB and extended to arbitrarily higher orders<sup>63</sup>, and those obtained from NR simulations. This is then used to interpolate in the spin and mass ratio parameter space, where the range of interpolation is limited only by the availability of NR simulations that probe greater mass ratios and larger spins. This is referred to as the *effective one-body numerical relativity* (EOBNR) approach. Such waveforms model the full inspiral-merger-ringdown process and allow for access to a wide parameter space.

## 6.3 Multiple interferometers

### 6.3.1 Optimal two-detector statistic

Since the expected signal for two co-located, co-aligned detectors is the same, but the noise is different and uncorrelated, the matched filter is

$$(s_1, h)_1 + (s_2, h)_2 = (s_{1+2}, h)_{1+2} = 4\text{Re} \int_0^\infty \frac{\tilde{s}_{1+2}(f)\tilde{h}^*(f)}{S_{1+2}(f)} df, \quad (74)$$

with the subscripts for the inner products denoting weighting with respect to the noise of the  $i^{\text{th}}$  detector and

$$\tilde{s}_{1+2}(f) = \frac{\tilde{s}_1(f)/S_1(f) + \tilde{s}_2(f)/S_2(f)}{1/S_1(f) + 1/S_2(f)}, \quad (75)$$

where  $s_{1+2}(t)$  is referred to as the *coherent stream* of the two detectors, and

$$\frac{1}{S_{1+2}(f)} = \frac{1}{S_1(f)} + \frac{1}{S_2(f)}. \quad (76)$$

When the (approximately) co-aligned LIGO Hanford and Livingston detectors are operational, the optimal detection statistic is formed by adding, in quadrature, the SNR for the individual detectors and maximising this with respect to  $\tau$ , the difference in the detection time of the signal<sup>5</sup>,

$$\rho_{\text{coherent}}^2(t) = \max_\tau \frac{|z_{L1}(t) + z_{H1}(t + \tau)|^2}{\sigma_{L1}^2 + \sigma_{H1}^2}. \quad (77)$$

The generalisation of this to an arbitrary network of detectors is given in Appendix D.

### 6.3.2 Source Localisation in the Sky

A single interferometer has no directional sensitivity as it is not a pointed device - the wavelength of the GW ground-based interferometers are built to detect is of the order of magnitude of the interferometer or larger (the peak sensitivity at 100 Hz corresponds to a wavelength of 3000 km). It can detect GW from sources in all directions, except those objects whose orbits lie in the plane of the detector, as there is no distortion of space-time along the direction of propagation. Any knowledge about the location of the source can be determined by timing triangulation (TT) using two or more detectors. This is based purely on the difference in the arrival times of the GW.

Consider a GW travelling in direction  $\hat{\mathbf{n}}$ , arriving at detector  $i$  at  $t_i = t_0 + (\hat{\mathbf{n}} \cdot \mathbf{r}_i)/c$ , with  $t_0$  the time of arrival at an arbitrary reference point and  $\mathbf{r}_i$  the position of the interferometer with respect to that reference point such as, for example, the centre of the Earth (modelled as an ellipsoid, Earth Model WGS-84, see <https://www.lsc-group.phys.uwm.edu/daswg/docs/technical/T010110.pdf>). The measured times  $t_i$  will have some measurement error  $\sigma_i$ , giving a residual

$$\chi^2 = \sum_{i=1}^N \frac{(t_0 - t_i + (\hat{\mathbf{n}} \cdot \mathbf{r}_i)/c)^2}{\sigma_i^2}. \quad (78)$$

An estimate for the value of  $t_0$  is given by minimising this residual over  $t_0$ , giving

$$t_0 = \frac{\sum_{i=1}^N (t_i - (\hat{\mathbf{n}} \cdot \mathbf{r}_i)/c)/\sigma_i^2}{\sum_{i=1}^N 1/\sigma_i^2}, \quad (79)$$



which, substituted back into eqn. 78, yields the timing residual minimised over the geocentric arrival time

$$\min_{t_0} \chi^2 = \sum_{i=1}^N \frac{[-(t_i - \bar{t}) + \hat{\mathbf{n}} \cdot (\mathbf{r}_i - \bar{\mathbf{r}})]^2}{\sigma_i^2}, \quad (80)$$

where

$$\bar{t} = \frac{\sum_{i=1}^N t_i / \sigma_i^2}{\sum_{i=1}^N 1 / \sigma_i^2}, \quad (81)$$

and

$$\bar{\mathbf{r}} = \frac{\sum_{i=1}^N \mathbf{r}_i / \sigma_i^2}{\sum_{i=1}^N 1 / \sigma_i^2}. \quad (82)$$

Finally, to obtain an estimate for  $\hat{\mathbf{n}}$ , the residual of eqn. 80 is minimised with respect to  $\hat{\mathbf{n}}$  with the constraint that  $|\hat{\mathbf{n}}| = 1$ . This can be done using the method of Lagrange multipliers. For  $N = 3$  detectors, there is a degeneracy in determining the component of  $\hat{\mathbf{n}}$  normal to the plane spanned by the three detectors. The sign of this component cannot be determined, producing two mirror images of the object in the sky. For  $N > 3$  detectors, an estimate for  $\hat{\mathbf{n}}$  can be found and then used in eqn. 79 to find  $t_0$ . These together give a value of  $\chi^2$ , which, as a consistency test, should not be much larger than  $N$ . If this is the case, then it is likely that either the signal was a random glitch or the errors on the arrival times are too large to determine the position accurately enough.

Timing triangulation alone is not enough for a robust localisation, especially one that could be followed up by EM observations<sup>56</sup>, and a more accurate localisation should also take into account phase and amplitude information of the signals. However, even with the inclusion of phase with TT, a full Bayesian treatment produces a better estimate of the source location.

## 6.4 Other Data Analysis Techniques

For signals of known shape, searches based on matched filtering are in general the most effective. However, it is too computationally expensive to matched filter long stretches of data. Combined searches<sup>28</sup> are necessary to detect the majority of GW events, as was the case with GW150914. These involve an excess power coincidence test followed by a full matched filter search.

**Excess power** this method searches the detector strain data over short periods of  $\simeq 1s$  for power exceeding the expected value due to noise in a given frequency band<sup>16</sup>. This is an optimal statistic when searching for an unmodelled waveform, and when cross-correlated between multiple detectors this will be the first signal of an event that necessitates a follow-up matched filtering analysis. It is shown to be as efficient as matched filtering with a large template bank, though more limited in detectability distance.

**Clustering algorithms** these are a form of an excess power search<sup>93</sup> that looks for features on a spectrogram that stand out from the noise and resemble a signal of astrophysical origin (see Figure 19b for a real example of such a feature). These are shown to be highly effective in unmodelled searches of transients on timescales of milliseconds to seconds in a network of ground-based interferometers. However, they usually rely on locating a “seed” which is a overdense grouping of pixels. In longer-lived transients (on the order of 10 seconds or more), the power will be spread out and there will not be a

clear seed with a high enough SNR. A seedless clustering<sup>91</sup> method can be shown to give access to a significantly greater observational volume than that achieved with seed-based clustering applied to astrophysically-motivated signals. Despite this being a targeted search, this technique was shown to apply equally well<sup>92</sup> to an untargeted, all-sky search for long-lived transients. Although seedless clustering is more computationally expensive, it is also highly parallel, and the authors outline the performance of such techniques on GPU, clearly showing their feasibility.

**Amplitude-based search** a novel alternative to the excess-power searches uses the Hilbert-Huang transform (HHT)<sup>86</sup>. This is referred to as an excess amplitude search (EAM) and is expected to perform well with non-stationary and non-linear data. The authors use realistic rotating core-collapse supernova models (outlined in more detail in §3.5), and find a false alarm rate of  $< 10^{-3}$  for supernovae out to 30kpc. However, their analysis of the method is at a very early stage, as instantaneous frequency information is not used and it is only applied to simulated data buried in “perfect” Gaussian noise. It is therefore yet to be seen how well this method performs on real data when compared to the previously mentioned excess power techniques.

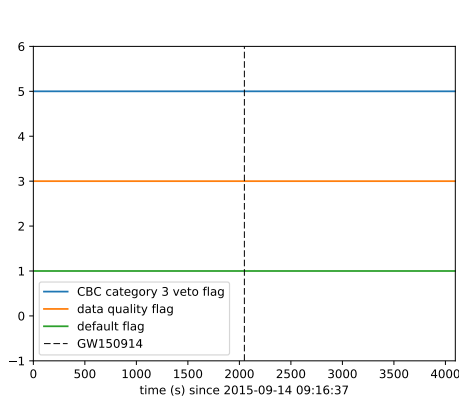
**Machine learning** artificial neural networks (ANN) are usually trained to do a specific task, which they perform with high accuracy. As described in the Gravity Spy<sup>104</sup> project, volunteers can now classify online detector glitches in spectrograms and teach machine learning algorithms to recognize and eliminate them from the search. An average accuracy of 97.1% was achieved in classifying training data, and the project will be an indispensable addition to the other pipelines designed to perform the same task. A neural network search<sup>66</sup> has also been proposed as a complementary detection statistic when searching for GW signals associated with short GRBs. It is found to increase the detectability distance while simultaneously lowering the false alarm probability. However, the analysis is limited in the number of different GRB on which it was tested. Application of a deep neural network (DNN) to detect and eliminate non-stationary, non-Gaussian noise transients<sup>65</sup> in detector data can lead to increased sensitivity. DNNs are expected to be the necessary breakthrough to enable real-time multimessenger astronomy<sup>50</sup>.

## 6.5 GW150914

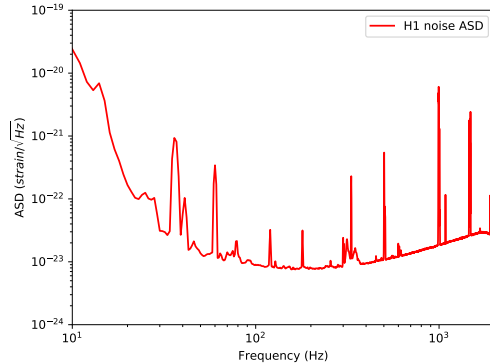
In 2015 LIGO began its first observing run (O1) as Advanced LIGO with a significantly higher strain sensitivity (lower amplitude spectral density of noise), in particular an order of magnitude increase<sup>90</sup> around the most sensitive band of 100 Hz, and greatly improved sensitivity below 40 Hz<sup>70</sup>, extending the sensitivity range in the lower end of the frequency spectrum down to about 10 Hz, where the ASD is now  $\simeq 10^{-22}$ . However, it achieves the greatest sensitivity at frequencies around 100 Hz, where the ASD is  $\simeq 4 \times 10^{-24}$  (see §5.1.1 for the specific improvements carried out).

We now look at the first discovery of GW<sup>7</sup> at an SNR of 23.6 and confidence of  $5.1\sigma$ . The initial detection was made by a coherent two-detector unmodelled transient search<sup>67</sup>.

LIGO has made available all of the data from runs up to and including S6, as well as the data files containing the GW150914 signal (the signal processing is further explained and the file can be downloaded from [https://losc.ligo.org/s/events/GW150914/GW150914\\_tutorial.html](https://losc.ligo.org/s/events/GW150914/GW150914_tutorial.html)). The file of interest starts at GPS time 1126257414 (2015-09-14 09:16:37 UTC). GPS time is the number of seconds since 00 : 00 on January 6, 1980. LIGO provide data files containing 4096 seconds of data sampled at 4096Hz (downsampled from 16384Hz) and 16384Hz in the .hdf5 file format. As the range of interest 10 – 200Hz



(a) The DEFAULT flag offset by 0, the DATA flag offset by 2 and the CBCCAT3 flag offset by 4 for the strain data. The CBCCAT3 flag has a value of 1, meaning that the data passes all tests and can be analysed for CBC events. The DEFAULT flag also has a value of 1, indicating that all of the data quality tests are passed.



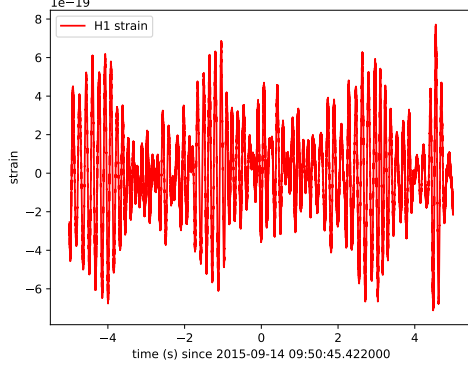
(b) The ASD of noise of the H1 detector measured from 2000 seconds of the strain data. The 500 Hz resonance frequency of the mirror suspensions and its harmonics, as well as the 60 Hz frequency of the power lines and its harmonics, are clearly visible in this plot. Low frequency noise begins to dominate below 20 Hz, and photon shot noise is the dominant source above  $\simeq 150\text{ Hz}$ .

Figure 17: The data quality flags and ASD for H1 strain data starting at GPS time 1126257414.

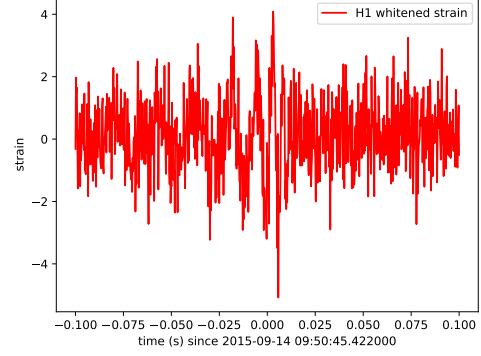
falls well below the Nyquist frequency for both sampling rates, the downsampled data is used here. Each file contains the GPS time, the corresponding strain and the data quality flag (the data quality is stored in 1s subdivisions). We now look at the strain data from the H1 detector.

Any analysis pipeline must first check the data quality flags (the definitions for S6, mostly similar to those of O1, can be found at <https://losc.ligo.org/archive/dataset/S6/>). The DATA flag being 1, for example, is the minimum necessary condition to proceed, as this indicates no NaNs (Not-a-Number) in the data. Unlike with the sample in question, the data will usually have gaps filled with NaNs, when the detector is collecting good quality data, and it would have to be split into smaller segments before being analysed. Figure 17a shows the DATA, CBCCAT3 and DEFAULT data quality channels for the duration of the data sample. The next key step is to obtain an estimate of the ASD of noise, shown in Figure 17b calculated directly from the first 2000s of the data. A more robust estimate of the PSD is obtained from overlapping 256s segments by 128s from 2064s of data, calculating the PSD for each segment and then taking the median in each frequency bin<sup>24</sup>. This latter plot displays the instrumental features described in §4.3.1, including the 500Hz suspension resonance and its harmonics, the 60Hz frequency and harmonics of the power lines, as well as the photon shot noise starting to dominate around  $\simeq 150\text{ Hz}$ .

The event occurs at GPS time 1126259462.422, Figure 18 shows the strain 10 seconds around the event as well as the whitened strain -  $s_w(t) = FT^{-1}[\tilde{s}(f)/\sqrt{S(f)}]$  for 0.2 seconds around the event. The beauty of this plot is that it is possible to see the signal, when the SNR is high enough, "with the naked eye". Figure 19 shows the unwhitened and whitened spectrograms around the event. Both the unwhitened spectrogram and the ASD plot show which frequencies are unwanted and the next step is to apply a bandpass filter which attenuates all of the signal's frequencies in the stopband below a desired level.



(a) The detector strain  $s(t)$  in a 10 second window around GW150914. This is dominated by low frequency noise which creates an envelope, making it impossible to see the GW signal without some processing.

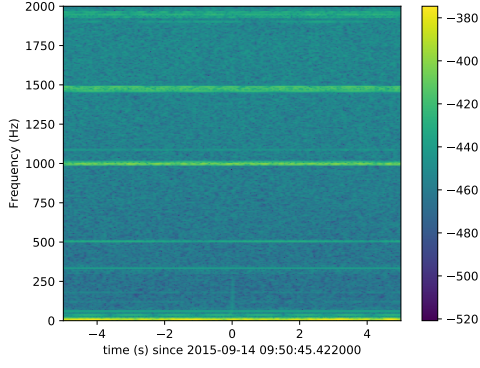


(b) Whitened strain data 0.2s around the event. It is now possible to see the main features of the signal, but further removal of known spectral lines is necessary to clean it up.

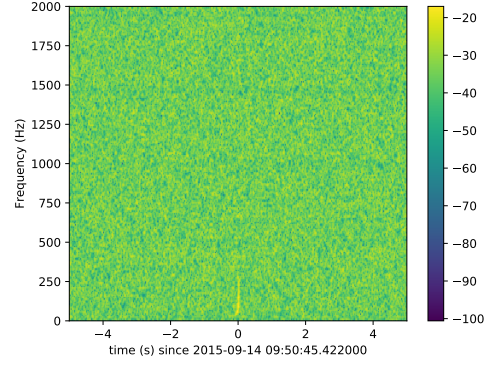
Figure 18: Strain data before and after whitening around GW150914.

Figure 20 shows the application of a 4<sup>th</sup> order bandstop elliptic filter around 510Hz with a passband between 310Hz and 710Hz and a stopband between 490Hz and 530Hz. The power in this frequency band is now clearly below that of the background.

Finally, applying the same 4<sup>th</sup> order filter to the whitened strain to notch (band-pass with a narrow stopband) lines corresponding to the following frequencies (Hz): 14.0, 34.70, 35.30, 35.90, 36.70, 37.30, 40.95, 60.00, 120.00, 179.99, 304.99, 331.49, 510.02, 1009.99 gives the waveform seen in Figure 1. The GW signal is visible, overlaid by the corresponding best-matching NR template. The best match is found to be that of an inspiral of two black holes of masses  $36^{+5}_{-4} M_{\odot}$  and  $29^{+4}_{-4} M_{\odot}$  followed by a merger to a  $62^{+4}_{-4} M_{\odot}$  black hole and its ringdown.



(a) FFTs of size 1024 and overlapping by 15/16 are used to resolve short-time features in the spectrogram. The instrumental lines at 500Hz and multiples thereof are clearly visible, and the signal around  $t = 0$  can just be resolved with the naked eye.



(b) The spectrogram is now plotted for whitened strain, using FFTs of size 512. The GW150914 signal stands out, sweeping in frequency from  $\simeq 30\text{Hz}$  to  $\simeq 250\text{Hz}$ .

Figure 19: Spectrograms in a 10 second window around GW150914.

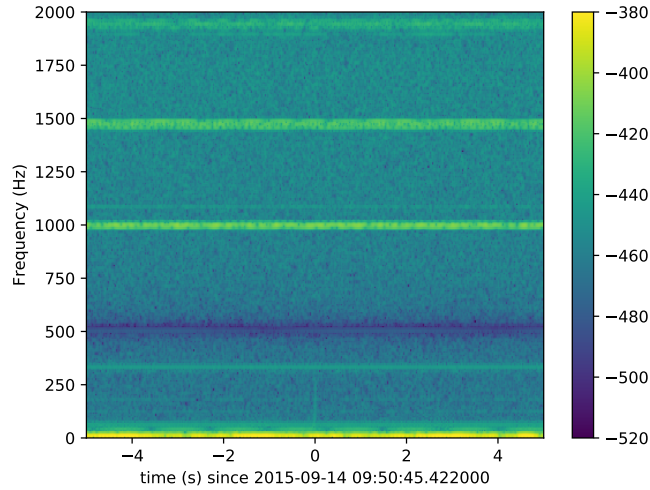


Figure 20: A spectrogram in a 10 second window around GW150914 illustrating the effect of applying a wide stopband filter at 510Hz. The combination of whitening and notching known spectral lines and resonances is what gives the waveform seen in Figure 1.

## 7 Conclusion

### 7.1 Findings

For the past one hundred years, GW have been the cause of controversy, debate and discussion, yet the detection of GW150914 by LIGO factualised GW theory in the scientific community, allowing further confirmation of general relativity and progression in astrophysical, technological and conceptual sectors. The report discusses GW as the direct consequence of analysis under the General Relativity regime. Starting from Newtonian gravity and special relativity, and arriving at the curvature of space-time, it is illustrated how curved spacetime affects Newtonian gravity. By aiming to yield gravitational theory which is invariant under all transformations in any coordinate system, the report then derives the famous Einstein field equations qualitatively, exemplifying the unification of special relativity and Newtonian gravity under General Relativity theory. By considering the simplification of linearised gravity, GW from weak sources are derived, along with their polarisations, and the solution illustrating their luminosity is finally reached. From the first section alone, GW are highlighted as an element of GR, with the section setting the foundation of the astrophysical theory.

With the fundamental mathematical theory of GW, and their detection, it has been made possible to examine and scrutinise sources *directly*, and at the same time verify aspects of general relativity. Such sources are described in section 3, ranging from BNS to BBH and BHNS systems, as well as supernovae and the stochastic GW background. The crucial aspect of GW detection lies in the ability to probe the inner structure of BH and NS, from comparing predicted and detected waveforms, thus modelling tidal interactions of the bodies. An equally significant development is the understanding of the supernovae mechanism - GW provide a test to the hypothesis set out (neutrino, magnetorotational and acoustic mechanisms) concerning core collapse during the supernovae, as each produces a distinct GW waveform. Finally, some other contributions of GW to current knowledge are but are not limited to, the formation of BBH systems, as calculating the precessions provides information on the creation path, the topological structure of BH right before the merger phase, thus providing information on their structure and finally, construction of the GW stochastic background model expected to be produced by inflation, preheating, cosmic strings and first order phase transitions.

Even before their confirmation, GW brought about innovation in the technological field. The instruments required to observe GW needed to be extremely precise, as they were aimed at detecting disturbances of the order of  $10^{-18}$  m. Initially, the detecting method incorporated metal bars which would resonate with the frequency of the GW, known as resonant mass detectors. Such technology was progressively improved from Weber's initial design to modern resonant mass detectors, such as NAUTILUS. The progression was complex and difficult, due to the necessary reduction of noise sources, such as thermal and electronic noise, stemming from the nature of atoms within the metal bar, as well as apparatus of the detector. Regardless, the detectors using metal bars as resonators held little promise as even after all improvements, the detection capabilities were orders of magnitude less than that required to detect GW. The future of resonant mass detectors is in fact still promising, as new designs such as spherical detectors are in development, allowing for detection of GW from all directions and, from the amount of quadrupole modes spherical detectors have, the polarisation of GW as well.

From the limits of resonant mass detectors arose the necessity for a different detection method, namely that of interferometry. Interferometry works on the basic principle of the correlation between the change in the length of arms of the interferometer and that the intensity measured by the detector. Thus came the birth of LIGO. LIGO faces similar challenges as RMD in terms of noise reduction. The three primary sources are thermal, seismic and shot noise types. Thermal noise is dealt with by having a mirror which concentrates thermal motions to a small frequency range, so that they can be differentiated from GW vibrations. Seismic noise is dealt with by construction of a composite suspension system, with active parts using sensors to counter vibrations and passive parts which are comprised of counterweights to prevent horizontal motion of the mirror. Shot noise arises from fluctuations in the mean power of the laser, therefore increasing the laser power reduces the shot noise, before the limit of radiation pressure sets in (see section 4.3.4). With LIGO it was finally possible to detect the first GW, namely GW150914, from a BBH system. Now the scientists in the field have turned their gaze towards refining and expanding the methods of detection.

Development in detection methods is crucial in observing finer sources of GW, such as accurately modelling the stochastic GW signal, and also expanding the range of frequency which can possibly be detected. Thus the plans for several new detectors both on the ground and in space have been unravelled. Advanced LIGO is a new interferometer with superior capabilities to LIGO, being ten times more sensitive, and using a new laser and suspension system to reduce noise even further. Moreover with the signal recycling technique, frequency ranges may be magnified or diminished depending on the desired result, and with the combination of homodyne detection the sensitivity limits of Advanced LIGO are furthered. Even with advancements in technique and technology, ground based detectors lack the capability of measuring low frequency GW due to seismic vibrations, unlike space based detectors. Hence, LISA has been planned. LISA specialises in observing low frequency GW, with its limitations being its sensitivity to gravitational fluctuations and the fact that really low frequency GW overlap and thus become tangled and only possibly discernable during data analysis.

Analysing the signals detected by interferometers is one of the most essential parts of observing GW. The matched filter was shown to be the optimal detection statistic. GW150914 was analysed using this technique - relying first on a coherent excess power search and then by matched filtering. Other search methods need to be applied in the case of unmodelled signals (transients) - these being the excess power methods, including clustering algorithms for short lived transients, and machine learning which can be used as a complementary check for GW produced alongside short GRBs. Currently, the optimal method is the one being employed, of excess power searches followed by matched filtering, yet unmodelled waveform searches need to be refined and explored in the interest of discovering less loud transients buried in the data. Moreover, clustering and seedless clustering methods will need to be implemented to uncover short and long transients respectively. It is quite believable, however, that artificial neural networks (particularly deep learning algorithms) are the key to enabling real-time searches in the future, as they have already shown to be capable of effectively eliminating non-Gaussian noise transients from the data.



## 7.2 Discussion of Findings

From the compilation of all the findings summarised in this review paper, it is evident that GW open up an entirely new era of detector technology, analysis technique and maybe most importantly enable an unprecedented understanding of astrophysical phenomena. As discussed, GW allow for the probing of the inner workings of supernovae mechanisms as well as the coalescing and structure of massive, dense stellar bodies such as BH and NS, something which was previously impossible. The supernova mechanism has been a widely studied yet poorly understood phenomenon in the life evolution of massive stars, and with GW astronomy its mysteries shall be revealed. GW also reveal how event horizons of BH change in nature during the merger phase, thereby providing information on some of the least understood topics in astronomy. Hence astronomy will be enriched and expanded, not only from these understandings, but indirectly as well - for example knowing more concretely the structure and effect of such phenomena may lead to development of dynamical galaxy evolution, particularly when considering supermassive BH. By combining electromagnetic redshift measurements with GW, an even more accurate map of the universe shall be realised. With enough samples of GW from a variety of astrophysical systems and sources, understanding the inner structure of neutron stars will make modelling of the EOS of neutron stars and nuclear matter at extreme densities. Eventually, a model of the stochastic GW background will yield information for the early conditions of the universe. Finally, GW provide another test for the theory of general relativity, in the area of strong gravity, in which it has never been tested before.

Evidently, the discovery of GW has sparked an epoch of new comprehension of astrophysical events, and technological and analytical modernization. From the paper's findings, GW will undoubtedly be an area of research for many years to come and will yield invaluable information in both theoretical and experimental physics.

## References

- [1] GW151226: Observation of Gravitational Waves from a 22-Solar-Mass Binary Black Hole Coalescence. In: *Phys. Rev. Lett.* 116 (2016), Jun, S. 241103. – URL <http://link.aps.org/doi/10.1103/PhysRevLett.116.241103>
- [2] ABADIE, J. u. a.: A Gravitational wave observatory operating beyond the quantum shot-noise limit: Squeezed light in application. In: *Nature Phys.* 7 (2011), S. 962–965
- [3] ABADIE, J. ; ABBOTT, B. P. ; ABBOTT, R. ; ABBOTT, T. D. ; ABERNATHY, M. ; ACCADIA, T. ; ACERNESE, F. ; ADAMS, C. ; ADHIKARI, R. ; AFFELDT, C. ; AL. et: Search for gravitational waves from low mass compact binary coalescence in LIGO’s sixth science run and Virgo’s science runs 2 and 3. In: *Phys. Rev. D* 85 (2012), April, Nr. 8, S. 082002
- [4] ABADIE, J. ; ABBOTT, B. P. ; ABBOTT, R. ; ABERNATHY, M. ; ACCADIA, T. ; ACERNESE, F. ; ADAMS, C. ; ADHIKARI, R. ; AJITH, P. ; ALLEN, B. ; AL. et: TOPICAL REVIEW: Predictions for the rates of compact binary coalescences observable by ground-based gravitational-wave detectors. In: *Classical and Quantum Gravity* 27 (2010), September, Nr. 17, S. 173001
- [5] ABBOTT, B. ; ABBOTT, R. ; ADHIKARI, R. ; AGEEV, A. ; ALLEN, B. ; AMIN, R. ; ANDERSON, S. B. ; ANDERSON, W. G. ; ARAYA, M. ; ARMANDULA, H. ; AL. et: Analysis of LIGO data for gravitational waves from binary neutron stars. In: *Phys. Rev. D* 69 (2004), Juni, Nr. 12, S. 122001
- [6] ABBOTT, B. ; ABBOTT, R. ; ADHIKARI, R. ; AGEEV, A. ; ALLEN, B. ; AMIN, R. ; ANDERSON, S. B. ; ANDERSON, W. G. ; ARAYA, M. ; ARMANDULA, H. ; AL. et: Detector description and performance for the first coincidence observations between LIGO and GEO. In: *Nuclear Instruments and Methods in Physics Research A* 517 (2004), Januar, S. 154–179
- [7] ABBOTT, B. P. ; ABBOTT, R. ; ABBOTT, T. D. ; ABERNATHY, M. R. ; ACERNESE, F. ; ACKLEY, K. ; ADAMS, C. ; ADAMS, T. ; ADDESSO, P. ; ADHIKARI, R. X. ; AL. et: Observation of Gravitational Waves from a Binary Black Hole Merger. In: *Physical Review Letters* 116 (2016), Februar, Nr. 6, S. 061102
- [8] ABBOTT, B. P. ; ABBOTT, R. ; ADHIKARI, R. ; AJITH, P. ; ALLEN, B. ; ALLEN, G. ; AMIN, R. S. ; ANDERSON, S. B. ; ANDERSON, W. G. ; ARAIN, M. A. ; AL. et: LIGO: the Laser Interferometer Gravitational-Wave Observatory. In: *Reports on Progress in Physics* 72 (2009), Juli, Nr. 7, S. 076901
- [9] ABBOTT, BP ; ABBOTT, R ; ABBOTT, TD ; ABERNATHY, MR ; ACERNESE, F ; ACKLEY, K ; ADAMS, C ; ADAMS, T ; ADDESSO, P ; ADHIKARI, RX u. a.: Astrophysical implications of the binary black hole merger GW150914. In: *The Astrophysical Journal Letters* 818 (2016), Feb, Nr. 2, S. L22
- [10] ABBOTT, BP ; ABBOTT, R ; ABBOTT, TD ; ABERNATHY, MR ; ACERNESE, F ; ACKLEY, K ; ADAMS, C ; ADAMS, T ; ADDESSO, P ; ADHIKARI, RX u. a.: GW151226: Observation of gravitational waves from a 22-solar-mass binary black hole coalescence. In: *Physical Review Letters* 116 (2016), Nr. 24, S. 241103

- [11] ABBOTT, BP ; ABBOTT, R ; ABBOTT, TD ; ABERNATHY, MR ; ACERNESE, F ; ACKLEY, K ; ADAMS, C ; ADAMS, T ; ADDESSO, P ; ADHIKARI, RX u. a.: Properties of the binary black hole merger GW150914. In: *Physical review letters* 116 (2016), April, Nr. 24, S. 241102
- [12] ACERNESE, F. ; AGATHOS, M. ; AGATSUMA, K. ; AISA, D. ; ALLEMANDOU, N. ; ALLOCCA, A. ; AMARNI, J. ; ASTONE, P. ; BALESTRI, G. ; BALLARDIN, G. ; AL. et: Advanced Virgo: a second-generation interferometric gravitational wave detector. In: *Classical and Quantum Gravity* 32 (2015), Januar, Nr. 2, S. 024001
- [13] ACERNESE, F ; AMICO, P ; ARNAUD, N ; ARNAULT, C ; BABUSCI, D ; BALLARDIN, G ; BARONE, F ; BARSUGLIA, M ; BELLACHIA, F ; BENEY, J L. ; BILHAUT, R ; BIZOUARD, M A. ; BOCCARA, C ; BOGET, D ; BONDU, F ; BOURGOIN, C ; BOZZI, A ; BRACCI, L ; BRACCINI, S ; BRADASCHIA, C ; BRILLET, A ; BRISSON, V ; BUSKULIC, D ; CACHENAUT, J ; CALAMAI, G ; CALLONI, E ; CANITROT, P ; CARON, B ; CASCIANO, C ; CATTUTO, C ; CAVALIER, F ; CAVALIERE, S ; CAVALIERI, R ; CECCHI, R ; CELLA, G ; CHICHE, R ; CHOLLET, F ; CLEVA, F ; COKELAER, T ; CORTESE, S ; COULON, J P. ; CUOCO, E ; CUZON, S ; DATTILO, V ; DAVID, P Y. ; DAVIER, M ; ROSA, M D. ; ROSA, R D. ; DEHAMME, M ; FIORE, L D. ; VIRGILIO, A D. ; DOMINICI, P ; DUFOURNAUD, D ; EDER, C ; ELEUTERI, A ; ENARD, D ; ERRICO, A ; EVANGELISTA, G ; FABBIONI, L ; FANG, H ; FERRANTE, I ; FIDECARO, F ; FLAMINIO, R ; FOURNIER, J D. ; FOURNIER, L ; FRASCA, S ; FRASCONI, F ; GAMMAITONI, L ; GANAU, P ; GARUFI, F ; GASPARD, M ; GENNARO, G ; GIACOBONE, L ; GIAZOTTO, A ; GIORDANO, G ; GIRARD, C ; GUIDI, G ; HEITMANN, H ; HELLO, P ; HERMEL, R ; HEUSSE, P ; HOLLOWAY, L ; IANNARELLI, M ; INNOCENT, J M. ; JULES, E ; PENNA, P L. ; LACOTTE, J C. ; LAGRANGE, B ; LELIBOUX, M ; LIEUNARD, B ; LODYGENSKI, O ; LOMTADZE, T ; LORIETTE, V ; LOSURDO, G ; LOUPIAS, M ; MACKOWSKI, J M. ; MAJORANA, E ; MAN, C N. ; MANSOUX, B ; MARCHESONI, F ; MARIN, P ; MARION, F ; MARRUCHO, J C. ; MARTELLI, F ; MASSEROT, A ; MASSONNET, L ; MATAGUEZ, S ; MAZZONI, M ; MENCIK, M ; MICHEL, C ; MILANO, L ; MONTORIO, J L. ; MORGADO, N ; MOURS, B ; MUGNIER, P ; NICOLSI, L ; PACHECO, J ; PALOMBA, C ; PAOLETTI, F ; PAOLI, A ; PASQUALETTI, A ; PASSAQUIETI, R ; PASSUELLO, D ; PERCIBALLI, M ; PINARD, L ; POGGIANI, R ; POPOLIZIO, P ; PRADIER, T ; PUNTURO, M ; PUPPO, P ; QIPIANI, K ; RAMONET, J ; RAPAGNANI, P ; REBOUX, A ; REGIMBAU, T ; REITA, V ; REMILLIEUX, A ; RICCI, F ; RICHARD, F ; RIPEPE, M ; RIVOIRARD, P ; ROGER, J P. ; SCHEIDECKER, J P. ; SOLIMENO, S ; SOTTILE, R ; STANGA, R ; TADDEI, R ; TAURIGNA, M ; TEULER, J M. ; TOURRENC, P ; TRINQUET, H ; TURRI, E ; VARVELLA, M ; VERKINDT, D ; VETRANO, F ; VEZIAN, O ; VICERÉ, A ; VINET, J Y. ; VOCCA, H ; YVERT, M ; ZHANG, Z: The present status of the VIRGO Central Interferometer. In: *Classical and Quantum Gravity* 19 (2002), Nr. 7, S. 1421. – URL <http://stacks.iop.org/0264-9381/19/i=7/a=325>
- [14] ALLEN, B.:  $\chi^2$  time-frequency discriminator for gravitational wave detection. In: *Phys. Rev. D* 71 (2005), März, Nr. 6, S. 062001
- [15] ALLEN, B. ; ANDERSON, W. G. ; BRADY, P. R. ; BROWN, D. A. ; CREIGHTON, J. D. E.: FINDCHIRP: An algorithm for detection of gravitational waves from inspiraling compact binaries. In: *Phys. Rev. D* 85 (2012), Juni, Nr. 12, S. 122006
- [16] ANDERSON, W. G. ; BRADY, P. R. ; CREIGHTON, J. D. ; FLANAGAN, É. É.:

- Excess power statistic for detection of burst sources of gravitational radiation. In: *Phys. Rev. D* 63 (2001), Februar, Nr. 4, S. 042003
- [17] ARAIN, M. A. ; MUELLER, G.: Design of the Advanced LIGO recycling cavities. In: *Optics Express* 16 (2008), Juni, S. 10018
- [18] ASTON, S M. ; BARTON, M A. ; BELL, A S. ; BEVERIDGE, N ; BLAND, B ; BRUMMITT, A J. ; CAGNOLI, G ; CANTLEY, C A. ; CARBONE, L ; CUMMING, A V. ; CUNNINGHAM, L ; CUTLER, R M. ; GREENHALGH, R J S. ; HAMMOND, G D. ; HAUGHIAN, K ; HAYLER, T M. ; HEPTONSTALL, A ; HEEFNER, J ; HOYLAND, D ; HOUGH, J ; JONES, R ; KISSEL, J S. ; KUMAR, R ; LOCKERBIE, N A. ; LODHIA, D ; MARTIN, I W. ; MURRAY, P G. ; O'DELL, J ; PLISSI, M V. ; REID, S ; ROMIE, J ; ROBERTSON, N A. ; ROWAN, S ; SHAPIRO, B ; SPEAKE, C C. ; STRAIN, K A. ; TOKMAKOV, K V. ; TORRIE, C ; VEGGEL, A A. van ; VECCHIO, A ; WILMUT, I: Update on quadruple suspension design for Advanced LIGO. In: *Classical and Quantum Gravity* 29 (2012), Nr. 23, S. 235004. – URL <http://stacks.iop.org/0264-9381/29/i=23/a=235004>
- [19] ASTONE, P. u. a.: Search for gravitational radiation with the Allegro and Explorer detectors. In: *Phys. Rev. D* 59 (1999), S. 122001
- [20] ASTONE, P. u. a.: Study of coincidences between resonant gravitational wave detectors. In: *Class. Quant. Grav.* 18 (2001), S. 243–252
- [21] ASTONE, P ; BASSAN, M ; BONIFAZI, P ; CARELLI, P ; COCCIA, E ; COSMELLI, C ; FAFONE, V ; FRASCA, S ; MARINI, A ; MAZZITELLI, G ; MINENKOV, Y ; MODENA, I ; MODESTINO, G ; MOLETI, A ; PALLOTTINO, G.V ; PAPA, M.A ; PIZZELLA, G ; RAPAGNANI, P ; RICCI, F ; RONGA, F ; TERENCEZI, R ; VISCO, M ; VOTANO, L: The gravitational wave detector {NAUTILUS} operating at  $T = 0.1$  K. In: *Astroparticle Physics* 7 (1997), Nr. 3, S. 231 – 243. – URL <http://www.sciencedirect.com/science/article/pii/S0927650597000236>. – ISSN 0927-6505
- [22] ASTONE, P. ; FRASCA, S. ; PIZZELLA, G.: Background Estimation in a Gravitational Wave Experiment. In: *International Journal of Modern Physics D* 9 (2000), S. 341–346
- [23] BABAK, S. ; BISWAS, R. ; BRADY, P. R. ; BROWN, D. A. ; CANNON, K. ; CAPANO, C. D. ; CLAYTON, J. H. ; COKELAER, T. ; CREIGHTON, J. D. E. ; DENT, T. ; DIETZ, A. ; FAIRHURST, S. ; FOTOPOULOS, N. ; GONZÁLEZ, G. ; HANNA, C. ; HARRY, I. W. ; JONES, G. ; KEPPEL, D. ; MCKECHAN, D. J. A. ; PEKOWSKY, L. ; PRIVITERA, S. ; ROBINSON, C. ; RODRIGUEZ, A. C. ; SATHYAPRAKASH, B. S. ; SENGUPTA, A. S. ; VALLISNERI, M. ; VAULIN, R. ; WEINSTEIN, A. J.: Searching for gravitational waves from binary coalescence. In: *Phys. Rev. D* 87 (2013), Januar, Nr. 2, S. 024033
- [24] BABAK, S. ; BISWAS, R. ; BRADY, P. R. ; BROWN, D. A. ; CANNON, K. ; CAPANO, C. D. ; CLAYTON, J. H. ; COKELAER, T. ; CREIGHTON, J. D. E. ; DENT, T. ; DIETZ, A. ; FAIRHURST, S. ; FOTOPOULOS, N. ; GONZÁLEZ, G. ; HANNA, C. ; HARRY, I. W. ; JONES, G. ; KEPPEL, D. ; MCKECHAN, D. J. A. ; PEKOWSKY, L. ; PRIVITERA, S. ; ROBINSON, C. ; RODRIGUEZ, A. C. ; SATHYAPRAKASH, B. S. ; SENGUPTA, A. S. ; VALLISNERI, M. ; VAULIN, R. ; WEINSTEIN, A. J.: Searching for gravitational waves from binary coalescence. In: *Phys. Rev. D* 87 (2013), Januar, Nr. 2, S. 024033

- [25] BARISH, Barry C. ; WEISS, Rainer: LIGO and the Detection of Gravitational Waves. In: *Physics Today* 52 (1999), Nr. 10, S. 44–50. – URL <http://dx.doi.org/10.1063/1.882861>
- [26] BAUSWEIN, H. T.: Measuring neutron-star properties via gravitational waves from binary mergers. In: *Physical review letters*. 108 (2012), Juni, Nr. 1, S. 011101
- [27] BELCZYNSKI, Krzysztof ; BULIK, Tomasz ; FRYER, Chris L. ; RUITER, Ashley ; VALSECCHI, Francesca ; VINK, Jorick S. ; HURLEY, Jarrod R.: On the maximum mass of stellar black holes. In: *The Astrophysical Journal* 714 (2010), April, Nr. 2, S. 1217
- [28] BISWAS, R. ; BRADY, P. R. ; BURGUET-CASTELL, J. ; CANNON, K. ; CLAYTON, J. ; DIETZ, A. ; FOTOPOULOS, N. ; GOGGIN, L. M. ; KEPPEL, D. ; PANKOW, C. ; PRICE, L. R. ; VAULIN, R.: Detecting transient gravitational waves in non-Gaussian noise with partially redundant analysis methods. In: *Phys. Rev. D* 85 (2012), Juni, Nr. 12, S. 122009
- [29] BLAIR, D. G.: *The Detection of Gravitational Waves*. Oktober 2005
- [30] BLANCHET, L. ; DAMOUR, T. ; IYER, B. R. ; WILL, C. M. ; WISEMAN, A. G.: Gravitational-Radiation Damping of Compact Binary Systems to Second Post-Newtonian Order. In: *Physical Review Letters* 74 (1995), Mai, S. 3515–3518
- [31] BUONANNO, A. ; DAMOUR, T.: Effective one-body approach to general relativistic two-body dynamics. In: *Phys. Rev. D* 59 (1999), April, Nr. 8, S. 084006
- [32] BURROWS, Livne E. Dessart L. Ott C. D. Murphy J.: An acoustic mechanism for core-collapse supernova explosions. In: *New Astronomy Reviews*. 50 (2006), November, Nr. 7, S. 487–491
- [33] CAMENZIND, M.: *Compact objects in astrophysics white dwarfs, neutron stars, and black holes*. Springer, 2007
- [34] CAVES, Carlton M.: Quantum-Mechanical Radiation-Pressure Fluctuations in an Interferometer. In: *Phys. Rev. Lett.* 45 (1980), Jul, S. 75–79. – URL <http://link.aps.org/doi/10.1103/PhysRevLett.45.75>
- [35] CENTRELLA, J. ; BAKER, J. G. ; KELLY, B. J. ; VAN METER, J. R.: Black-hole binaries, gravitational waves, and numerical relativity. In: *Reviews of Modern Physics* 82 (2010), Oktober, S. 3069–3119
- [36] CERVANTES-COTA, Jorge L. ; GALINDO-URIBARRI, Salvador ; SMOOT, George F.: A Brief History of Gravitational Waves. In: *Universe* 2 (2016), Nr. 3, S. 22
- [37] COCCIA, E. ; FAFONE, V. ; FROSSATI, G. ; LOBO, J. A. ; ORTEGA, J. A.: Hollow sphere as a detector of gravitational radiation. In: *Phys. Rev. D* 57 (1998), Feb, S. 2051–2060. – URL <http://link.aps.org/doi/10.1103/PhysRevD.57.2051>
- [38] COHEN, Michael I. ; KAPLAN, Jeffrey D. ; SCHEEL, Mark A.: Toroidal horizons in binary black hole inspirals. In: *Physical Review D* 85 (2012), October, Nr. 2, S. 024031
- [39] CORBIN, V. ; CORNISH, N. J.: Detecting the cosmic gravitational wave background with the Big Bang Observer. In: *Classical and Quantum Gravity* 23 (2006), April, S. 2435–2446

- [40] CREIGHTON, J. ; ANDERSON, W.: *Gravitational-Wave Physics and Astronomy: An Introduction to Theory, Experiment and Data Analysis*. November 2011
- [41] CROWDER, J. ; CORNISH, N. J.: Beyond LISA: Exploring future gravitational wave missions. In: *Phys. Rev. D* 72 (2005), Oktober, Nr. 8, S. 083005
- [42] CUTLER, C. ; FLANAGAN, É. E.: Gravitational waves from merging compact binaries: How accurately can one extract the binary's parameters from the inspiral waveform? In: *Phys. Rev. D* 49 (1994), März, S. 2658–2697
- [43] DRAY, Tevian: *The geometry of special relativity*. Taylor & Francis, 2012
- [44] DREVER, R. W. P. ; HALL, J. L. ; KOWALSKI, F. V. ; HOUGH, J. ; FORD, G. M. ; MUNLEY, A. J. ; WARD, H.: Laser phase and frequency stabilization using an optical resonator. In: *Applied Physics B* 31 (1983), Nr. 2, S. 97–105. – URL <http://dx.doi.org/10.1007/BF00702605>. – ISSN 1432-0649
- [45] DROZ, S. ; KNAPP, D. J. ; POISSON, E. ; OWEN, B. J.: Gravitational waves from inspiraling compact binaries: Validity of the stationary-phase approximation to the Fourier transform. In: *Phys. Rev. D* 59 (1999), Juni, Nr. 12, S. 124016
- [46] FABER, J. A. ; RASIO, F. A.: *Hydrodynamics of Neutron Star Mergers*. Januar 2001
- [47] FOFFA, S. ; STURANI, R.: Dynamics of the gravitational two-body problem at fourth post-Newtonian order and at quadratic order in the Newton constant. In: *Phys. Rev. D* 87 (2013), März, Nr. 6, S. 064011
- [48] FROSSATI, G.: Ultralow-temperature resonant gravitational wave detectors, present state and future prospects. In: *Advances in Space Research* 32 (2003), Nr. 7, S. 1227 – 1232. – URL <http://www.sciencedirect.com/science/article/pii/S027311770390322X>. – ISSN 0273-1177
- [49] GAIR, Jonathan R.: The black hole symphony: probing new physics using gravitational waves. In: *Philosophical Transactions of the Royal Society of London A: Mathematical, Physical and Engineering Sciences* 366 (2008), December, Nr. 1884, S. 4365–4379
- [50] GEORGE, D. ; HUERTA, E. A.: Deep Neural Networks to Enable Real-time Multimessenger Astrophysics. In: *ArXiv e-prints* (2017), Dezember
- [51] GEROSA, Davide ; MOORE, Christopher J.: Black hole kicks as new gravitational wave observables. In: *Physical Review Letters* 117 (2016), June, Nr. 1, S. 011101
- [52] GIAIME, J. A. ; DAW, E. J. ; WEITZ, M. ; ADHIKARI, R. ; FRITSCHER, P. ; ABBOTT, R. ; BORK, R. ; HEEFNER, J.: Feedforward reduction of the microseism disturbance in a long-base-line interferometric gravitational-wave detector. In: *Review of Scientific Instruments* 74 (2003), Nr. 1, S. 218–224. – URL <http://dx.doi.org/10.1063/1.1524717>
- [53] GOLDBERGER, W. D. ; ROTHSTEIN, I. Z.: Effective field theory of gravity for extended objects. In: *Phys. Rev. D* 73 (2006), Mai, Nr. 10, S. 104029
- [54] GOLDSTEIN, Herbert: *Classical mechanics*. Pearson, 2014



- [55] GOTTARDI, L. ; DE WAARD, A. ; USENKO, O. ; FROSSATI, G. ; PODT, M. ; FLOKSTRA, J. ; BASSAN, M. ; FAFONE, V. ; MINENKOV, Y. ; ROCCHI, A.: Sensitivity of the spherical gravitational wave detector MiniGRAIL operating at 5K. In: *Phys. Rev. D* 76 (2007), November, Nr. 10, S. 102005
- [56] GROVER, K. ; FAIRHURST, S. ; FARR, B. F. ; MANDEL, I. ; RODRIGUEZ, C. ; SIDERY, T. ; VECCHIO, A.: Comparison of gravitational wave detector network sky localization approximations. In: *Phys. Rev. D* 89 (2014), Februar, Nr. 4, S. 042004
- [57] HARRY, G. M. ; LIGO SCIENTIFIC COLLABORATION: Advanced LIGO: the next generation of gravitational wave detectors. In: *Classical and Quantum Gravity* 27 (2010), April, Nr. 8, S. 084006
- [58] HARTLE, J. B.: *Gravity: an introduction to Einstein's general relativity*. Addison-Wesley, 2003
- [59] HULSE, J. H.: Discovery of a pulsar in a binary system. In: *Neutron stars, black holes, and binary X-ray sources* 48 (1975), Juni, Nr. 1
- [60] IRA THORPE, J.: LISA long-arm interferometry. In: *Classical and Quantum Gravity* 27 (2010), April, Nr. 8, S. 084008
- [61] IWAKAMI, Ohnishi N. Kotake K. Yamada S. Sawada K.: Spiral mode of standing accretion shock instability in core-collapse supernovae. In: *Astrophysics and Space Science*. 322 (2009), Juni, Nr. 1-4, S. 43–47
- [62] IYER, B.: LIGO-India: expanding the international network of gravitational wave detectors. In: *APS Meeting Abstracts*, April 2015
- [63] KAPADIA, S. J. ; JOHNSON-MCDANIEL, N. K. ; AJITH, P.: Estimating effective higher order terms in the post-Newtonian binding energy and gravitational-wave flux: Nonspinning compact binary inspiral. In: *Phys. Rev. D* 93 (2016), Januar, Nr. 2, S. 024006
- [64] KAWAMURA, S. u. a.: The Japanese space gravitational wave antenna: DECIGO. In: *Classical and Quantum Gravity* 28 (2011), Mai, Nr. 9, S. 094011
- [65] KIM, H. ; KIM, Y.-M. ; OH, J. J. ; OH, S. H. ; SON, E. J. ; CHU, H.: Deep Neural Networks for identifying noise transients in Gravitational-Wave Detectors. In: *IAU General Assembly* 22 (2015), August, S. 2257476
- [66] KIM, K. ; HARRY, I. W. ; HODGE, K. A. ; KIM, Y.-M. ; LEE, C.-H. ; LEE, H. K. ; OH, J. J. ; OH, S. H. ; SON, E. J.: Application of artificial neural network to search for gravitational-wave signals associated with short gamma-ray bursts. In: *Classical and Quantum Gravity* 32 (2015), Dezember, Nr. 24, S. 245002
- [67] KLIMENKO, S. ; VEDOVATO, G. ; DRAGO, M. ; SALEMI, F. ; TIWARI, V. ; PRODI, G. A. ; LAZZARO, C. ; ACKLEY, K. ; TIWARI, S. ; DA SILVA, C. F. ; MITSELMAKHER, G.: Method for detection and reconstruction of gravitational wave transients with networks of advanced detectors. In: *Phys. Rev. D* 93 (2016), Februar, Nr. 4, S. 042004
- [68] KLIMENKO, S. ; YAKUSHIN, I. ; MERCER, A. ; MITSELMAKHER, G.: A coherent method for detection of gravitational wave bursts. In: *Classical and Quantum Gravity* 25 (2008), Juni, Nr. 11, S. 114029



- [69] LATTIMER, J. M.: *The nuclear equation of state and neutron star masses*. Mai 2013
- [70] LIGO SCIENTIFIC COLLABORATION ; AASI, J. ; ABBOTT, B. P. ; ABBOTT, R. ; ABBOTT, T. ; ABERNATHY, M. R. ; ACKLEY, K. ; ADAMS, C. ; ADAMS, T. ; ADDESSO, P. ; AL. et: Advanced LIGO. In: *Classical and Quantum Gravity* 32 (2015), April, Nr. 7, S. 074001
- [71] LINTHORNE, N P. ; VEITCH, P J. ; BLAIR, D G.: Interaction of a parametric transducer with a resonant bar gravitational radiation detector. In: *Journal of Physics D: Applied Physics* 23 (1990), Nr. 1, S. 1. – URL <http://stacks.iop.org/0022-3727/23/i=1/a=001>
- [72] LOGUE J., Heng I. S. Kalmus P. Scargill J. H. C.: Inferring Core-Collapse Supernova Physics with Gravitational Waves. In: *Physical Review D* 86 (2012), Februar, S. 044023
- [73] MICHELSON, A. A. ; MORLEY, E. W.: On the relative motion of the Earth and the luminiferous ether. In: *American Journal of Science Series 3* Vol. 34 (1887), Nr. 203, S. 333–345. – URL <http://www.ajsonline.org/content/s3-34/203/333.short>
- [74] MIKAMI, Sato Y. Matsumoto T. Hanawa T.: The Three Dimensional MHD Effects For Core Collapse Supernova Explosion. In: *ASTROPHYSICS OF COMPACT OBJECTS: International Conference on Astrophysics of Compact Objects* Bd. 968 AIP Publishing (Veranst.), 2008, S. 49–52
- [75] MISNER, Charles W. ; THORNE, Kip S. ; WHEELER, John A.: *Gravitation*. W.H. Freeman and Company, 1973
- [76] MOORE, C. J. ; COLE, R. H. ; BERRY, C. P. L.: Gravitational-wave sensitivity curves. In: *Classical and Quantum Gravity* 32 (2015), Januar, Nr. 1, S. 015014
- [77] MÜCK, Michael ; MCDERMOTT, Robert: Radio-frequency amplifiers based on dc SQUIDS. In: *Superconductor Science and Technology* 23 (2010), Nr. 9, S. 093001. – URL <http://stacks.iop.org/0953-2048/23/i=9/a=093001>
- [78] OTT, C. D.: Probing the core-collapse supernova mechanism with gravitational waves. In: *Classical and Quantum Gravity*. 26 (2009), Juni, Nr. 20, S. 204015
- [79] OTT, O'Connor E. P. Gossan S. Abdikamalov E. Gamma U. C. T. Drasco S.: Core-Collapse Supernovae, Neutrinos, and Gravitational Waves. In: *Nuclear Physics B-Proceedings Supplements*. 235 (2013), November, S. 381–387
- [80] OWEN, B. J. ; SATHYAPRAKASH, B. S.: Matched filtering of gravitational waves from inspiraling compact binaries: Computational cost and template placement. In: *Phys. Rev. D* 60 (1999), Juli, Nr. 2, S. 022002
- [81] POINCARÉ, Henri: La Mécanique nouvelle, book containing the text of a lecture presented at the congress of the “Association française pour l’avancement des sciences”(Lille, 1909), the paper dated 23 July 1905 Sur la dynamique de l’électron. In: *Rendiconti del Circolo matematico di Palermo XXI* (1906)
- [82] PRESS, W. H. ; TEUKOLSKY, S. A. ; VETTERLING, W. T. ; FLANNERY, B. P.: *Numerical recipes in C. The art of scientific computing*. 1992

- [83] PUNTURO, M. o.: The Einstein Telescope: a third-generation gravitational wave observatory. In: *Classical and Quantum Gravity* 27 (2010), Oktober, Nr. 19, S. 194002
- [84] RAPAGNANI, P.: Development and test at  $T=4.2\text{K}$  of a capacitive resonant transducer for cryogenic gravitational-wave antennas. In: *Il Nuovo Cimento C* 5 (1982), Nr. 4, S. 385–408. – URL <http://dx.doi.org/10.1007/BF02561646>. – ISSN 0390-5551
- [85] RILES, K.: Gravitational waves: Sources, detectors and searches. In: *Progress in Particle and Nuclear Physics*. (2013), Februar, Nr. 68, S. 1–54
- [86] SAKAI, K. ; OOHARA, K.-i. ; KANEYAMA, M. ; TAKAHASHI, H.: Amplitude-based detection method for gravitational wave bursts with the Hilbert-Huang Transform. In: *ArXiv e-prints* (2016), Juni
- [87] SCHUTZ, Bernard F.: *A first course in general relativity*. Cambridge University Press, 2009
- [88] SHADDOCK, D. A.: Space-based gravitational wave detection with LISA. In: *Classical and Quantum Gravity* 25 (2008), Juni, Nr. 11, S. 114012
- [89] SMITH, J. R. ; LIGO SCIENTIFIC COLLABORATION: The path to the enhanced and advanced LIGO gravitational-wave detectors. In: *Classical and Quantum Gravity* 26 (2009), Juni, Nr. 11, S. 114013
- [90] THE LIGO SCIENTIFIC COLLABORATION ; THE VIRGO COLLABORATION: Sensitivity Achieved by the LIGO and Virgo Gravitational Wave Detectors during LIGO’s Sixth and Virgo’s Second and Third Science Runs. In: *ArXiv e-prints* (2012), März
- [91] THRANE, E. ; COUGHLIN, M.: Searching for gravitational-wave transients with a qualitative signal model: Seedless clustering strategies. In: *Phys. Rev. D* 88 (2013), Oktober, Nr. 8, S. 083010
- [92] THRANE, E. ; COUGHLIN, M.: Seedless clustering in all-sky searches for gravitational-wave transients. In: *Phys. Rev. D* 89 (2014), März, Nr. 6, S. 063012
- [93] THRANE, E. ; KANDHASAMY, S. ; OTT, C. D. ; ANDERSON, W. G. ; CHRISTENSEN, N. L. ; COUGHLIN, M. W. ; DORSHER, S. ; GIAMPANIS, S. ; MANDIC, V. ; MYTIDIS, A. ; PRESTEGARD, T. ; RAFFAI, P. ; WHITING, B.: Long gravitational-wave transients and associated detection strategies for a network of terrestrial interferometers. In: *Phys. Rev. D* 83 (2011), April, Nr. 8, S. 083004
- [94] USMAN, S. A. ; NITZ, A. H. ; HARRY, I. W. ; BIWER, C. M. ; BROWN, D. A. ; CABERO, M. ; CAPANO, C. D. ; DAL CANTON, T. ; DENT, T. ; FAIRHURST, S. ; KEHL, M. S. ; KEPPEL, D. ; KRISHNAN, B. ; LENON, A. ; LUNDGREN, A. ; NIELSEN, A. B. ; PEKOWSKY, L. P. ; PFEIFFER, H. P. ; SAULSON, P. R. ; WEST, M. ; WILLIS, J. L.: The PyCBC search for gravitational waves from compact binary coalescence. In: *Classical and Quantum Gravity* 33 (2016), November, Nr. 21, S. 215004
- [95] WEBER, J.: Detection and Generation of Gravitational Waves. In: *Phys. Rev.* 117 (1960), Jan, S. 306–313. – URL <http://link.aps.org/doi/10.1103/PhysRev.117.306>

- [96] WEBER, J.: Gravitational-Wave-Detector Events. In: *Phys. Rev. Lett.* 20 (1968), Jun, S. 1307–1308. – URL <http://link.aps.org/doi/10.1103/PhysRevLett.20.1307>
- [97] WEBER, J.: Evidence for Discovery of Gravitational Radiation. In: *Phys. Rev. Lett.* 22 (1969), Jun, S. 1320–1324. – URL <http://link.aps.org/doi/10.1103/PhysRevLett.22.1320>
- [98] WEBER, Joseph ; WHEELER, John A.: Reality of the Cylindrical Gravitational Waves of Einstein and Rosen. In: *Rev. Mod. Phys.* 29 (1957), Jul, S. 509–515. – URL <http://link.aps.org/doi/10.1103/RevModPhys.29.509>
- [99] WEINBERG, Steven: *Gravitation and cosmology: principles and applications of the general theory of relativity*. Wiley, 1972
- [100] WEPPNER, McKelvey J. P. Thielen K. D. ; ZIELINSKI, A. K.: A variable polytrope index applied to planet and material models. In: *Monthly Notices of the Royal Astronomical Society*. 452 (2015), September, Nr. 2, S. 1375–1393
- [101] WHITCOMB, S. E.: Ground-based gravitational-wave detection: now and future. In: *Classical and Quantum Gravity* 25 (2008), Juni, Nr. 11, S. 114013
- [102] WILLKE, B. u. a.: The GEO-HF project. In: *Classical and Quantum Gravity* 23 (2006), April, S. S207–S214
- [103] WILLKE, B ; AUFMUTH, P ; AULBERT, C ; BABAK, S ; BALASUBRAMANIAN, R ; BARR, B W. ; BERUKOFF, S ; BOSE, S ; CAGNOLI, G ; CASEY, M M. ; CHURCHES, D ; CLUBLEY, D ; COLACINO, C N. ; CROOKS, D R M. ; CUTLER, C ; DANZMANN, K ; DAVIES, R ; DUPUIS, R ; ELLIFFE, E ; FALLNICH, C ; FREISE, A ; GOSSLER, S ; GRANT, A ; GROTE, H ; HEINZEL, G ; HEPTONSTALL, A ; HEURS, M ; HEWITSON, M ; HOUGH, J ; JENNRICH, O ; KAWABE, K ; KÖTTER, K ; LEONHARDT, V ; LÜCK, H ; MALEC, M ; MCNAMARA, P W. ; MCINTOSH, S A. ; MOSSAVI, K ; MOHANTY, S ; MUKHERJEE, S ; NAGANO, S ; NEWTON, G P. ; OWEN, B J. ; PALMER, D ; PAPA, M A. ; PLISSI, M V. ; QUETSCHKE, V ; ROBERTSON, D I. ; ROBERTSON, N A. ; ROWAN, S ; RÜDIGER, A ; SATHYAPRAKASH, B S. ; SCHILLING, R ; SCHUTZ, B F. ; SENIOR, R ; SINTES, A M. ; SKELDON, K D. ; SNEDDON, P ; STIEF, F ; STRAIN, K A. ; TAYLOR, I ; TORRIE, C I. ; VECCHIO, A ; WARD, H ; WEILAND, U ; WELLING, H ; WILLIAMS, P ; WINKLER, W ; WOAN, G ; ZAWISCHA, I: The GEO 600 gravitational wave detector. In: *Classical and Quantum Gravity* 19 (2002), Nr. 7, S. 1377. – URL <http://stacks.iop.org/0264-9381/19/i=7/a=321>
- [104] ZEVIN, M. ; COUGHLIN, S. ; BAHADINI, S. ; BESLER, E. ; ROHANI, N. ; ALLEN, S. ; CABERO, M. ; CROWSTON, K. ; KATSAGGELOS, A. ; LARSON, S. ; LEE, T. K. ; LINTOTT, C. ; LITTENBERG, T. ; LUNDGREN, A. ; OESTERLUND, C. ; SMITH, J. ; TROUILLE, L. ; KALOGERA, V.: Gravity Spy: Integrating Advanced LIGO Detector Characterization, Machine Learning, and Citizen Science. In: *ArXiv e-prints* (2016), November

## A Action Principles, Lagrangians and Calculus of Variations

In order to define what a Lagrangian and an action is, it is instructive to consider problems akin to ones proposed by the ancient Greeks such as Dido's problem, the brachistochrone and others like these. The problems proposed here all involve maximised a certain function perhaps with some constraints imposed on it as well. The prototypical example is finding the shortest path between two points in Euclidian space. We all know the solution to this is a straight line however to prove that this is the shortest requires what is known as the calculus of variations.

To begin with we define what is called the action ( denoted here by  $I[x]$  )

$$I[x] = \int_a^b L(x(t), \dot{x}(t), t) dt \quad (83)$$

Where the integrand is known as the Lagrangian. To proceed we must examine the problem at hand which involves finding the extremum (maximum or minimum) of the functional ( a functional is analogous to a function as function takes a parameter such as  $x$  as an argument a functional take a function as an argument). To do this we apply what is known as the Euler lagrange equations ( for derivation of these see<sup>54</sup>)

$$\frac{d}{dt} \frac{\partial L}{\partial \dot{x}} - \frac{\partial L}{\partial x} = 0 \quad (84)$$

When the Lagrangian is fed into these equations the resulting differential equations can be solved and the solution to the problem is found. This technique is used widely in physics. General relativity in particular employs this method alot when finding the trajectories of particles in space time. The study of these functionals and their properties is called the calculus of variations.

## B Stationary Gaussian noise

In this appendix, the *probability density function* (PDF) of stationary Gaussian noise is used to motivate the definition of the inner product (a, b).

Given a noise time series  $x(t)$  sampled at regular intervals  $\Delta t$  in  $0 \leq t < T$  which produces a set of  $N = T/\delta t$  samples  $x_j$ , and assuming each of these is an independent Gaussian random variable, the joint PDF for the collection  $\{x_j\}$  is

$$p_x(x_j) = \left( \frac{1}{\sqrt{2\pi}\sigma} \right)^N \exp \left[ -\frac{1}{2\sigma^2} \sum_{j=0}^{N-1} x_j^2 \right]. \quad (85)$$

As the samples are independent, the power spectrum can be shown to be frequency-independent, and taking the Fourier transform of the autocorrelation function  $R_x(\tau) = \langle x(t)x(t+\tau) \rangle$ , applying Parseval's theorem and performing the integral as a discrete sum, one obtains  $S_x = \lim_{\Delta t \rightarrow 0} 2\sigma^2 \Delta t$ , which defines white noise. In the continuum limit, the PDF becomes

$$p_x[x(t)] \propto \lim_{t \rightarrow 0} \exp \left[ -\frac{1}{2\sigma^2} \sum_{j=0}^{N-1} x_j^2 \right] = \exp \left[ -\frac{1}{2} \int_0^\infty \frac{|\tilde{x}(f)|^2}{S_x} df \right]. \quad (86)$$

With the formula also applying to non-white (“coloured”) noise, which can be shown by taking a convolution in the time domain of  $x(t)$  with a kernel  $K(t)$  and then demonstrating that  $S_x \rightarrow S_x(f) = |\tilde{K}(f)|^2 S_x$ . This result gives motivation for defining a noise-weighted inner product  $(a, b)$  of time series  $a(t)$  and  $b(t)$  as

$$(a, b) = 4 \operatorname{Re} \int_0^\infty \frac{\tilde{a}(f)\tilde{b}^*(f)}{S_x(f)} df. \quad (87)$$

With the PDF for a stationary Gaussian noise process now written concisely as  $p_x[x(t)] \propto e^{-(x,x)/2}$ .

## C Derivation of the matched filter

The matched filter is the optimal detection statistic in the Bayesian sense, and one wants to use Bayes’ theorem to distinguish between two hypotheses:

- 1) The null hypothesis  $H_0$  that there is no GW signal in the strain data, so  $s(t) = n(t)$ .
- 2) The alternative hypothesis  $H_1$  that  $s(t) = n(t) + h(t)$ , the strain data contains a GW signal.

Maximizing the odds ratio  $O(H_1|s)$  will favour the presence of a GW signal, where  $O(A|B)$  is defined as  $P(A|B)/P(A'|B)$ , and  $O(A)$  defined as  $P(A)/P(A')$ , the prime denoting the complement of  $A$ . According to Bayes’ theorem, the odds ratio is then  $O(B|A) = O(B)\Lambda(B|A)$  where  $\Lambda(B|A) = P(A|B)/P(A|B')$  is the likelihood ratio. The function to be maximised is therefore

$$O(H_1|s) = O(H_1)\Lambda(H_1|s). \quad (88)$$

Which only depends on the data via the second term on the right-hand side,  $\Lambda(H_1|s) = P(s|H_1)/P(s|H_0) = p(s|H_1)/p(s|H_0)$  where the probabilities are now replaced with probability densities. The two terms are  $p(s|H_0) = p_n[s(t)] \propto e^{-(s,s)/2}$  and  $p(s|H_1) = p_n[s(t) - h(t)] \propto e^{-(s-h, s-h)/2}$ , as in both cases the PDF of the noise is being evaluated. Finally, the likelihood ratio becomes

$$\Lambda(H_1|s) = \frac{e^{-(s-h, s-h)/2}}{e^{-(s,s)/2}} = e^{(s,h)} e^{-(h,h)/2}. \quad (89)$$

Which only depends on the signal through the term  $e^{(s,h)}$  and is a monotonically increasing function of  $(s, h)$ .

The quantity  $(s, h)$  is then the quantity wanted – the matched filter. Any requirement on the odds ratio to accept the hypothesis  $H_1$  can be translated into a required acceptance threshold for the matched filter.

Given the expected signal  $h(t; \boldsymbol{\lambda})$ , to find the optimal detection statistic, one must marginalise over the unknown parameters,

$$\Lambda(H_1|s) = \frac{\int p(s|H_{\boldsymbol{\lambda}})p(H_{\boldsymbol{\lambda}})d\boldsymbol{\lambda}}{p(s|H_0)} = \int \Lambda(H_{\boldsymbol{\lambda}}|s)p(H_{\boldsymbol{\lambda}})d\boldsymbol{\lambda}. \quad (90)$$

Differentiating the natural logarithm of the likelihood ratio with respect to  $\lambda_i$  gives the following system of equations for  $\boldsymbol{\lambda}_{\max}$ :

$$\left( s - h(\boldsymbol{\lambda}), \frac{\partial}{\partial \lambda_i} h(\boldsymbol{\lambda}) \right) = 0. \quad (91)$$

For a signal with an unknown amplitude,  $h(t; A) = Ag(t)$ , the logarithm of the likelihood ratio is

$$\ln \Lambda(H_A|s) = (s|h(A)) - \frac{1}{2}(h(A), h(A)) = A(s, g) - \frac{1}{2}A^2(g, g). \quad (92)$$

Which, according to eqn. 91, is maximised for  $A_{\max} = (s, g)/(g, g)$  thus giving the maximum likelihood statistic,

$$\ln \Lambda(H_{A_{\max}}|s) = \frac{(s, g)^2}{2(g, g)}. \quad (93)$$

Where  $g(t)$  is the known form of the signal – the template.

## D Generalisation to Detector Networks

In a general network of detectors, the interferometers will have different responses to an incoming GW, so when forming the coherent stream, one has to take into account the frequency-dependent beam pattern responses for each detector,  $G_{+,i}(\hat{\mathbf{n}}, \psi, f)$  corresponding to the plus polarised component and similarly  $G_{x,i}(\hat{\mathbf{n}}, \psi, f)$  corresponding to the cross-polarised component. In the long-wavelength limit these become  $F_{+,i}(\hat{\mathbf{n}}, \psi)$  and  $F_{x,i}(\hat{\mathbf{n}}, \psi)$ , with  $\psi$  the polarisation angle and  $\hat{\mathbf{n}}$  the direction of travel of the GW in the co-ordinate frame of the detector. The functions  $G_+$ ,  $G_x$  can be found in §6.1.10 of Creighton & Anderson<sup>40</sup>. In terms of these functions, the coherent stream for the plus polarisation (and equivalently for the cross polarisation) in the Fourier domain becomes

$$\tilde{s}_+(f) = \frac{\sum_{i=1}^N e^{2\pi i f \tau_i(\hat{\mathbf{n}})} G_{+,i}^*(\hat{\mathbf{n}}, \psi, f) \tilde{s}_i(f) / S_i(f)}{\sum_{i=1}^N |G_{+,i}(\hat{\mathbf{n}}, \psi, f) \tilde{s}_i(f)|^2 / S_i(f)}, \quad (94)$$

and the combined noise power spectrum for the plus polarisation (and equivalently for the cross polarisation) becomes

$$\frac{1}{S_+(f)} = \sum_{i=1}^N \frac{|G_{+,i}(\hat{\mathbf{n}}, \psi, f)|^2}{S_i(f)}, \quad (95)$$

with the equivalent of a matched filter for this general network being:

$$\sum_{i=1}^N (s_i, h_i)_i = (s_+, h_+)_+ + (s_x, h_x)_x. \quad (96)$$